UNIVERSITÀ
DEGLI STUDI
DI PADOVA

University of Padova
Department of Information Engineering
Ph.D. Course in Information Engineering: Information and
Communications Technology
Cycle XXXVI

INCREASING THE EFFICIENCY OF SINGLE AND MULTI-CHANNEL CONFIGURATIONS IN DISTRIBUTED FIBER SENSING

Thesis written with the financial contribution of Fondazione
Cariparo

SUPERVISOR: Prof. Andrea Galtarossa
CO-SUPERVISOR: Prof. Luca Palmieri
PH.D. PROGRAM COORDINATOR: Prof. Fabio Vandin

PH.D. STUDENT: Arman Aitkulov

ARMAN AITKULOV

INCREASING THE EFFICIENCY OF SINGLE AND MULTI-CHANNEL CONFIGURATIONS IN DISTRIBUTED FIBER SENSING

Ph.D. Thesis

SUPERVISOR: Prof. Andrea Galtarossa
CO-SUPERVISOR: Prof. Luca Palmieri

Arman Aitkulov: *Increasing the efficiency of single and multi-channel configurations in distributed fiber sensing*, Ph.D. Course in Information Engineering: Information and Communications Technology, © November 2023

Dedicated to the loving memory of my grandmother Raisa.

ABSTRACT

Distributed fiber sensing is a promising and fascinating field of research that can improve many existing detector systems used in oil industry, seismology, minimally invasive surgery, environmental monitoring, and even IoT. While being very compact, optical fibers can be used to implement very accurate measurements with efficient spatial resolution.

This work focuses on distributed sensing applied in acoustic sensing, thermal ablation, and shape sensing. Moreover, the potential for polarization-resolved sensing is explored as well. The implemented sensing configurations are based on the interrogation scheme known as optical frequency domain reflectometry (OFDR), which collects Rayleigh backscattering signals from the fibers exposed to external stimuli. This particular interrogation enables very high resolution. It can be interfaced with optical links that consist either of single or multiple channels. However, each of the arrangements has issues that can be resolved. Single channel sensors are prone to fading, which is proposed to be corrected with the machine learning techniques. In multi-channel schemes, it is challenging to achieve efficient acquisition rates, and this work explores several multiplexing techniques that can lead to improvements. In polarization-resolved sensing, birefringence is difficult to monitor. Unspun multi-core fibers are considered as a way to solve this problem.

PUBLICATIONS

Some of the discussed ideas and figures have appeared previously in the following publications:

[1] Zhannat Ashikbayeva, Arman Aitkulov, Timur Sh. Atabaev, Wilfried Blanc, Vassilis J. Inglezakis, and Daniele Tosi. "Green-Synthesized Silver Nanoparticle-Assisted Radiofrequency Ablation for Improved Thermal Treatment Distribution." In: *Nanomaterials* 12.3 (2022). ISSN: 2079-4991. DOI: 10.3390/nano12030426. URL: https://www.mdpi.com/2079-4991/12/3/426.

[2] Arman Aitkulov, Luca Palmieri, Alessandro Chiuso, and Andrea Galtarossa. "Machine learning method of phase extraction in distributed acoustic sensing scheme based on optical frequency domain reflectometry." In: *27th International Conference on Optical Fiber Sensors*. Optica Publishing Group, 2022, Th4.32. DOI: 10.1364/OFS.2022.Th4.32. URL: https://opg.optica.org/abstract.cfm?URI=OFS-2022-Th4.32.

[3] Arman Aitkulov, Leonardo Marcon, Alessandro Chiuso, Luca Palmieri, and Andrea Galtarossa. "Machine Learning Estimation of the Phase at the Fading Points of an OFDR-Based Distributed Sensor." In: *Sensors* 23.1 (2023). ISSN: 1424-8220. DOI: 10.3390/s23010262. URL: https://www.mdpi.com/1424-8220/23/1/262.

[4] Martina Cappelletti, Arman Aitkulov, Daniele Orsuti, Luca Schenato, Marco Santagiustina, Mirko Magarotto, Cristian Antonelli, Andrea Galtarossa, Antonio Mecozzi, Tetsuya Hayashi, and Luca Palmieri. "Fiber signature-domain multiplexing for high-speed shape sensing." In: *European Workshop on Optical Fibre Sensors (EWOFS 2023)*. Vol. 12643. International Society for Optics and Photonics. SPIE, 2023, 126431W. DOI: 10.1117/12.2678899. URL: https://doi.org/10.1117/12.2678899.

ACKNOWLEDGMENTS

Firstly, I am extremely grateful to my supervisors, professor Andrea Galtarossa and professor Luca Palmieri, for their guidance and patience, as well as for the provided opportunities.

I would like to extend my deepest gratitude to professor Daniele Tosi and Zhannat Ashikbayeva for allowing me to collaborate with them during my period abroad.

I also very much appreciate the help of my fellow research group members Daniele and Martina, as well the council provided by my senior peers Gianluca, Riccardo, and Leonardo.

CONTENTS

LIST OF FIGURES

1 INTRODUCTION

1.1 OVERVIEW OF DISTRIBUTED SENSING

Although the most well-known application of optical fibers is telecommunications, a research interest in using them as sensors has only been increasing ever since the introduction of the concept in the 1960s [1]. The earliest sensors were designed to measure changes occurring outside of the fiber structure. In these extrinsic implementations, fibers were mainly used for transferring data from the sensing entity to the receiver. In a decade, the first intrinsic sensors were developed. They were designed for tracking changes through modulations happening inside the fiber itself.

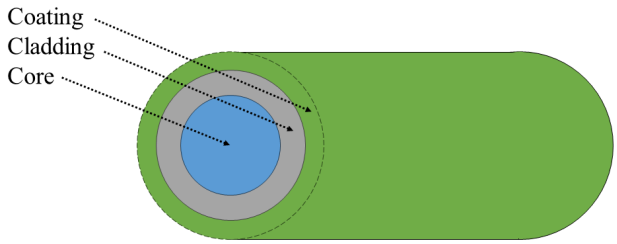

Figure 1.1: Cross-sectional view of a typical optical fiber.

The structural composition of an optical fiber can be seen in Fig. 1.1. The light is transmitted through the fiber core. The cladding layer is often made from the same material as the core, but its refractive index (RI) is slightly lower. As a result, total internal reflection occurs at the boundary between the layers. The coating generally serves for physical protection from environmental effects. Typically, the fiber core is produced using high-silica glasses. Materials such as fluorine are added to the core if lower RI is needed, while the addition of germanium dioxide increases RI. Through the vaporization process, these materials are deposited on the fiber preform. During the drawing process, preforms of the fibers, softened with high temperatures, are pulled and elongated by motor-driven rollers to make them thinner and give them the desired dimensions. Usually, the radius of the single mode fiber (SMF) core is around 4.25 μm, with the overall outer radius including cladding equal to 62.5 μm. In such fibers, there is only one path for the light to propagate through. On the other hand, multi-mode fibers (MMFs), which usually have a core diameter in the range of $50 - 62.5$ μm, allow the light to travel through several propagation paths at the same time. SMFs are considerably less susceptible to the effects of modal dispersion and, consequently, they can provide higher sensitivity and conduct measurements over longer distances, which means that SMF is a more common option in sensing applications.

The reason for the interest in fibers is that they have numerous advantages, including flexibility, compactness, robustness, immunity to electromagnetic interference, and cost effectiveness. The developments done for fibers in telecommunications have also had a positive impact on the sensing area, giving it new sophisticated tools for expanding the capabilities of fiber-based detectors. Today, the sensing category of fiber applications is a vibrant research area with many diverse technologies and directions for future discoveries.

A very popular approach in fiber sensing is fiber Bragg gratings (FBG). FBGs allow to reflect selective wavelengths while transmitting all of the remaining ones. As a result, a spectral peak can be monitored at a certain wavelength. The shifts of the peak allow to infer information about the thermal or strain variations the fiber is subjected to. The advantage of FBGs is high signal-to-noise ratio (SNR) values. However, FBGs need to be inscribed into a fiber, and usually such sensors offer a limited sensing range. Since FBGs are placed on selected points on a fiber, only a quasi-distributed sensing can be implemented with them.

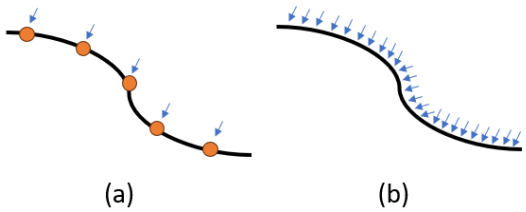

Figure 1.2: Schematic comparison between a) point measurements and b) distributed sensing.

On the other hand, of particular interest are sensing configurations where continuous measurements are conducted along the whole observable length of an optical fiber, allowing to identify the precise location of a perturbation applied to a fiber. It is a concept known as distributed sensing. Fully distributed sensing can be achieved by monitoring the backscattering of optical fibers. Basically, the diffuse back reflections of a light launched into a fiber are measured over time. The time it takes to receive the reflections indicates the length of the light propagation, which means that the intensity of the received signal can be characterized with respect to distance. Of all the backscattering types, Rayleigh backscattering can offer the best spatial resolution and high SNR values.

1.2 APPLICATIONS

The characteristics of optical fibers make them a viable sensing tool for applications in harsh conditions. For example, the measurements of seismic activity were performed with optical fibers in different environments, ranging from urban areas to ocean bottoms [2]. The types of detected seismic activity include earthquakes and smaller scale events, which could be caused by debris flows or industrial processes, such as wastewater treatment or mining. Remarkably, the

sensitivity of fibers allows detecting earthquakes that are hundreds km away. Optical fibers can also be applied as a monitoring tool in pipelines used for oil or gas transportation [3] to define the location of vibrations caused by corrosion or weather impact. In this case, it is more cost efficient to use fiber sensors rather than install cameras along pipelines, which are also less robust against harsh environmental conditions. Similarly, optical fibers can monitor intrusions along railway tracks [4]. In the area of power transmission, fiber sensors were installed on a power transformer to detect vibrations associated with the defects of the mechanical components [5]. Moreover, optical fibers deployed along roads were also shown to be a viable tool in traffic monitoring [6], since they are able to track vehicles by their respective vibrations.

The sensors in the aforementioned applications are based on the detection of acoustic waves. One of the main focuses in this area of fiber sensing, known as distributed acoustic sensing (DAS), is the development of efficient denoising algorithms. Traditionally, the existing commercial sensors, such as geophones, can offer higher sensitivities, but the respective time and cost of the installation procedures, as well as the measurement duration, make DAS a more attractive option.

Another well known set of fiber applications is distributed temperature sensing (DTS), with the first research activities dating back as early as 1982. For instance, optical fibers provide a good alternative to conventional methods of measuring the temperature of insulation oil in a power transformer [7], which is a crucial element in power grids. Another application in the area of power plants involves using optical fibers as a part of the safety system to detect fire [8]. In addition, the maintenance of power cables requires a regular thermal monitoring to locate unwanted hot spots, which can be efficiently conducted with DTS [9]. An important advantage of optical fibers is that they are often already pre-installed in power lines. Optical fibers are also an efficient option for thermal measurements in a lithium-ion battery, since they are easily adaptable to various form factors due to flexibility [10]. Remarkably, Ref. [11] reports the fiber sensor capable of thermally monitoring superconducting power transmission lines at cryogenic temperatures. Optical fibers also offer good sensitivity, which is why they can detect gas leakages in pipelines by monitoring the corresponding temperature drops [12], which are below 1°C. Another application is thermal measurements for the preventive purposes in nuclear reactors [13], which usually are a very difficult environment for the robust placement of sensors.

Naturally, DTS also has high applicability in medicine. Advances of wearable devices have increased the interest in optical fibers due to their portability. One of such implementations is a fiber sensor used in thermotherapies of hand muscles for rehabilitating patients after stroke [14]. However, some applications require to use multiple channels rather than single one, which is what has been considered so far. A configuration consisting of several multiplexed fibers can cover two-dimensional spaces, which is needed when monitoring temperature pattern across tissues subjected to thermal treatment [15]. For

instance, a set of multiplexed fibers containing FBGs was applied as a monitoring tool in cancer treatment tests [16].

Another area that requires to use configurations of multiplexed fibers is shape sensing. In minimally invasive surgery, a fiber placed along a needle can provide accurate information about the insertion procedure [17]. Multi-core fibers assisted by electromagnetic tracking were also explored as an alternative to fluoroscopy in tracking the shape of catheter [18]. It was also demonstrated that optical fibers have applicability in aerospace engineering as tools for monitoring shapes of satellite components [19]. Due to their flexibility, fibers are very suitable for tracking the shape of manipulators in robotics [20, 21]. They can also be used to perform structural monitoring in civil engineering, identifying unwanted shape deformations [22]. However, many of the listed implementations rely on configurations based on the FBG measurements, which means that they can offer limited efficiency in terms of spatial coverage.

Pressure sensors form another subsection of areas where optical fibers can be useful. It is possible to use pressure values recorded by fibers to detect water level elevations during floods [23]. Chemical sensing can also be implemented by tracking RI changes in the medium surrounding the fiber under test [24]. For example, it is possible to measure the level of water salinity [25]. Some implementations, however, require modifications of fiber coating with a layer sensitive to particular substances. Such is the case in Ref. [26], where the fiber was coated with an elastomer sensitive to the presence of hydrocarbons. Coating the fiber with silver allows tracking the presence of hydrogen sulfide gas, as it causes the silver layer to deteriorate, changing the RI along the core [27]. Hydrogen detectors were also implemented by covering fibers with a sensitive film made from tungsten trioxide and palladium [28]. Still, these implementations are categorized as extrinsic sensors.

In addition, many of the described measurements can be done remotely, and in the last decade, it has allowed optical fibers to become a crucial element in various implementations of the Internet of Things (IoT). Hence, there is a powerful incentive to explore fiber sensors, as their applicability in IoT-based areas, such as industrial automation, smart cities, and environmental monitoring, is only going to rise.

To summarize, there is a particular interest towards three categories of distributed fiber sensors, which are acoustic, temperature and shape measurements. What is important is that such sensors can be implemented as intrinsic configurations, emphasizing the uniqueness of fibers in comparison to other techniques. In the context of DAS, configurations are mainly based on single channel. Shape sensing mechanisms require the use of at least three channels to be functional. Moreover, the repetition rates of modern sensing setups also allow to explore real-time monitoring of changing thermal patterns.

1.3 PROBLEM STATEMENT

In the work, all of the sensing is conducted by measuring Rayleigh backscattering with a technique called optical frequency domain reflectometry (OFDR). However, the efficient implementation of the detection requires to address the issues listed in this section.

1.3.1 *Fading in single channel sensor*

Random RI defects along an optical fiber lead to the interference of reflections and the subsequent loss of information at some points of the Rayleigh backscattering. This phenomenon is known as fading. Points of fading occurrence cannot provide meaningful or reliable information. Compared to other distributed sensing methods, OFDR is more robust when encountering fading, but it still has an impact on the measurements.

We propose to approach the problem of fading with machine learning. A neural network can be used to undo the disruptions in backscattering signals. The problem is considered in the context of DAS.

1.3.2 *Acquisition rate in multi-channel sensor*

In a multi-channel optical sensor, which can be built by multiplexing independent fibers or by using multi-core fibers, it is often very challenging to achieve an efficient acquisition rate. Ideally, all channels are interrogated simultaneously. The most straightforward way to implement this is to use separate detectors for each channel, but such setups can be very complex and expensive. Hence, more practical approach is to interrogate channels sequentially using an optical switch. However, the main flaw of this approach is that, compared to the interrogation of a single mode fiber, the acquisition rate is basically reduced by a factor equal to the number of interrogated channels.

In the current work, this issue is addressed for two cases. The first one concerns the applications where a short sensing region needs to be covered and real time monitoring is used. The need for switching can be eliminated by concatenating the multiplexed channels into a single sequential link. In this case, the fibers are used as temperature monitoring tools for thermal therapies.

The second case is for the applications where sensing regions are constrained only by the limits of an interrogation setup. It further improves on the technique in the previous case, because the input light does not need to cycle through the multiplexed links sequentially, but propagates through them simultaneously. In this part, the shape sensing is considered, which is the area where the ability to cover longer distances is more important than in temperature monitoring.

1.3.3 *Rapid variations of polarization state*

An intriguing subset of distributed sensing is polarization-resolved sensing. And yet, it has not managed to integrate into commercial applications of fiber sensors. One of the issues is that conventional SMFs, due to their primary use in communications, are spun to reduce their polarization mode dispersion (PMD). Hence, the state of polarization (SOP) varies too rapidly to be monitored accurately, which makes it difficult to estimate parameters such as the internal twist of the fiber.

In this work, the use of unspun multi-core fibers (MCFs) is proposed to enable the estimation of the twist.

1.4 THESIS STRUCTURE

The main part starts from presenting the state of the art regarding distributed sensing. It includes reviewing the basic interrogation scheme used in the experiments, as well as the relevant background theory about its alternatives and different backscattering types. Existing implementations of high frequency acoustic sensing are considered, followed by the discussion about methods of fading suppression. The machine learning perspective in distributed sensing is also considered. The state of the art chapter is concluded by reviewing the setups for interrogating multi-channel fiber structures.

Chapter 3 explores the development of the single channel acoustic sensor. It starts from the description of the high frequency detection method which is used as a basis in the single channel part. Then, the proposed machine learning method of phase difference estimation is presented. The mathematical model for simulating the training set is described, followed by presenting three neural networks which are considered as possible candidates for the main implementation of phase estimation. The technique of correcting non-linearity introduced by the interferometer is also discussed. The results consist of testing the neural networks on simulated and real perturbations.

From this point, the multi-channel configurations are considered. Chapter 4 details a system of multiplexed fibers in the context of thermal ablation. The methodology part covers the implementation of time division multiplexing by means of fibers with enhanced Rayleigh backscattering. It is followed by presenting the experimental setup for thermal ablation. The chapter is concluded with the results from real-time monitoring of ablating a sample tissue.

Chapter 5 considers shape sensing implemented with a multi-core fiber. Firstly, basic theory is reviewed, including spectral correlation analysis and parallel transport frame method for shape reconstruction. Then, the proposed extension of SCA from single mode fibers onto multi-core fibers is presented. Following this, it is discussed how Cramer-Rao lower bound can be applied in the context of fiber sensing to characterize noise. In the section about experimental setups, a benchmark configuration built with an optical switch and a configuration built for the proposed simultaneous interrogation of multiple

cores are presented. The results consist of the noise characterization and the assessment of shape reconstruction.

Chapter 6 elaborates on the estimation of the internal twist, which becomes feasible due to the interrogation of an unspun MCF. The theoretical framework of this chapter is based on the birefringence analysis.

The report is concluded by providing a commentary on the conducted work, as well as future outlooks on the presented concepts.

2

STATE OF THE ART AND THEORETICAL BACKGROUND

2.1 DIFFERENT SCATTERING PHENOMENA

While most of the light launched into a fiber link travels forward, a portion of it experiences scattering by impurities and inhomogeneities having dimensions much smaller than signal wavelength. In telecommunications, it is one of the major factors that define the loss of power inside the fiber, but in sensing, it is very useful as a measurand. Most of the scattered light escapes the fiber core on the sides, but the monitoring process in distributed sensing is conducted by measuring backscattering, i.e., a portion of the scattering signal that is redirected back to the source of the probing light, as shown in Fig. 2.1.

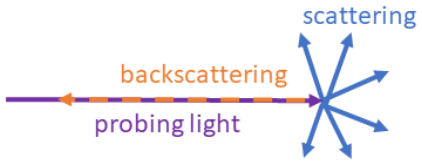

Figure 2.1: Scattering process.

There are different scattering types that can be used to implement sensing, such as Raman, Brillouin and Rayleigh scattering. There is also Mie scattering, but it occurs when the incident photons interract with inhomogeneities of size that is considerably larger than the wavelength of the light. Non-idealities of such sizes are not commonly present in modern fibers. In general, monitored backscattering is comprised of several spectral bands, as shown in Fig. 2.2, which are Stokes, Anti-Stokes, and Rayleigh components. The latter corresponds to the wavelength of the light source, and it is several magnitudes stronger than the former two.

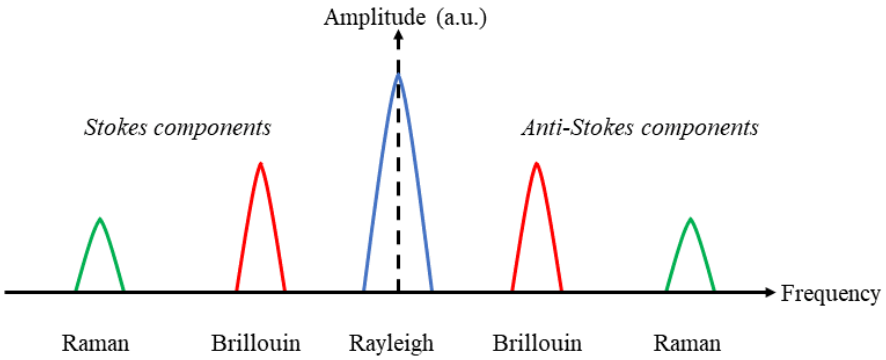

Figure 2.2: Spectral distribution of scattering processes.

Raman scattering, first observed by C. V. Raman in 1928, is an inelastic scattering that occurs when photons interact with matter and undergo changes in their energy and direction of propagation [29]. Scattered particles are shifted to shorter and longer wavelengths that correspond to Anti-Stokes and Stokes lines, respectively. The shifts occur due to the vibration of molecules that interact with the incident photons. The intensity of the Anti-Stokes components responds to thermal variations, but the Stokes line is temperature-insensitive. By considering the ratio of the Anti-Stokes components and the Stokes components, thermal changes with respect to distance can be determined, given the reference conditions. Strain cannot be measured by Raman-based sensors.

Brillouin scattering, initially predicted by Leon Brillouin in 1914, is also an inelastic process that happens when incident photons are scattered by periodic deformation-induced acoustic waves propagating inside an optical channel. The scattered photons experience a Doppler shift [30]. The frequency shifts corresponding to Anti-Stokes and Stokes bands are in the order of GHz, instead of THz as in the case of Raman scattering [31]. Unlike Raman scattering, the frequency shifts in the Brillouin spectra are in response to both temperature and strain changes [32]:

$$\Delta f = K_\epsilon \Delta\epsilon + K_T \Delta T, \tag{2.1}$$

where K_ϵ and K_T are the strain and temperature coefficients, respectively, which are predefined by the properties of the fiber composition. Eq. 2.1 indicates that temperature and strain cannot be measured separately.

Since both Raman scattering and Brillouin scattering are inelastic processes, it is often difficult to achieve high SNR values when monitoring them.

In this work, Rayleigh scattering is considered. Described in 1871 by Lord Rayleigh, this phenomenon is the oldest research concept among the considered processes. In addition to being easier to observe, it also allows to conduct more accurate measurements due to higher spatial resolution. Typically, the SNR of Rayleigh-based configurations is higher than that of sensors based on the other two processes, which allows them to conduct the scans of fiber links at a faster rate. Compared to Brillouin scattering, Rayleigh scattering is also more suitable for measuring dynamically changing strain. Still, OFDR experiences problems associated with phase noise of the laser source [33], which can be managed by applying proper compensation techniques. Still, the significant phase noise issues arise in configurations that cover long distances, which is not the case in the current work, where the distances under 100m are considered for all sensing configurations.

Rayleigh scattering is observed when light is scattered by particles whose wavelengths are at least 10 times smaller than the wavelength of light. It is an elastic scattering, as the energies of the scattered photons do not change. The scattered particles continue to vibrate at the frequency of the originating light. The intensity of the scattered

light is inversely proportional to the 4th power of the wavelength. An example of this phenomenon is the blue sky. Sunlight is scattered by air particles in atmosphere, and since the blue light has shorter wavelengths in the visible range, its scattering intensity is the highest.

Inside an optical fiber, photons are scattered by very small inhomogeneities in the fiber structure. Typically, these non-idealities are formed at the fabrication stage during fiber drawing. High temperatures around 2000°C are applied to soften the fiber material. The resulting random molecular motions lead to miniscule density variations in the fiber structure. Then, it is subjected to a very rapid cooling. As the viscosity of the material increases, the previously formed impurities become the fixed characteristics of the fiber, since there is not enough time for density to be readjusted within the duration of the cooling process.

Unlike other discussed processes, Rayleigh scattering is, in general, independent of external physical fields. While Raman and Brillouin scatterings measure temperature or strain directly, Rayleigh-based sensors utilize the scattering itself to track changes associated with these stimuli. A scatterer by itself is not necessarily sensitive to temperature and strain. Instead, temperature and strain alter the spatial distribution of scatterers along a fiber, thereby changing the properties of the light propagation. By tracking these changes in the scattering, we can indirectly detect the applied stress. Initial Rayleigh-based detectors conducted sensing by measuring changes in the intensity of backscattering. Over time, the sensing techniques became more sophisticated due to development of tracking methods based on cross-correlation and phase difference.

Similarly to Brillouin scattering, Rayleigh scattering also cannot discriminate whether the changes are induced by temperature or strain. Hence, when considering one of these stimuli, we have to minimize the impact of the other one by carefully managing the environmental conditions.

While Rayleigh scattering is somewhat limited in terms of the observable length due the phase noise, in the considered applications and conditions, a Rayleigh-based sensor is clearly the most practical choice due to significant improvements in spatial resolution.

2.2 INTERROGATION TECHNIQUES IN DISTRIBUTED SENSING

2.2.1 *Fiber signature*

In distributed sensing, the changes in the state of the optical channel are monitored with respect to a previously obtained reference, which usually corresponds to the backscattering of the unperturbed straight fiber. As long as an outside impact is not present, this measurement can be considered as the constant signature of the fiber, since the arrangement of the scattering centers is expected to remain fixed even over long times. The fiber signature is a key concept in distributed

sensing; it does not need to be collected at the start of each sensing session since it can be reused.

2.2.2 *Optical time domain reflectometry*

There are several ways to implement distributed sensing with optical fibers. It is possible to use optical time reflectometry (OTDR), which was developed in 1970s. The original intention was for it to be a testing tool for identifying faults within optical transmission lines, as well as attenuation along each fiber section. In OTDR, a pulse sequence is sent into the fiber. Rayleigh scattering is collected with a photodetector at the same end of the fiber that is used to launch the probe, as indicated in Fig. 2.3. Temporal evolution of the received backscattering indicates the time it takes for the light to travel through the fiber, which means that is equivalent to the spatial distribution.

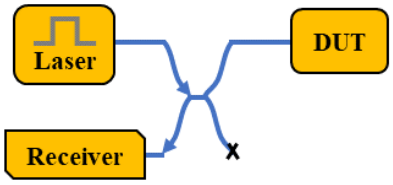

Figure 2.3: Schematic of the OTDR setup.

An example of the trace usually observed in OTDR is shown in Fig. 2.4.

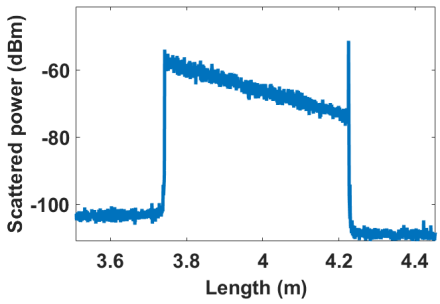

Figure 2.4: Example of backscattering obtained in OTDR.

The attenuation of backscattering exponentially increases with the propagated distance. The received signal is equivalent to the spatial representation of the backscattering, because time relates to distance as

$$t = \frac{2z}{v_g}, \tag{2.2}$$

where v_g is the group velocity of the probing signal, and the multiplication by 2 is due to the round-trip propagation. The spatial resolution is dependent on the pulse duration τ_p:

$$\delta z = \frac{v_g \tau_p}{2}. \tag{2.3}$$

Longer pulse duration leads to higher pulse energy and, consequently, to higher signal-to-noise ratio (SNR) at the expense of spatial resolution. Moreover, OTDR offers limited performance when it comes to measuring areas close to the launching end of the fiber, so-called "dead zones" of the interrogation created because of photodiode saturation.

2.2.3 *Optical frequency domain reflectometry*

In OTDR, the compromise between SNR and spatial resolution has to be achieved, which is not the case for optical frequency domain reflectometry (OFDR). OFDR was first introduced in 1981, with an initial purpose of measuring optical losses in a fiber. Eventually, it evolved into a sensing technique with high commercial applicability.

In OFDR, a tunable laser source is used to interrogate a fiber link with a signal whose frequency is linearly increased in time within the duration of a single scan:

$$E_{in}(t) = E_0(t)e^{-j2\pi\nu(t)t}, \tag{2.4}$$

where $\nu(t)$ is the instantaneous frequency value during the frequency sweep, and $E_0(t) = c(t)e^{j2\nu_0 t}$, with ν_0 as the reference carrier frequency and with $c(t)$ as the baseband component. The amplitude of the sweep is mostly kept constant. Typically, the light source with central wavelength 1550 nm is used, and the sweep range can cover up to 80 nm. The instantaneous frequency is defined as

$$\nu(t) = \sigma t, \tag{2.5}$$

where σ is the rate of the frequency sweep. The operational principle of OFDR is based on the Mach-Zehnder interferometer, as shown in Fig. 2.5. It is a case of heterodyne detection. One arm of the interferometer serves as a reference, and the second one is connected to a fiber under test (FUT). It is assumed that the light propagates through the reference arm without changing. However, the light in the measuring arm is delayed, as it passes through a different optical path due to the FUT. These two arms are recombined, bringing them into interference with each other, and the resulting output detected by a photodiode is

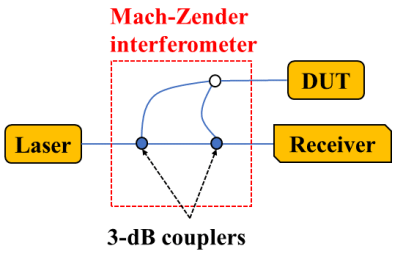

Figure 2.5: Schematic of the OFDR setup.

$$E_{out}(t) = E_0(t)e^{-j2\pi\nu(t)\,t} + r(\tau)\,E_0(t-\tau)e^{-j2\pi\nu(t-\tau)\,t}, \tag{2.6}$$

where τ is a delay in the input signal due to propagating through the measuring arm of the interferometer, and $r(\tau)$ is the reflectivity attenuation corresponding to this delay.

Then, the photodetector registers the following intensity signal, which is proportional to the power of a signal in Eq. 2.6:

$$I(t) = |E_0(t)|^2 + r^2(\tau)\,|E_0(t-\tau)|^2 + I_b(t). \tag{2.7}$$

with

$$I_b(t) = 2r(\tau)\,E_0(t)\,E_0(t-\tau)\cos[2\pi\,\nu(t)\,\tau)]. \tag{2.8}$$

$I_b(t)$ is a beat signal which contains information about the interference of the arms. More specifically, the beat signal is dependent on τ or, equivalently, on the difference between the paths of the arms.

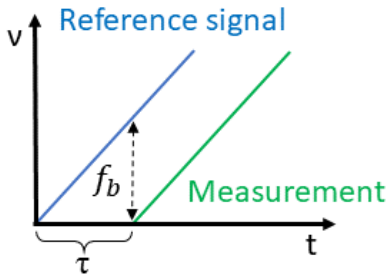

Figure 2.6: Beat signal of the interference between the arms.

The schematic representation of the beat signal in Fig. 2.6 shows that the interference of two swept signals introduces a beat frequency $f_b = \sigma\tau$. Combining Eq. 2.5 and Eq. 2.8, we can express the beat signal as a function of this frequency:

$$\begin{aligned} I_b(t) &= 2r(\tau)\,E_0(t)\,E_0(t-\tau)\cos(2\pi\,\sigma\,t\,\tau) \\ &= 2r(\tau)\,E_0(t)\,E_0(t-\tau)\cos(2\pi f_b t). \end{aligned} \tag{2.9}$$

Beat frequency f_b is linearly dependent on the delay τ. Thus, the Fourier transform, $i(f_b)$, of the detected intensity signal in Eq. 2.7 basically maps beat frequencies to particular locations along the interfering distance, providing the equivalent of the spatially distributed trace that is observed in OTDR; the first two terms in Eq. 2.7 correspond to very low frequencies, so their transforms are located close to zero or at zero point of time axis. More specifically, distance can be expressed in terms of beat frequency as

$$z = \frac{v_g}{2\sigma} f_b, \tag{2.10}$$

and if the backscattering signal, $i(f_b) = i(z)$, needs to be characterized in terms of propagation time, the same relationship as in Eq. 2.2 from the OTDR case can be used.

By definition, σ is the range of frequencies, Δf, swept within the probe time, T, so Eq. 2.10 becomes

$$z = \frac{v_g T}{2\sigma\Delta f} f_b. \tag{2.11}$$

Then, the spatial resolution is

$$\delta z = \frac{v_g}{2\Delta f}. \tag{2.12}$$

The resolution of the resulting signal is defined by the frequency sweep at the input. By increasing the range of the sweep, finer measurements are achieved. Compared to Eq. 2.3 from the case of OTDR, this is considerably more efficient method to improve spatial resolution, because SNR is not compromised. Moreover, compared to OTDR, the continuous nature of the OFDR probe makes it more suitable to conduct dynamic measurements.

The length beyond which the arms can no longer interfere is called the coherence length of the source. It depends on the properties of the source, and can be increased by narrowing the bandwidth of the laser. Since the measured distances in the work are within the coherence length of the utilized OFDR probe, the laser phase noise term in Eq. 2.4 is neglected.

As stated before, the primary outputs of OFDR and OTDR have the same meaning, as they provide the intensity as a function of propagation distance, which is a time domain information. In the analysis, the signal is segmented. Then, inverse Fourier transform is applied to each of the segments. By comparing each segment in the collected backscattering with its counterpart in the signature backscattering, the external stimuli is quantified and localized. There are two main comparison methods: phase-based and correlation-based detections. They are going to be discussed in detail in the parts dedicated to single and multi-channel configurations, respectively.

A more detailed implementation of OFDR is shown in Fig. 2.7. An additional interferometer is used to trigger the acquisition of the backscattering signals. In the main interferometer, a delay line is introduced to balance the signals from the arms. Moreover, this OFDR scheme enables polarization-resolved sensing. Polarization provides orientational information about the oscillations of the electrical field generated by the light as it propagates. The direction of an oscillation in a plane orthogonal to the propagation path is described by the state of polarization (SOP). At the output of the schematic in Fig. 2.7, there is a polarization beam splitter which separates the backscattering into orthogonal polarization traces, referred to as S and P components. The components describe the oscillation of the received light wave projected onto horizontal and vertical planes which are parallel and orthogonal, respectively, to the probe signal [34]. As exemplified in Fig. 2.8, the components oscillate in a complementary manner; their sum results in the overall unsplit backscattering.

It should be commented that the oscillations in Fig. 2.8 are caused by the linear birefringence. The analysis of birefringence can further extend the distributed sensing capabilities of fibers, making it possible to measure magnetic fields [35] and electric currents [36], as well as fiber twist [37]. Since the SOP of the input light is mostly preserved in the backscattering, the birefringence can be measured by combining the information obtained from launching different SOPs into the

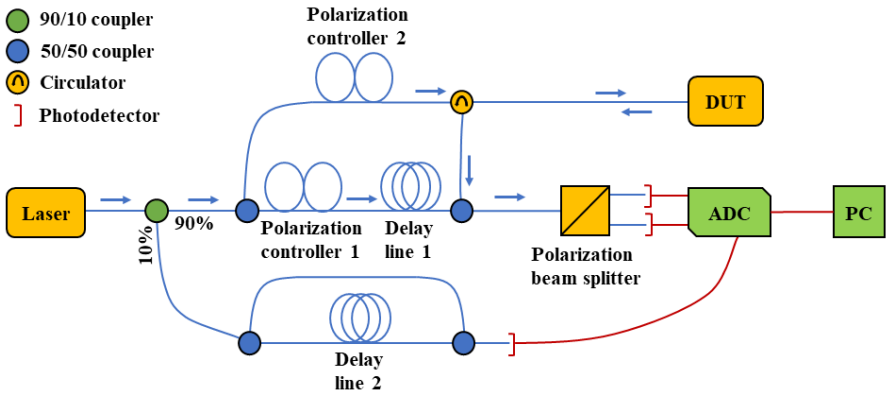

Figure 2.7: Practical OFDR implementation.

fiber. The SOPs of the input can be varied using phase modulators, but these modifications are not included in the default OFDR scheme.

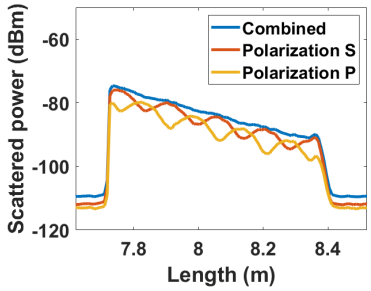

Figure 2.8: Example of polarization components.

So far, coherent OFDR has been considered. In incoherent OFDR, the amplitude of the sweep signal varies as a sinusodial function instead of being constant. The received backscattering is modulated by the same function as the input signal. Thus, at the receiver, there is a delay between the same frequencies in the source modulation and in the output modulation, which means that in the Fourier transform of the received signal, the frequencies are linked to their respective propagation distance. Hence, similarly to OTDR (Eq. 2.3), the spatial resolution is inversely proportional to the bandwidth of the source. Compared to its coherent counterpart, incoherent OFDR is inherently more suitable for detection over longer distance.

Still, coherent OFDR is a considerably more prevalent technique in contemporary works due to advances in techniques of controlling the frequencies of the input signal. Incoherent OFDR is considered more frequently in the context of Raman and Brillouin scatterings.

2.3 ELASTO-OPTIC EFFECT

Due to the impact of an external medium, the distribution of the scattering centers inside the FUT can be altered, consequently affecting refractive index (RI) along its surface. Thus, the outside stimulus and its respective place of application can be quantified by tracking the evolution of the backscattering along the fiber link, with respect to

the previously collected signature. In general, the overall backscattering of a light wave $a(t)$ can be modelled as the superposition of the backscattering signals due to the scatterers in the probed link L:

$$B_L[a(t)] = \sum_k c_k e^{-j2\beta_0 z_k} a(t - 2\beta_1 z_k), \tag{2.13}$$

where c_k is the Rayleigh backscattering coefficient, z_k is the location of a scatterer, and β_0 and β_1 are the propagation constant and the inverse group velocity, respectively. The RI changes can be tracked by evaluating the spectral shifts in the signal from Eq. 2.13:

$$\frac{\Delta n}{n} \approx \frac{\Delta f}{f}. \tag{2.14}$$

The phenomenon of mechanical stress, ε, causing the RI changes is known as elasto-optic effect. Acoustic waves also result in elasto-optic effect, as they change the electrical permittivity of the fiber when interacting with it. Temperature, T, also causes variations in RI along the fiber. It follows that elasto-optic and thermo-optic effects are linked by the following relationship:

$$\Delta f = K_\varepsilon \Delta\varepsilon + K_T \Delta T. \tag{2.15}$$

K_ε and K_T are typically equal to $0.15\text{GHz}/\mu\epsilon$ and $1.5\text{GHz}/^\circ\text{C}$, respectively [38]. From Eq. 2.15, there is an issue of cross-sensitivity. Only Raman-based configurations are not affected by it, since they detect only thermal variations.

2.4 MULTI-CORE FIBERS

So far, we have been considering sensing in the context of conventional SMFs, whose fiber structure contains only one core. On the other hand, a multi-core fiber (MCF) contains multiple cores within its fiber structures, as demonstrated in Fig. 2.9.

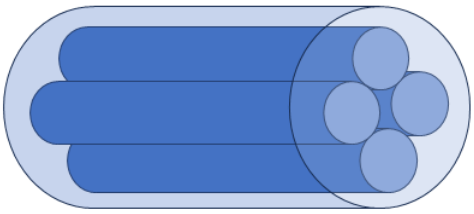

Figure 2.9: Multi-core fiber structure.

Each of the cores is an independent channel, separated from the rest of the cores within the constrains of the same cladding. Since the light propagates along parallel channels, the multiplexing capacity of the fiber increases with the number of cores.

While the manufacturing process of MCFs is more complex than that of SMFs, the accessibility of such fibers keeps increasing due

to the continued research interest. Compared to SMFs, it is not as straightforward to interface MFCs with the interrogation devices, but there are many commercially available components that allow to integrate MCFs into the sensing configurations.

Since OFDR operates with a coherent light source, the issue of cross-talk between the cores in an MCF may be exacerbated. The reason is that incident photons preserve their phase relationship, and the spatial overlapping between the photons from the neighbouring cores results in a destructive or constructive interfrence. However, the use of an uncoupled MCF resolves this issue.

2.5 HIGH FREQUENCY ACOUSTIC SENSING

In conventional OFDR-based DAS techniques, the limits of the detectable frequency are determined by the repetition rate of the scan. For each scan, the cross-correlation method, which is discussed in Chapter 5 in detail, is used to obtain the spectral shifts with respect to distance. Since the time step between the consecutive scans is known, it can be seen which shifts occur in a periodical manner. Hence, the works on the correlation-based DAS are directed towards maximizing the repetition rate. By driving an I/Q modulator with an arbitrary waveform generator, the repetition rate of 10 kHz was achieved [39]. Another method replaces the conventional linear sweep of OFDR with frequencies varying in a sinusoidal manner, which allows increasing the repetition rate of scans [40]. However, the method is computationally more involved that the traditional OFDR.

A technique called time-resolved OFDR leverages the fact that the distance dependence of the backscattering trace is related to the time dependence. Different parts of the backscattering spectrum relate to different time instants. Hence, at each time instant, or, equivalently, spatial position, the backscattering trace can be analyzed to obtain specific, local information [41]. The detection limit depends on the parameters of the laser source.

Initially, the idea to use the phase of backscattering trace to measure the vibrations was broached in 1990. Unlike the amplitude variations, the backscattering phase is linearly dependent on the acoustic or mechanical perturbation applied to the fiber, making it possible to accurately capture dynamic variations.

It should also be noted that there are novel DAS techniques that achieve sensing regions over 100 km, but in the currently considered applications, it is sufficient to consider the length provided by OFDR.

2.6 FADING SUPPRESSION METHODS

A popular method to mitigate the impact of fading is to launch different frequencies into the probing light [42–44], obtaining several spatial signatures for each of them. Thus, fading points in one signature can be compensated by the remaining ones. However, in addition to increasing the acquisition time by the number of probing frequencies,

this is the method applied in OTDR, and it is incompatible with the OFDR paradigm. Another technique utilizes two independent laser sources to interrogate the FUT [45] and combine the resulting pair of the backscattering traces. It is used in OTDR, but, in principle, the technique could also be used in OFDR. However, such configuration would be expensive and complex in terms of hardware. In another OTDR method, fading points can also eliminated by identifying them through comparison with the phase peaks caused by the known induced perturbation [46]. The use of acousto-optic modulator to code the intensity of OTDR pulses in a specific ways also allows to suppress fading [47]. Moreover, a successful mitigation of fading has recently been achieved by using nonlinear amplification in phase-OTDR [48]; the input traces of lower intensities pass through higher gains, and vice versa, which allows to decrease the signal deterioration induced by fading.

Still, in literature, the majority of fading suppression methods consider OTDR rather than OFDR, even if there are approaches that are suitable for both interrogation schemes. For instance, it is possible to remove fading through computations involving sorting and averaging [49].

Regarding the OFDR methods, the implementations that utilize cross-correlation techniques can mitigate the fading effects; however, in this case, the scan rate of the tunable laser puts a limit on the range of detectable frequencies, which is why it is still more preferable to work with schemes based on phase difference calculation. One way to lower the fading effects is to average the backscatterings of the channels of a multi-core fiber [50]. However, this method is intrinsically incompatible with DAS, which needs to be implemented with a single channel. In this case, the averaging across multiple channels could distort and invalidate the information about dynamic changes of the acoustic vibrations. In another approach [51], the measured backscattering and the respective reference are segmented. The segments are converted into frequency domain, and then the phase signals can be obtained. For each segment, the difference between the phases of the measurement and the reference is obtained. The resulting phase signals are compared using a sliding window. In the windowed regions, the most similar phase signals are identified and averaged, mitigating possible fading impact. The corrected phases are combined to provide the overall phase evolution along the fiber. However, the detectable frequency of the method is defined by the scan rate of the setup.

2.7 MACHINE LEARNING IN DISTRIBUTED SENSING

Optical fiber sensors are utilizing the techniques of machine learning at a rapidly increasing rate. For example, convolutional neural network (CNN) was applied to measure pipeline corrosion [3]. There have been reports of vibration event recognition implemented with support vector machine (SVM) [52], relevance vector machine [53], and a configuration combining SVM and CNN [54]. Three models

built with multilayer perceptron, CNN, and CNN combined with long short-term memory (LSTM) network were used to perform classification of earthquake signals [55]. Linear regression was applied to decouple thermal measurements from humidity in the distributed humidity sensor based on monitoring Brillouin backscattering [56].

However, in the context of optical fiber sensing, the majority of machine learning implementations are classification problems. In the considered application, the processing of temporal data at the input and the output is required. In terms of computational resources, it is too demanding to train a neural network based on LSTM [57], especially if small kernel sizes are used to work with temporal sequences. Some implementations of machine learning in optics utilize CNN to process images that represent spatial phase information [58, 59]. However, in areas apart from optics, it has been recently shown that the U-Net architecture can achieve an efficient performance in both image [60] and temporal data [57, 61].

2.7.1 *Artificial datasets*

It should be noted that the use of simulated data for the training is a popular technique. The models based on generative adversarial network (GAN) can generate training data themselves [62, 63], but it is also possible to create artificial samples with theoretical models. For example, the CNN for denoising seismic images was trained with signals simulated with the Ricker wavelet [64]. Artificial image data was used to train the CNN model for denoising measurements in electron microscopy [65]. Another CNN also utilized synthetic data during training for correcting phase and frequency in magnetic resonance spectra [66].

2.8 DOPED FIBERS

The intensity of the optical signal decreases in an exponential manner along the fiber. Hence, at some point the backscattering becomes too noisy to provide reliable information. However, the default backscattering strength can be improved. For instance, the intensity of the scattering signal can be increased by treating the fiber with UV radiation; this technique was shown to achieve an increase in backscattering by a factor of 10 [67]. By subjecting a region of the fiber core to the irradiation by femtosecond laser, a 40 dB enhancement in the backscattering was achieved [68]. A similar gain has been achieved by using femtosecond laser to inscribe a nanograting into the fiber structure [69]. Another convenient way to modify the propagating properties of optical fibers is to merge the fiber structure with rare-earth dopants. It becomes possible to increase the gain of backscattering, achieving higher SNR values in the distributed sensing measurements. For example, fiber materials with high concentrations of germanium allow to increase the backscattering signal by 6 dB [70]. The addition of gold nanoparticles coated with zirconia into the fiber core not only

increased the Rayleigh backscattering, but also allowed it to detect temperatures up to 800°C. It should be noted that dopants can be introduced into the fiber structure even after the fiber had been manufactured.

As said before, scattering events occur when light encounters defects and inhomogeneities inside the fiber link. Enhancing the backscattering increases the probability of these scattering events, which leads to more energy losses. Hence, enhanced backscattering also has a faster attenuation rate. However, if the sensing needs to be done over a short distance, it is not a significant issue. Potentially, it means that fibers with the enhanced backscattering have a high applicability in medical measurements, which need to be conducted over very short distances.

Still, some fabrication techniques, such as depositing MgO nanoparticles on the fiber through chemical vapors, allow to achieve low loss fibers with attenuation of 0.4 dB/m at wavelength value of 1350 nm [71].

2.9 METHODS OF INTERROGATING MULTI-CHANNEL FIBERS

Generally, when several channels inside an optical link are multiplexed, their corresponding backscattered light signals arrive at the point of multiplexing at the same time. As a result, the overall Rayleigh spectrum obtained after interrogation is the overlapping, or superposition, of the backscaterrings of all the channels. There are two conventional ways to interrogate multi-channel configurations. The first one achieves true simultaneous interrogation by using separate detector modules for each of the channels. For instance, there is a multiparameter configuration that measures two different backscatterings, Raman and Rayleigh, across two cores of a fiber [72]. However, in addition to being more expensive and demanding in terms of hardware, such setups need to operate on fibers with low cross-talk [73]. The second technique interrogates the cores sequentially using a switch [74], which means that the acquisition time is increased due to the number of probes being equal to the number of multiplexed channels. However, time between switching cannot be shorter than the scan duration, which means that the fiber state captured by each probe may not be exactly the same. Hence, for applications concerned with real time monitoring, this technique would not be practical.

Moreover, most of these multiplexing implementations utilize FBGs; the spatial information can be decoded by monitoring wavelength peaks in the common spectrum. Such methods are inherently incompatible with the Rayleigh-based detection.

Of main interest are approaches based on OFDR. Ref. [32] proposes a setup for simultaneous measurement of temperature and strain with two multiplexed fibers. The technique implements bandwidth-division multiplexing, separating the frequency sweep into two subbands with bandpass filters and then interrogating the fibers with these subbands. Then, the two resulting backscatterings can be ana-

lyzed independently to extract temperature and strain along the two fibers. In another technique [75], two multiplexed fibers are connected to two weak reflector arrays. A delay line is also added to one of the fibers so that the reflectors from different arrays do not overlap. Then, the information from each fiber can be obtained by looking at the corresponding reflectors in the mixed spectrum. Still, the method is similar to the principle of FBGs, which means that only a quasi-distributed configuration is achieved. Another viable approach is to implement time division multiplexing (TDM) by arranging the multiplexed channels into a single propagation route, which enables the interrogation of all the channels within a single OFDR scan. For example, it was implemented with a configuration based on a multi-core fiber [76], where each core was coupled with its geometrical counterpart using microlenses; the pairs of the coupled channels were then linked with an SMF.

However, in the aforementioned approaches, the sensing region, determined by the parameters of the OFDR setup, needs to accommodate several channels. As a result, the measurable length of each channel is reduced by a factor equal to the amount of the channels.

Part I

SINGLE CHANNEL

The first part elaborates on the single channel implementation of distributed sensing. The considered application is acoustic detection.

3 ACOUSTIC SENSING

This chapter considers distributed sensing in the context of acoustic measurements, which need to be conducted with a configuration comprised of a single optical channel. The interrogation is performed with an OFDR device. Firstly, the phase-based detection, used as the basis of the work, is discussed. Due to this standard approach being prone to fading, an alternative phase difference estimation based on machine learning is proposed. The mathematical model used to create a synthetic training dataset is presented, which is followed by the description of two neural network architectures tested during the work. The first tests are conducted with another set of simulation. In the final part, the networks are tested on the real backscattering signals.

3.1 THEORETICAL FRAMEWORK OF PHASE-BASED ACOUSTIC DETECTION

The basis of the proposed methodology is the DAS technique based on estimating phase difference between the stressed fiber and the fiber at rest, reported in Ref. [77]. For completeness, this method, henceforth referred to as the standard approach, is briefly reviewed here.

Let us suppose that we have a fiber of length L. $B_{str}(z)$ and $B_{ref}(z)$ denote the backscattering signals collected from the stressed fiber and the corresponding signature, respectively, with the OFDR configuration. These signals are equivalent to their spectral domain representation due to the equivalence of distances and swept frequencies in OFDR:

$$f = \frac{2n_{eff}\sigma z}{c_0}, \tag{3.1}$$

where n_{eff} is the effective refractive index, σ is the sweep rate of the probe, and c_0 is the speed of light. The traces $B_{str}(z)$ and $B_{ref}(z)$ are segmented into spatial channels using a band-pass filter in order to localize the perturbation:

$$B_{str,n}(z) = W_n(z) \cdot B_{str}(z), \tag{3.2}$$

where the index n indicates a specific channel that corresponds to an isolated region on the fiber. $W(z)$ is a Tukey window whose limits, equivalent to cut-off frequencies, correspond to spatial positions where each channel starts and ends. From Eq. 3.1, the length of the window, or the isolated channel, depends on the acoustic bandwidth, B_a: $L_W = B_a c_0/(2n_{eff}\sigma)$. In essence, the acoustic bandwidth defines the maximum frequency detectable within the isolating window. It is

linked to the upper limit of the frequency sweep, f_{max}, divided by the overall number of the windows, N:

$$B_a = \frac{f_{max}}{N}, \tag{3.3}$$

with N defined as

$$N = \frac{L}{L_W}. \tag{3.4}$$

Eq. 3.3 indicates that the detectable frequency is constrained by the number of the isolating windows. Nevertheless, since the limits of frequency sweep in OFDR reach the order of THz, a frequency detectable within one window is still very high. In our case, the observed fiber length does not go beyond 100 m, which means that the method can offer the detection limit in the order of hundreds of kHz.

The isolated signals are converted back to time domain with inverse FFT. After that, the phase information, $\theta_n(t)$, can be extracted:

$$e^{j2\theta_n(t)} = \frac{b_{str,n}(t)}{b_{ref,n}(t)}. \tag{3.5}$$

$\theta_n(t)$ is actually the perturbation, $\varphi(t)$, acting on the fiber. From Eq. 3.4, it follows that the number of pairs $b_{str,n}(t)$ and $b_{ref,n}(t)$ contained in a single fiber profile is equal to N.

For each channel n, the phase in Eq. 3.5 is accumulation of the phases from all of the previous channels, including the current one. In order to access the information related only to the current channel, the differential phase needs to be considered:

$$\Delta\theta_n(t) = \theta_{n+\Delta n}(t) - \theta_n(t), \tag{3.6}$$

where $\Delta n = \frac{L_W + \Delta L}{\Delta z}$; ΔL is a distance between the starts of the consecutive windows, referred to as sensor spacing, and Δz is the spatial resolution of the OFDR setup.

The number of sampling points in a single isolated channel can be defined as:

$$N_t = \frac{4 L_W n_{eff} \sigma T}{c_0} = 2TB_a, \tag{3.7}$$

where T is the duration of the frequency sweep.

Compared to standard DAS approaches, the advantage of the described detection method is that it is not dependent on the scan rate of the interrogator. Instead, it performs the detection within the duration of a single frequency sweep, enabling the detection of higher frequencies. Although it also means that the detected signals have a very short duration, this is not a serious issue in the common DAS applications. For example, when detecting seismic activity, long observation times are not needed.

3.2 METHODOLOGY

The aforementioned high frequency detection method is prone to fading due to the division procedure. The proposed method involves estimating phase difference by means of machine learning. Specifically, a neural network trained with the fiber profiles under known stress can be used to correct the disruptions in the continuity of the observed scattering pattern. The idea is to calculate the phase difference directly from the stressed profile and the reference, without performing the computational steps in Eq. 3.5.

The first step is to create a synthetic dataset consisting of fiber profiles subjected to different perturbations. For this purpose, a mathematical model for simulating backscatterings of fibers under stress is presented, which is used to create the dataset for training. The next stage after that is the discussion of two different neural networks. However, before applying the methods to the real data, the measurements need to be corrected to remove the non-linear effect caused by the auxiliary interferometer of the OFDR.

3.2.1 *Mathematical model of perturbed fiber profiles*

It should be noted that in the considered case it is more preferable to train the models with the synthetic data rather than with the real backscattering signals. Each fiber has its own unique arrangement of the scattering centers. Thus, a large variety of different fibers would have to be interrogated while subjected to stress in order to obtain an effective and comprehensive dataset, which is not a practical approach. On the other hand, if the fiber profile can be mathematically modelled, it becomes possible to train the network with a diverse set of the scatterings, enhancing its ability to generalize. The performance of the model is not constrained by a specific interrogation setup, fiber type or conditions of the surrounding environment. Moreover, the true perturbation waveform is rarely available for real measurements, as DAS is typically used to detect frequencies.

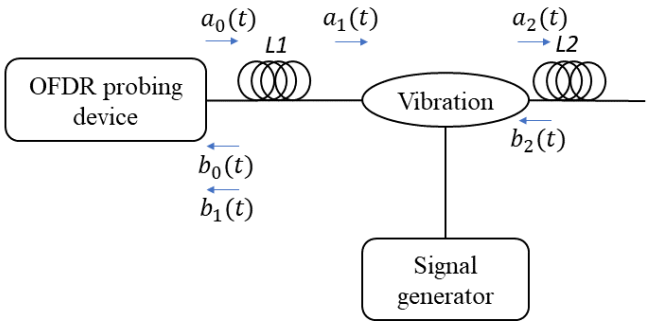

Figure 3.1: Schematic model of the perturbed fiber profile.

The external impact, which is an acoustic perturbation applied to the fiber, can be described with a diagram shown in Fig. 3.1. The

considered optical structure consists of two fiber links of lengths L_1 and L_2, with perturbations applied at a point between them.

Since the sensing region covered by the scan is not going to exceed the coherence length of the light source, the impact of the laser phase noise can be considered negligible. It is also worth noting that there is one perturbation location in Fig. 3.1. However, this condition is not going to limit the diversity of the samples in the training set. The detection in any point is done by evaluating the accumulated phase first. In each analyzed fiber section, the extracted phase difference is still a single waveform that could have been generated due to one perturbation point or multiple ones. Hence, it is sufficient to simulate fiber profiles subjected to different perturbations instead of the profiles with multiple perturbation points. The signal at the end of the unperturbed section of length L_1 is:

$$a_1(t) = e^{-j\beta_0 L_1} a_0(t - \beta_1 L_1), \tag{3.8}$$

where β_0 and β_1 are the propagation constant and the inverse group velocity defined as $\frac{2\pi n_{eff}}{\lambda_0}$ and $\frac{n_{eff}}{c_0}$, respectively. After passing through the point of perturbation and before entering the second link of length L_2, the light becomes:

$$a_2(t) = e^{j\phi(t)} a_1(t), \tag{3.9}$$

where $\phi(t)$ is the external perturbation applied to the fiber.

In the considered sensing configuration, the backscattering of the light is measured. In general, the backscattered form of a signal $a(t)$ can be expressed as:

$$B_L[a(t)] = \sum_k c_k e^{-j2\beta_0 z_k} a(t - 2\beta_1 z_k), \tag{3.10}$$

where c_k is the Rayleigh backscattering coefficient, and z_k is the location of a scatterer. As a result, the backscattering due to the first link is equal to:

$$b_0(t) = B_{L_1}[a_0(t)]. \tag{3.11}$$

Combining Eqs. 3.8-3.10, the backscattering due to the second link is:

$$b_2(t) = e^{j\phi(t)} e^{-j\beta_0 L_1} B_{L_2}[a_0(t - \beta_1 L_1)]. \tag{3.12}$$

Since the overall backscattering is measured at the start of the whole link, we need to obtain the backpropagation of the second link's backscattering. As it passes through the perturbation point again, the reflected backscattering becomes:

$$b_1(t) \approx e^{j\phi(t)} e^{-j\beta_0 L_1} b_2(t - \beta_1 L_1). \tag{3.13}$$

It is assumed that the phase variation in the applied perturbation is negligible over the course of the round trip conducted by the light through the second link. The total backscattering can be defined as the sum of the expressions from Eqs. 3.11 and 3.13:

$$b_{str}(t) = b_0(t) + b_1(t). \tag{3.14}$$

In order to obtain the reference signature of the fiber, the same steps in Eqs. 3.8-3.14 are repeated with setting $\phi(t)$ to zero.

3.2.2 *Neural networks for fading suppression*

Two network configurations are to be tested and compared with the standard detection in order to determine the most efficient model. Firstly, we need to briefly discuss the structure of the input and the output of the networks.

Depending on the length of isolated regions, one fiber profile can be separated into N channels, as per Eq. 3.4. A network processes each channel independently. Since each fiber profile contains two states, which are stress and reference, each channel is composed of two complex signals, $b_{str,n}(t)$ and $b_{ref,n}(t)$. Thus, the input has a shape $2 \times N_t$, where the first dimension corresponds to possible states and the second dimension is the size of each signal, which is defined by Eq. 3.7. The output of the network is the phase difference between the backscattering of the stressed fiber and that of the reference; as a result of processing, the 1st dimension of the input is reduced from 2 to 1. Consequently, there is an array of length N_t at the output.

3.2.2.1 *Network #1*

The initial input is further split into real and imaginary components, becoming $2 \times N_t \times 2$. The data is processed by a series of layers shown in the network diagram in Fig. 3.2, which is based on the LeNet architecture [78]. Firstly, the 2D-convolution of the real and imaginary parts is computed, reducing the dimensionality of the input, followed by another 1D-convolutional layer. Then, a pair of linear layers is applied to map extracted input features onto the output. Between each layer, the ReLU activation is applied.

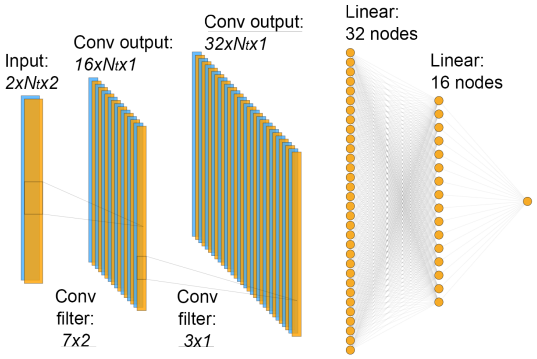

Figure 3.2: Layers of network based on LeNet.

3.2.2.2 *Network #2*

The model uses the same input as *Network #1*, but the shape is rearranged from $2 \times N_t \times 2$ to $4 \times N_t \times 1$. The architecture, which is based on the U-Net model [79], is replaced with a cascade of convolutional downsampling and upsampling blocks, as seen in Fig. 3.3(a). In the first convolutional layer, the number of input features is increased from 4 to 32. Fig. 3.3(b) presents a structure of each downsampling

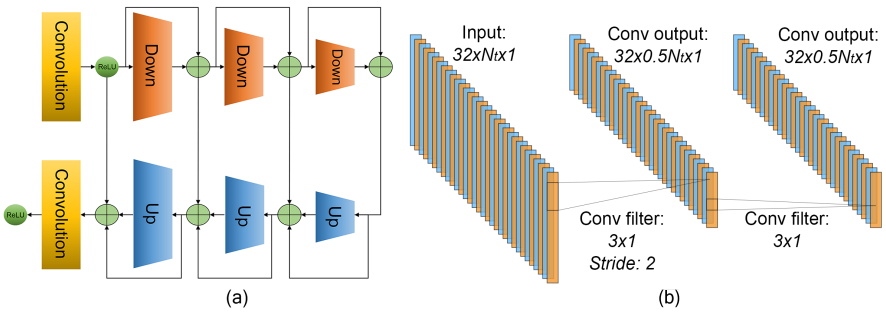

Figure 3.3: a) Layers of network based on U-Net; b) Architecture of single down-sampling block.

block, which is built from two convolutional layers that have one-dimensional kernel of length 3. The difference between these two layers is that the first one applies a stride equal to 2 to perform downsampling. Each upsampling block mirrors the structure of the downsampling block. However, in this case, the first layer performs transposed convolution to increase the amount of samples. All of the convolutional layer involved in the network have 32 nodes; the only exception is the last layer, as it has 1 node in order to have a single channel at the output. Each of the layers is followed by ReLU. The skip connections enable the network to capture both local and global features.

For all networks, the input, x_i, is normalized a $0-1$ range:

$$x_{i,normalized} = \frac{x_i - \overline{x}_-}{\overline{x}_+ - \overline{x}_-}, \tag{3.15}$$

where $\overline{x}_-$ and $\overline{x}_+$ are averages of the negative and positive values, respectively, in the set x the value x_i belongs to.

3.2.2.3 *Network training*

Pytorch was used as a machine learning framework. The networks were trained with 160 synthetic fiber profiles. More specifically, from the dataset, 70% and 30% of samples were used for training and validation, respectively. Training was conducted for 100 epochs with a learning rate of 0.001. MSE is used as an evaluation criterion. Adaptive moment estimation (Adam) is applied to optimize the network. In the simulated fiber profiles, the length of the fiber is 10 m, the isolating window is 2 cm, effective refractive index is 1.5, the scan duration is 0.1 s, and the frequency sweep rate is 12.5 THz/s. Hence, by substituting these values into Eq. 3.4, it is determined that a single fiber profile contains 500 isolated channels. Since perturbation is applied in the middle of the fiber, 250 of the channels are useful for the training. Thus, the overall number of fiber profiles, 160, results in the training set that contains 40000 traces.

Due to the constant kernel sizes, the selected parameters do not limit the networks to particular window sizes. Similarly to the standard method, the detection limits are scaled with the window size, in accordance with the Nyquist theorem.

3.3 EXPERIMENTAL SETTINGS FOR MEASURING ACOUSTIC VIBRATIONS

The OFDR device used in the work is Optical Backscatter Reflectometer (OBR) 4600 (Luna Innovations), with the sweep rate of around 25 THz/s. The central wavelength is 1550 nm, and the utilized bandwidth covers 80 nm. The overall sensing scheme is the same as in Fig. 3.1. For each of the two experimental measurements in the result section, the application point of the perturbation is specified. In the two experiments, the OBR mode was set to measure the backscattering over the lengths of 30 m and 70 m, respectively. The effective refractive index is 1.5.

3.3.1 *Correcting non-linearity of interferometer*

Similarly to Fig. 2.7, the utilized commerical OFDR system uses an additional interferometer to trigger the acquisition, ensuring the linearity of the frequency sweep. However, this linearizing interferometer causes misalignment between the time axes of the measured backscattering trace and the actual perturbation applied with a signal generator. The first step is to correct this misalignment.

A known stress of frequency f_c needs to be applied in the beginning of the fiber using a PZT. The previously described phase detection scheme is applied to extract the signal at one of the known stress application points. The result is the distorted signal $S(f - f_c)$ that experiences spectral broadening due to the effects of the linearizing interferometer. Then, this signal is processed with a homodyne demodulation, leveraging the knowledge about the applied stress, in conjuction with low-pass filtering to suppress the noise. The temporal axis of the modified signal is used to resample the backscattering traces, reducing the spread of the spectral broadening.

As an example, a 3 kHz perturbation was applied to the fiber. In Fig. 3.4(a), the detected perturbation without any compensation is shown. Then, this signal of known frequency was used to compensate the backscattering traces. The result is shown in Fig. 3.4(b), and it indicates that the spectral broadening was significantly reduced.

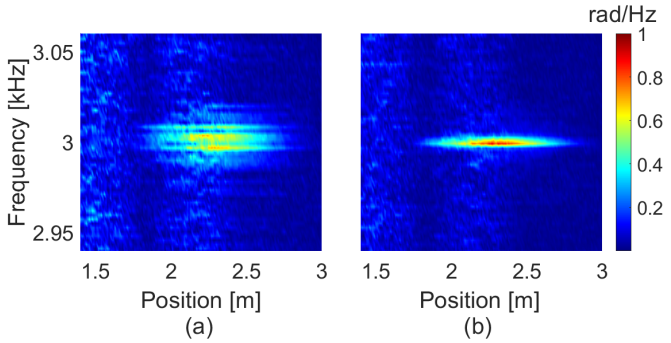

Figure 3.4: a) Perturbation detected using the raw signals b) Perturbation detected using the compensated signals.

3.4 RESULTS

3.4.1 *Simulated perturbations*

A new set consisting of 12500 channel traces, which were obtained from simulating 50 fiber profiles, was created to compare the proposed models between each other, as well as with the standard approach. The set contains the perturbations in the frequency range 0-1200 Hz and the amplitude range 0-1 rad. The number of frequencies contained in a signal ranged from 1 to 4.

To quantify the effect of noise, root mean square error (RMSE) between the detected phase difference and the respective nominal waveform, E, was estimated for each of the traces. Then, the cumulative distribution of the obtained error values was calculated: $F(E) = P(E \leqslant \varepsilon)$. In Fig. 3.5(a), a survival function $P(E > \varepsilon) = 1 - F(E)$ is plotted.

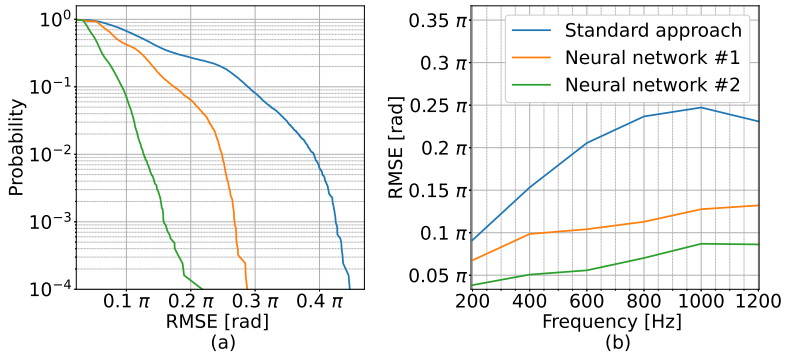

Figure 3.5: a) Survival function for the values of RMSE between the detected phases and the true phases; b) Relationship between RMSE and frequency.

Generally, *Network #2* performed better than the other methods, indicating a 6 dB improvement over the standard approach. *Network #1* is the second best method with a 3 dB decrease in error.

Fig. 3.5(b) uses the same RMSE metric to show the dependency of the accuracy on the perturbation frequency. In this case, each perturbation contained only a single frequency. The performances of the methods degrade as the perturbation approaches the detection limit, but the network consistently resulted in the error values lower than those of the standard approach.

3.4.2 *Real perturbation with single frequency*

Then, a sinusoidal signal with frequency of 41 kHz was applied to the 8 m position of a 12 m-long fiber. The sweep duration is 0.43 s. The length of the isolating windows is 75 cm, and the corresponding frequency limit is 45 kHz. The sensor spacing, ΔL, is 15 cm. The OBR time axis was corrected by applying a signal with frequency of 3 kHz.

As it can be seen from Fig. 3.6(a), obtained with the standard detection, there is a significant level of noise around the perturbation

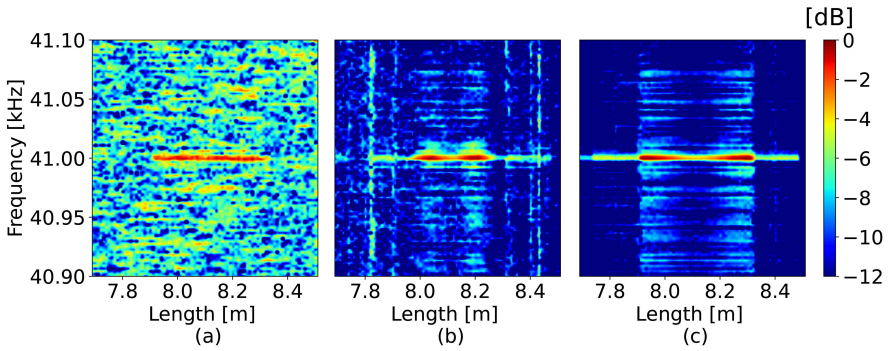

Figure 3.6: 41 kHz perturbation detected by a) standard method; b) Network #1 c) Network #2.

frequency. And yet, the neural networks are able to reduce the intensity of the deterioration caused by noise. As a result, the perturbation frequency becomes considerably more pronounced. To quantify the improvements, the SNR values in the perturbed region were measured and averaged. For *Network #1*, the SNR improvement over the standard approach is 6.9 dB. For *Network #2*, this improvement is equal to 7.3 dB. The noise reductions are also evident in Fig. 3.7 that shows the spectra of the perturbation extracted from the 8 m position.

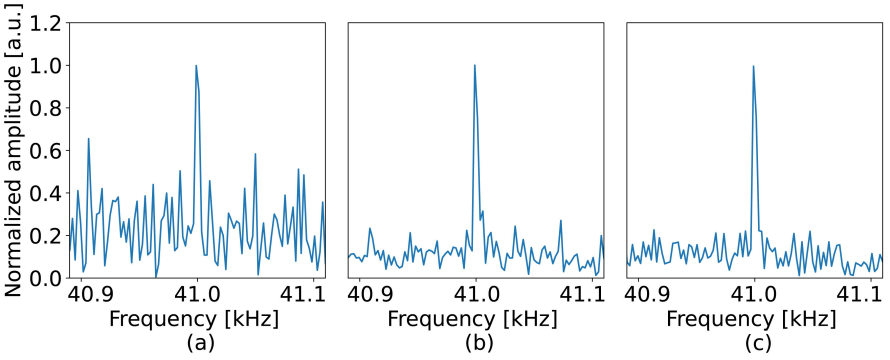

Figure 3.7: Frequency spectrum detected when measuring 41 kHz perturbation at 8 m by a) standard method; b) Network #1 c) Network #2.

3.4.3 *Real perturbation with multiple frequencies*

In the third test, a more complex perturbation, as shown in Fig. 5, was applied at the 15 m position of a 50 m-long fiber. The signal function of the perturbation is

$$A_1 \sin(2\pi f_1 t) + A_2 \sin(2\pi f_2 t) \cdot \exp(-0.5(t-\mu)^2/\Lambda^2), \qquad (3.16)$$

where $A_1 = 27.69 \cdot 10^{-2}$, $A_2 = 18.46 \cdot 10^{-5}$, $f_1 = 150$ kHz, $f_2 = 120$ kHz, $\mu = 0.5$ ms and $\Lambda = 0.4$ ms.

The length of the isolated windows is equal to 4 m and the frequency limit is 250 kHz. The sensor spacing, ΔL, is 25 cm. The sweep duration is 0.22 s. The frequency used to correct the OBR misalignment is 150 kHz, which is within the detection limit. The frequency domain traces obtained for each spatial channel are plotted on the

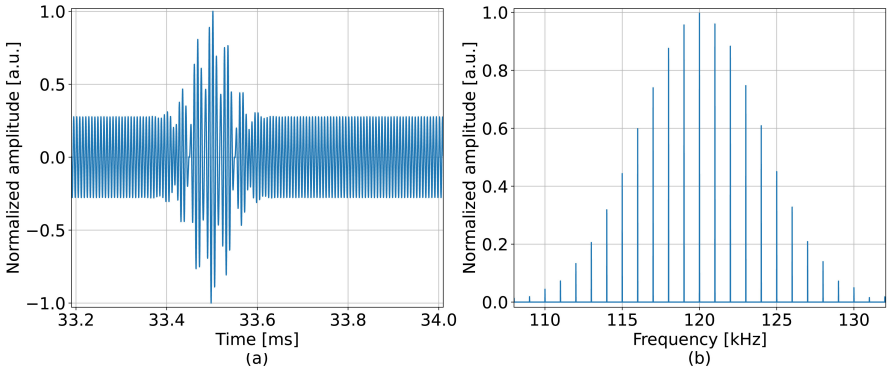

Figure 3.8: Perturbation of increased complexity applied experimentally a) in time domain; b) in frequency domain.

2D-maps shown in Fig. 3.9; for better visualization of the results, only subbands of 100 Hz around the perturbation frequencies are plotted.

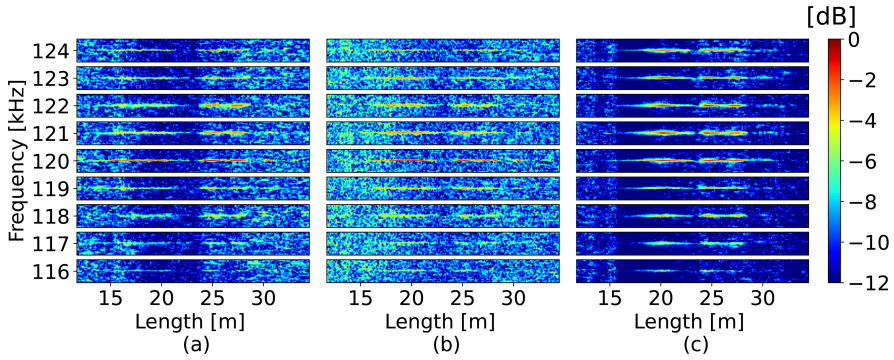

Figure 3.9: Perturbations of increased complexity detected by a) standard method; b) Network #1; c) Network #2 (demonstrated spectral width around each component is 100 Hz).

In this experiment, *Network #1* performed worse than the standard method, which is reflected in the very strong noise pattern from Fig. 3.9(b); the average SNR is deteriorated by 2 dB. Networks #2 was more consistent with the previous results, achieving 5.4 dB improvement in SNR over the standard method. These observations can be corroborated by examples of the detected perturbations from Fig. 3.10, which were collected at the 20 m position.

It can be inferred that Network #2 is the most efficient option, since it provided better results for both experimental measurements, as well as during the simulations. Even though *Network #1* showed efficient performance in the simulations and the first experimental test, it was not able to surpass the detection accuracy of the standard approach in case of the more complex perturbation, which implies that the model was overfitted during training. Hence, *Network #2* is the model that offers the most consistent performance.

3.5 CONCLUSION

In this chapter, the machine learning methodology was applied to suppress fading effects in the phase-based DAS measurements con-

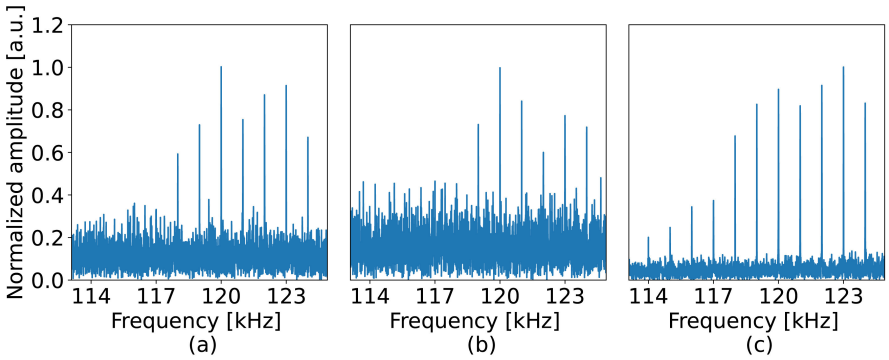

Figure 3.10: Frequency spectrum detected when measuring perturbation of increased complexity at 20 m by a) standard method; b) Network #1 c) Network #2.

ducted with OFDR over a single channel. A mathematical model for simulating the backscattering profiles of acoustically perturbed fibers was presented. It was demonstrated that a network for phase detection modelled after the U-Net architecture can be successfully trained with a synthetic dataset and subsequently achieve high accuracy even when processing the real backscattering profiles. The performance of the neural network achieved 5.1 dB improvement over the standard method.

Part II

MULTI-CHANNEL

The second part elaborates on the multi-channel implementations of distributed sensing. The considered applications are thermal ablation and shape sensing.

4

THERMAL ABLATION

This chapter elaborates on the application of optical fibers in temperature monitoring. The opening part describes what is the procedure of thermal ablation. Necessary biosensing context is provided. The next section reviews the well-known spectral correlation analysis method (SCA), which can estimate the stress applied to the fiber by comparing its signature backscattering and the stressed backscattering. Then, we proceed to discussing methodology, and, in particular, how time division multiplexing can be used to interrogate several fibers and measure thermal pattern in a two-dimensional manner. Necessary modifications in the form of enhanced backscattering are discussed there as well. The experimental part demonstrates the results obtained during real time monitoring of different thermal ablation sessions. In each session, different solutions were applied on the surface of the tissue to facilitate heating. The backscattering measurements assist in determining the solution that results in the most efficient heating.

Before proceeding, it is important to clarify the issue regarding fading, which was one of the major focuses in the previous chapter that considered single-channel sensing. However, as mentioned before in Chapter 2.5, the fading problem does not need to be addressed in the case of multiple channels, since the information lost at some points in one of them can be compensated by the information from the other channels. Moreover, the considered multi-channel schemes are based on the correlation method, which is going to be discussed in detail in this chapter. This method is intrinsically less susceptible to fading, in contrast to the previously considered phase-based approach.

4.1 THEORETICAL FRAMEWORK

4.1.1 *Thermal ablation review*

In thermal ablation, abnormal tissues are reduced or removed by subjecting them to heat [80]. A small incision needs to be made in order to apply the heating catheter to the treated tissue. Hence, it is a minimally invasive process, and treatment of tumors is one of its primary applications. Compared to conventional alternatives among surgical methods, thermal ablation is particularly useful when the targeted areas consist of several small tumors or when they are difficult to access. Moreover, the damage to healthy tissue surrounding the ablated regions is minimized, which also leads to a quicker recovery of patients.

There are different ways to conduct these thermal treatments, including high-intensity focused ultrasound, microwave, laser and radiofrequency ablation (RFA). The choice of treatment depends on the

type of targeted tissue. For instance, the RFA process is commonly used to treat tumors of liver and kidney. In RFA, alternating electrical currents of high frequencies flow through the catheter, or the electrode, and encounter the resistance due to the tissue, which results in the heat generation. Depending on the applied temperature level and the duration of the process, the tissue can undergo vaporization or coagulation, be partially or completely removed.

In order to achieve the required goals during the procedure, thermal variations must be precisely controlled, necessitating the need for accurate temperature monitoring tools. A common option is magnetic resonance imaging (MRI), but, in addition to being a very costly solution, it also cannot offer high detection speeds. Furthermore, due to the requirements of being used in minimally invasive procedures, the sensors must be sufficiently compact. Another well-known approach is to use a thermocouple, but it performs point measurements, and its metallic composition can have an unwanted impact on the heating therapy. Instead, intrinsic properties of optical fibers have made them a viable alternative to those conventional methods. More specifically, modern reflectometry devices enable high acquisition rates, which means that it is possible to conduct measurements in real time, and distributed sensing configurations offer high spatial resolutions. Optical fibers also do not interfere with the heating process, and they are not susceptible to the effects of electromagnetic interference.

Of particular interest during the monitoring of ablation are regions heated to 42°C and 60°C, which are the temperatures of cytotoxicity and thermal damage, respectively [80]. When the tissue reaches 42°C, cancer cells become sensitive to thermal treatment. Moreover, at this stage, the ablation damages cancer cells, but does not negatively affect healthy regions of the tissue. At 60°C, the tissue starts to become more solid as the coagulation process initiates. Moreover, this temperature can lead to the destruction of cells within the ablated region.

It is possible to further facilitate the heating process. Certain solutions deposited on the surface of the ablated regions can increase or decrease the intensity of thermal therapies, as well as widen the propagation of heat over the tissue surface. In particular, solutions containing metallic nanoparticles significantly improve the ablation efficiency. For instance, they can decrease the resistance of the tissue during the application of currents through the catheter, which results in a more gradual heating. An increase in the resistance that is too rapid also results in the quick deactivation of the generator. Hence, carefully selected solutions allow to exert more control over heating duration. Moreover, due to the heating becoming more uniform, we can manage to ablate larger areas before the deactivation.

Still, the heating eventually stops when the resistance due to the tissue becomes too high, which is a process that cannot be controlled by the user. The exact duration of the heating cannot be predicted, which means that the ablation procedure needs to be continuously monitored. Hence, the real time monitoring is required, so that the ablated regions can be observed right until the end of the thermal treatment.

4.1.2 *Spectral correlation analysis*

In this part, a general case of spectral correlation analysis (SCA) [81] is considered. It is a well-known technique used in distributed sensing to extract information from SMF.

The core principle of the technique is that RI variation, Δn, induced by a perturbation, results in a frequency shift, Δf, somewhere along the backscattering spectrum of FUT:

$$\frac{\Delta n}{n_0} \approx \frac{\Delta f}{f_0} \tag{4.1}$$

where n_0 is the RI of the unperturbed fiber, and f_0 is the central frequency. However, due to elasto-optic and thermo-optic effects, reviewed in Chapter 2.3, the RI change can be caused by both strain and temperature [82]:

$$\frac{\Delta n}{n_0} \approx -0.78\Delta\epsilon, \quad \frac{\Delta n}{n_0} \approx -6.92 \cdot 10^{-6}\Delta T. \tag{4.2}$$

Intrinsically, it is not possible to resolve whether the RI alteration is in response to strain and temperature. Hence, if the goal is to measure one of these stimuli, the experiment has to be designed in a way that minimizes the presence of the other one. In the current case, it is the strain fluctuations that need to be minimized. Hence, in the conducted experiments, the array of fibers will be spatially fixed to minimize the impact of strain on the measurements.

Let us suppose that backscattering trace $s_{ref}(z)$ is the signature of a fiber collected when it is straight and unperturbed, and $s(z)$ is the backscattering of the same fiber under some stress. The gauge length L_W and the set of delays Δz are selected. Then, the signature and the stressed trace are separated into smaller subsections $s_{ref}(z, z + L_W)$ and $s(z + \Delta z, z + \Delta z + L_W)$, respectively. The Fourier-transform is applied to these subsections. So, for each spatial position z, the transformed signature trace is cross-correlated with the transforms of the delayed stressed traces. As a result, the volumetric dataset $C(z, \Delta z, \Delta f)$ is obtained, with the first dimension representing distance, the second one corresponding to the number of delays considered for each subsection, and the third one being the frequency axis of the cross-correlation. A spatial alignment between the subsections is indicated by the peak along the Δf axis. The value of Δz corresponding to the best correlation indicates the difference between the group delays at the points where the signature and the stressed subsections start. The position of the peak corresponds to the spectral shift induced by the RI of the fiber changing due to the applied perturbation, in accordance with Eq. 4.1 and Eq. 4.2. Thus, by calculating the maximum of $C(z, \Delta z, \Delta f)$ along the second dimension, the spectral shift and, subsequently, the temperature change are determined with respect to the distance along the fiber: $SCA[s_{ref}(z), s(z)] = \Delta T(z)$.

While the spatial resolution of the raw backscattered data, dz, is determined by a laser used in the OFDR setup, the actual spatial resolution of the distributed sensing procedure is the gauge length set

in SCA. An increase in the gauge length lowers the noise, but the localization accuracy is reduced. Meanwhile, dz has a direct impact on the quality of the cross-correlation, since it determines the resolution of the Δf axis. The method can be further improved by oversampling the data during the Fourier-transform and by using parabolic peak tracking when estimating the location of the maximum during cross-correlation.

Recalling Chapter 2.2.2, the OFDR provides the backscattering traces of two polarization states. SCA can be conducted with different combinations of polarizations to select the one with the highest quality of correlation.

4.2 METHODOLOGY

4.2.1 *Time division multiplexing implemented with optical fibers*

When several optical channels of the same length, L_f, are coupled to an SMF, their backscattering traces are mixed after arriving at the point of multiplexing at the same time. Time division multiplexing (TDM) approaches are based on modifying the light propagation across the channels in a way that avoids the superposition of the backscattering signals. TDM can be implemented by delaying each backscattering by a certain time, and conventional SMFs can be used as delay lines.

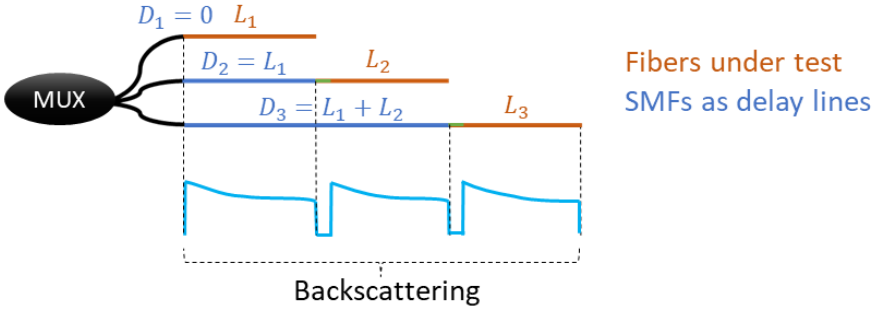

Figure 4.1: Multiplexing that enables TDM.

The first of the multiplexed channels does not need to be delayed. For each of the next channels, the length of the delay line is increased in steps equal to the length of the single channel, as illustrated in the Fig. 4.1. This way, it is ensured that the detector fully receives the backscattering due to one channel before receiving the next one. Since every sensing fiber has the same length L_f, the length of the delay line can be expressed as

$$D_i = (i-1)(\Delta l + L_f), \tag{4.3}$$

where Δl is a very small region which is needed to clearly discriminate the end of each fiber in the spatial domain trace. As the light probe sequentially travels through all of the multiplexed links, the overall propagation length becomes

$$L_{total} = D_N + L_N = N(\Delta l + L_f). \tag{4.4}$$

Hence, the sensing range of OFDR needs to cover the length L_{total} from Eq. 4.4. Although the multiplexing is achieved at the expense of sensing range, medical applications usually do not require to operate fiber sensors over long distances [70].

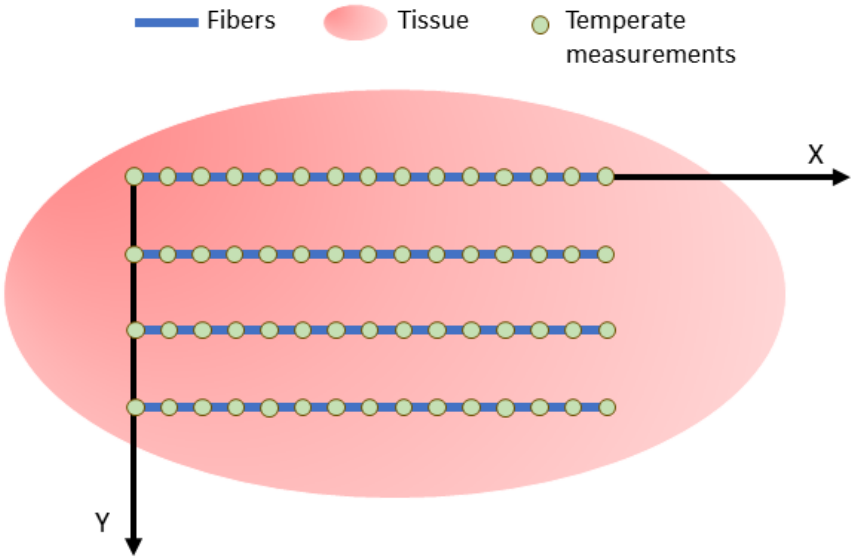

Figure 4.2: Array of fibers set to measure thermal changes across the tissue.

During the measurements, the sensing fibers need to be placed on a tissue in a pattern shown in Fig. 4.2. The backscattering signals collected from the multiplexed array of fibers will have a sawtooth shape, as indicated in Fig. 4.1. As usual in distributed sensing, the signature is collected first, while the fiber is in the initial thermal state. Then, the backscattering of the fiber subjected to heating can be collected. The SCA is applied to the signature and the measured backscattering, extracting the corresponding temperature change along the spatial axis of the multiplexed backscattering: $SCA[s_{ref}(z), s_{measured}] = \Delta T(z)$. Then, since the spatial points that correspond to each fiber can be inferred by looking at the backscattering in Fig. 4.1, the thermal changes experienced by each fiber can be separated from the overall trace $\Delta T(z)$. As a result, we obtain N number of spatially distributed temperature waveforms that reflect the arrangement in Fig. 4.2, with N representing the number of multiplexed fibers. These curves can be arranged as a 2D array.

4.2.2 *Fibers with enhanced Rayleigh backscattering*

Still, we need to be able to distinguish the backscattering of the sensing channel from that of the SMF delay lines. It is possible if the backscattering due to the sensing channel has a gain that increases the magnitude of the signal to a level considerably higher than the SMF lines. This amplification can be achieved by doping a silica-based fiber with rare earth materials, which is also one of the common ways to build amplifiers for lasers. More specifically, the introduction

of dopants increases the density of scattering centers, amplifying the backscattering gain as a result.

An efficient technique is to embed a rare-earth element into oxide nanoparticles, which can be implemented with modified chemical vapor deposition (MCVD) [71]. A precursor gas is produced from an alcoholic solution containing the dopants. Inside a rotating glass tube, which serves as a preform, the gas interacts with silicon-precursor gases. High temperature is applied to the tube, which leads to the decomposition of the gases. As a result, the dopants are incorporated into the growing glass structure. The composition of the fiber core is defined at this stage. Then, the preform is drawn into a fiber link that has the required dimensions. Finally, the resulting optical structure undergoes a period of steady cooling, which is followed by adding a protective coating layer. The advantage of the technique is that the doped fibers are considerably less fragile compared to, for example, methods where the glass substances are melted and drawn directly.

For the fiber used in this work, the precursor gas was produced by mixing $ErCl_3$ and $MgCl_2$. Hence, the manufactured fiber core contains MgO-based spherical nanoparticles, which were chosen due to a particularly high gain amplification [83]. For instance, the gains in the range 32-47 dB were previously reported [84]. Alternative compositions, such as Ge-doped fibers, offer the gains that are around 10 dB less. Moreover, as MgO-doped fibers become more common, their ease of use also improves, approaching the levels of commercial SMFs. For example, the splicing points in such fibers now have a loss lower than 0.1 dB. In addition, hundreds of meters of doped fibers can be spooled during the drawing process.

However, the side effect of the amplified gain is that the backscattering also attenuates at a higher rate due to the increased density of scattering centers and the absorption of photon energy by the dopants, which puts a constraint on the observable fiber length [85]. Let us denote the ratio of the enhanced backscattering power to the delay line power as the signal-to-interference ratio (SIR). At some position z, the SIR of each channel is equal to [84]

$$\mathrm{SIR}(z) = \mathrm{G} - 2\alpha z - 10\log_{10}(\mathrm{N}-1), \tag{4.5}$$

with G as the backscattering gain, α as the attenuation rate, and N as the number of multiplexed channels. Hence, depending on the required SIR, the length of each channel is limited to

$$\mathrm{L}_{f,max} = \frac{\mathrm{G} - 10\log_{10}(\mathrm{N}-1) - \mathrm{SIR}}{2\alpha}. \tag{4.6}$$

It is evident that the observable length of each channel decreases with the number of multiplexed links.

4.3 EXPERIMENTAL SETUP FOR MEASURING THERMAL PATTERN OF A TISSUE

4.3.1 *Distributed sensing configuration*

The schematic representation of the setup and its real laboratory implementation can be seen in Fig. 4.3. As in the previous chapter, OBR 4600 (Luna Innovations) is used to perform OFDR measurements.

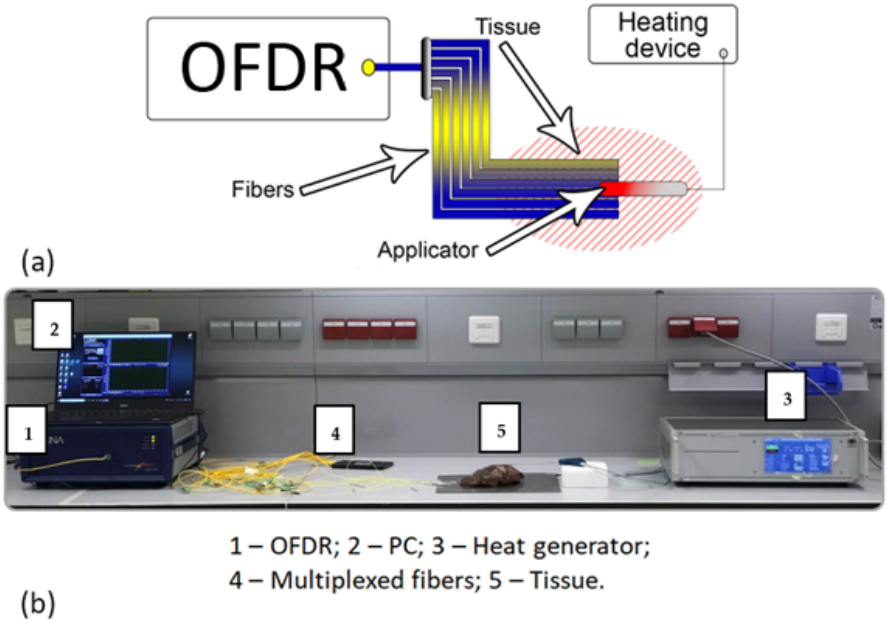

Figure 4.3: a) Schematic of the setup; b) Laboratory configuration.

The MgO-doped fiber was supplied and produced by the group led by prof. Wilfried Blanc from Université Côte d'Azur. The overall diameter of the fiber is 125 µm, with the core diameter equal to 10 µm. It was separated into six links. They were multiplexed with a 1x8 coupler; each fiber was spliced with a commercial SMF acting as a delay line. The splices, made with Fujikura 12-S, did not cause significant losses beyond the level of 0.1 dB. Fig. 4.4 shows the overall backscattering of the resulting TDM-based setup. The Rayleigh trace of each channel is clearly distinguishable, and the amplification gains with respect to the SMF delay lines are higher than 40 dB. The highest attenuation rate is equal to 83 dB/m. The length of 38 mm, counting from the tip, was chosen as the measured region for each fiber. The SIR value monitored at the tip of each fiber is at least 33 dB, which means that, in accordance with Eq. 4.6 the maximum length of each channel is higher than the sensing range provided by the OFDR device. Thus, the selected length is well within the stipulated constrains.

The sensing fibers were placed on a tissue in 2D fashion, as shown in Fig. 4.3(a). There was a distance of 4 mm between the fibers in the vertical direction. The backscattering signal in Fig. 4.4 also corresponds to the signature of the fiber, which was collected under room temperature. During the experiments, SCA was applied to extract

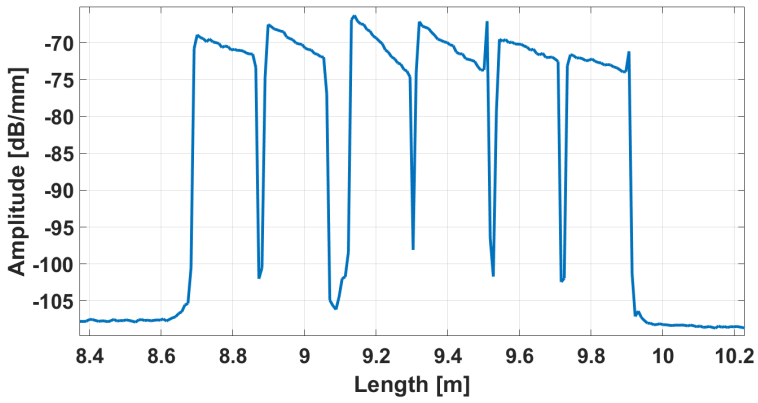

Figure 4.4: Backscattering of multiplexed fibers.

temperature variations with respect to this signature, with the gauge length set as 2 mm.

However, before the main measuring procedures, the thermal sensitivity of the utilized custom fiber needed to be obtained by performing a calibration step. The fiber was submerged into a gradually heated water tank. At the same time, temperature changes were registered with a thermocouple. Every 30 seconds, the fiber was interrogated with the OFDR device. The resulting spectral shifts were measured and compared with the respective thermocouple readings, obtaining the thermal response graph in Fig. 4.5. The slope indicates the value of the thermal sensitivity equal to 9.4pm/°C, which is close to the sensitivity of commercial SMFs.

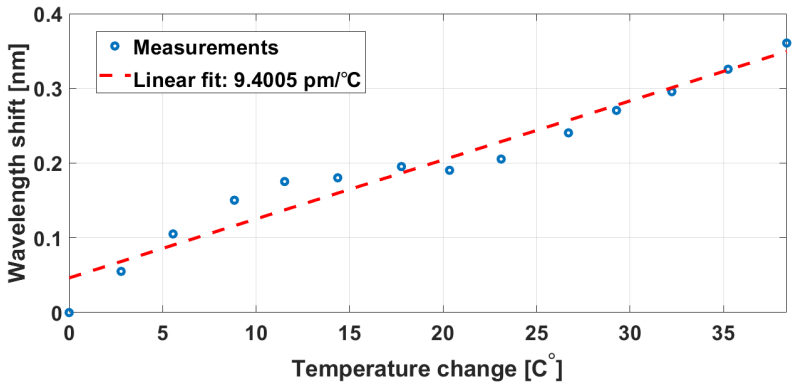

Figure 4.5: Thermal calibration curve.

For thermal ablation, the OBR was used in the spot scan mode to get better acquisition rate when monitoring thermal evolution with respect to time. In this mode, the wavelength range of the sweep is equal to 40 nm. In the scan mode, a particular region in the signature backscattering, containing the concatenated fibers, was selected beforehand. Then, the OBR performed continuous sweeps of this region only, with the benefit of the increased acquisition rate. The maximum length that can be swept in this mode is equal to 1.2 m, which is what was used in the experiments.

For each scan, the measurements along the channels can be rearranged as a 2D array to mirror the actual placement of the fibers.

Then, interpolation along Y-axis can be applied, with a step size equal to 0.4 mm.

4.3.2 *Thermal ablation parameters*

A microwave and radiofrequency generator (LeanFa Srl, Ruvo di Puglia, Italy) was used to apply heating to the tissue. The frequency of the applied current was set to 450 kHz, and the power of the generator was 60 W. The safety mode of the generator was activated, ensuring deactivation if the resistance of the tissue exceeded 800 Ω. The length of the electrode was 16 cm, and the diameter was 3 cm.

Before the start of the measurements, the sample tissue was thermally stabilized by leaving it in the laboratory environment for several hours. Thus, its initial state was comparable to the backscattering signature.

A porcine liver was used as a sample tissue for the experiments. Six thin cuts were made on its surface for the placement of fibers. This way, their positions were fixed to minimize fluctuations due to the strain. Except for the sessions when the generator stopped automatically due to the resistance of the tissue, the heating was applied for 1 minute, but the monitoring was continued for an additional minute to record the thermal behavior during the cooling period.

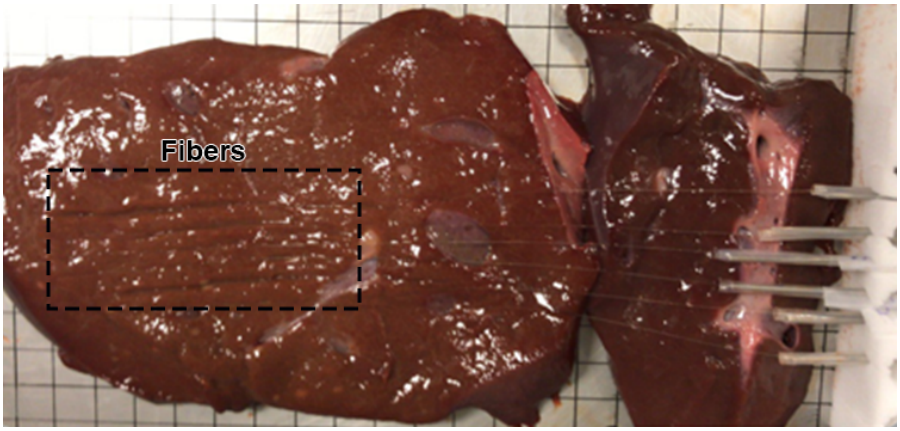

Figure 4.6: Placement of fibers on the sample.

We tested several solutions that can facilitate the heating process. The goal was to determine the solution that results in the most efficient ablation. More specifically, agarose solutions containing silver nanoparticles were tested for the facilitation of heating. Two concentrations were tested, 5 mg/ml and 10 mg/ml. The measurements were also conducted for the case of dry heating when no solution was applied. For each particular case, the measurements were repeated three times.

Solutions for testing were prepared by dissolving metallic-based powder in distilled water, followed by heating and stirring by means of a centrifuge. However, the detailed preparation of solutions containing metallic nanoparticles, which can be found in Ref. [86], is outside of the scope of the current work, which focuses on the interro-

gation methodology. The sizes of formed nanoparticles, as confirmed by an electron microscopy, ranged between 30 and 50 nm.

4.4 RESULTS OF REAL-TIME MONITORING OF THERMAL ABLATION

Temporal progressions of the thermal maps can be seen in Figs. 4.7-4.8. The examples obtained during one round (out of three) of trials are shown.

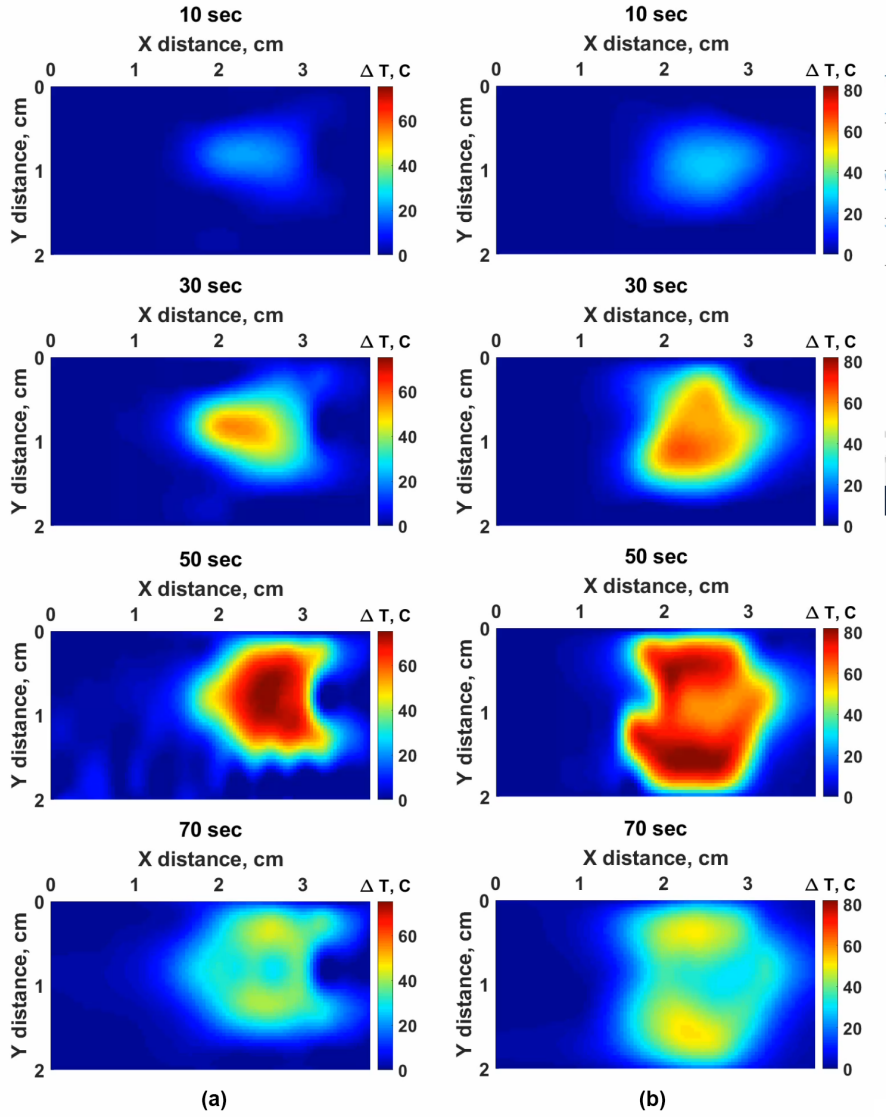

Figure 4.7: Thermal patterns observed with a) dry heating; b) heating facilitated by 5 mg/ml silver nanoparticle solution.

Upon visual inspection of Fig. 4.7, it is evident that, compared to the heating of tissue without any solutions, the silver solution increases the ablated area, while also achieving higher temperatures. Hence, in nanoparticles-assisted heating, more tissue is subjected to thermal treatment at a faster rate while avoiding very abrupt temperature rises that would result in the deactivation of the generator. As it can be seen, the patterns themselves are not always uniform, which

can be attributed to inhomogeneities in the surface of the treated sample. For instance, different fat percentages can cause these irregularities in the tissue. The state of the catheter is also a contributing factor, and as it is used for all of the sensing sessions, its conductive qualities may slightly deteriorate.

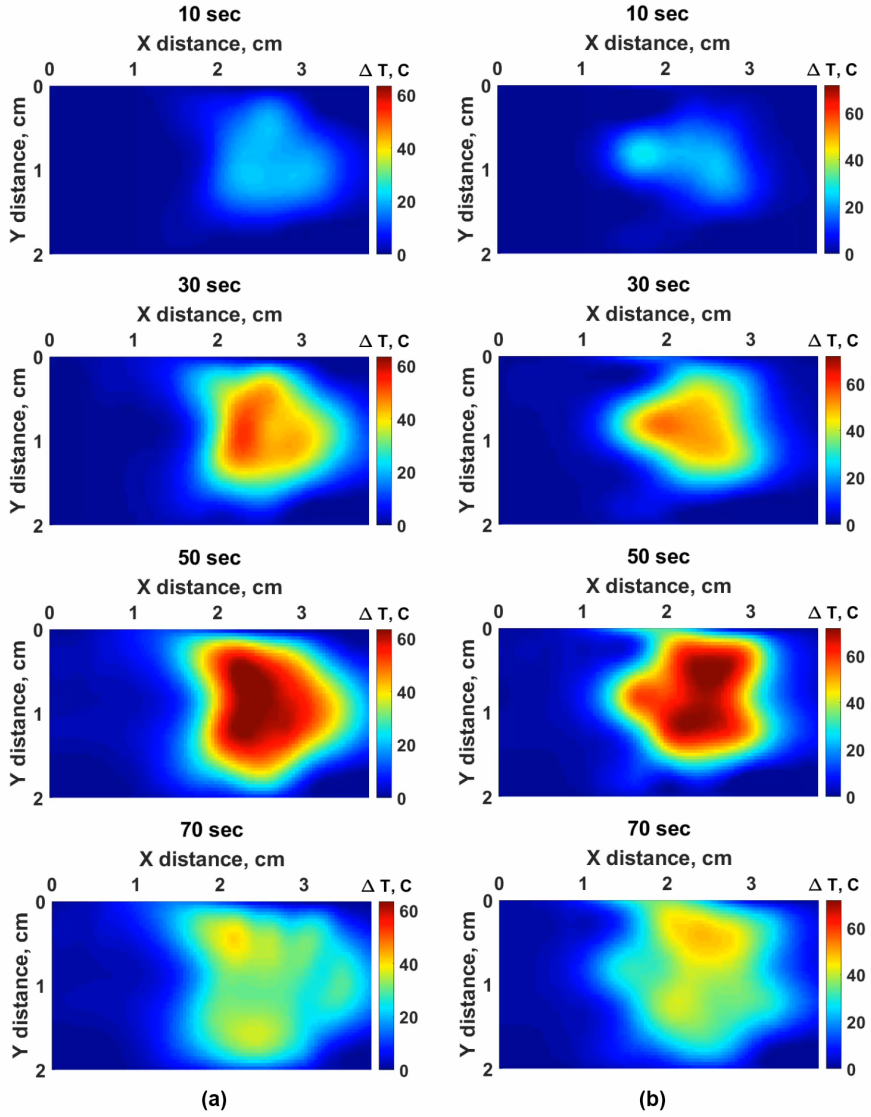

Figure 4.8: Thermal patterns observed with heating assisted by silver nanoparticle solutions with concentrations of a) 10 mg/ml; b) 20 mg/ml.

Temporal progressions of thermal maps in Fig. 4.9(a) were obtained for the 10 and 20 mg/ml concentration of the silver nanoparticle solution. However, while still showing improvements over heating with no solution, the heating procedures were not as efficient as in the case of the lower concentration of 5 mg/ml.

In particular, we are interested in the regions that are heated to 42°C and 60°C, as the main therapy stage occurs in-between these temperatures. 2D-maps corresponding to the sequential OBR scans allow to track a time instant when these temperatures are reached. Hence, for each session, we can identify the time instant when the

areas subjected to the temperatures of interest were the largest. The examples of the resulting maps, plotted for sessions in Fig. 4.7, can be seen in Figs. 4.9-4.10.

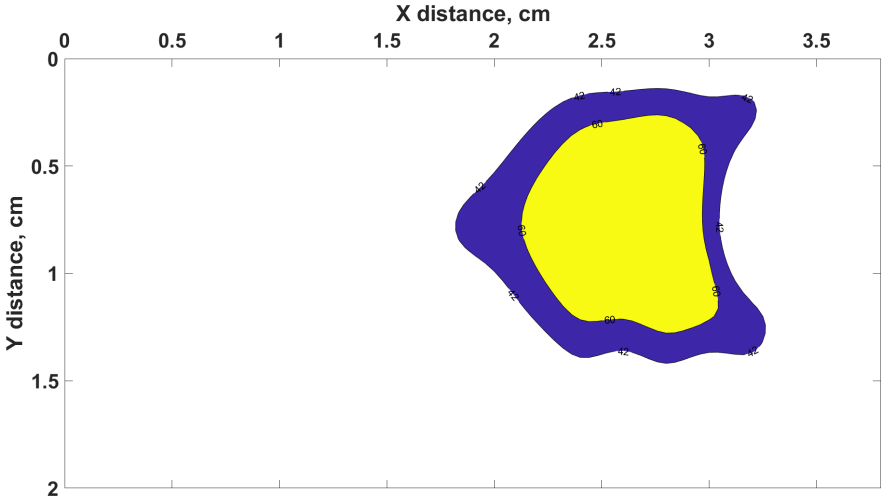

Figure 4.9: Ablated areas that reached 42°C and 60°C with dry heating.

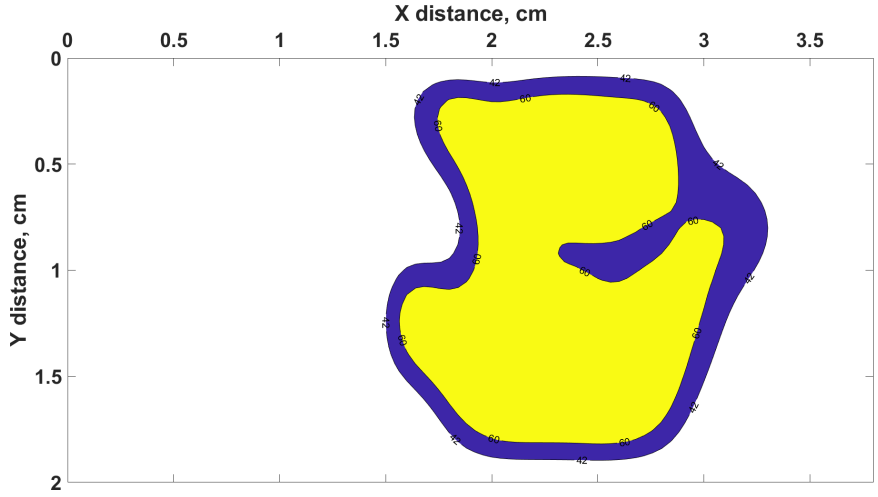

Figure 4.10: Ablated areas that reached 42°C and 60°C with heating assisted by 5 mg/ml silver nanoparticle solution.

From the heating patterns in Figs. 4.9-4.10, the areas of the tissue that reached temperatures of 42°C and 60°C are quantified.

For each of the solutions, the average values across the 3 conducted trials were calculated. The resulting data is summarized by bar plots in Figs. 4.11-4.12. Error bars represent the standard deviations registered for each solution across 3 rounds of trials.

In all of the measurements, the heating process managed to reach temperatures beyond 60°. As indicated by the spread of the error bars, the standard deviations were lower for all of the cases of assisted heating, improving on the consistency provided by dry heating. The 5 mg/ml silver solution resulted in the highest area of ablation. For 60°C, the ablated area was effectively doubled with respect to the case of dry heating. Moreover, the areas heated to 60°C were consistently

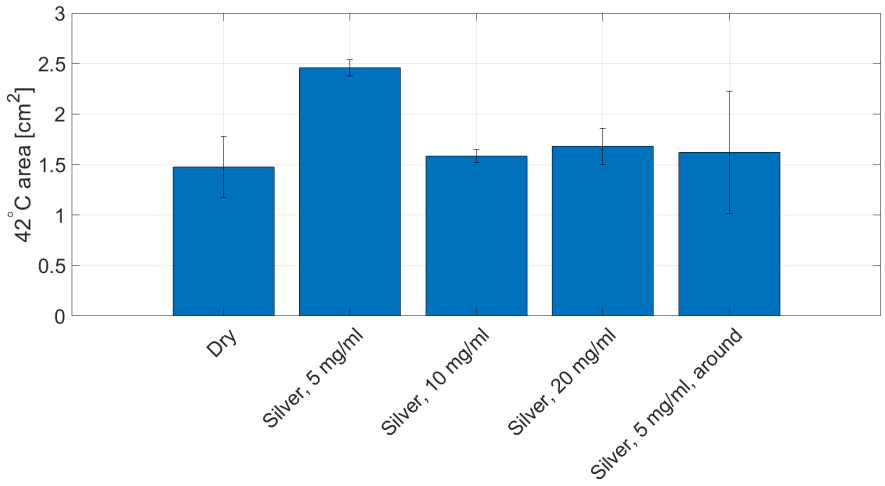

Figure 4.11: Bar plots of ablated ares heated to 42°C.

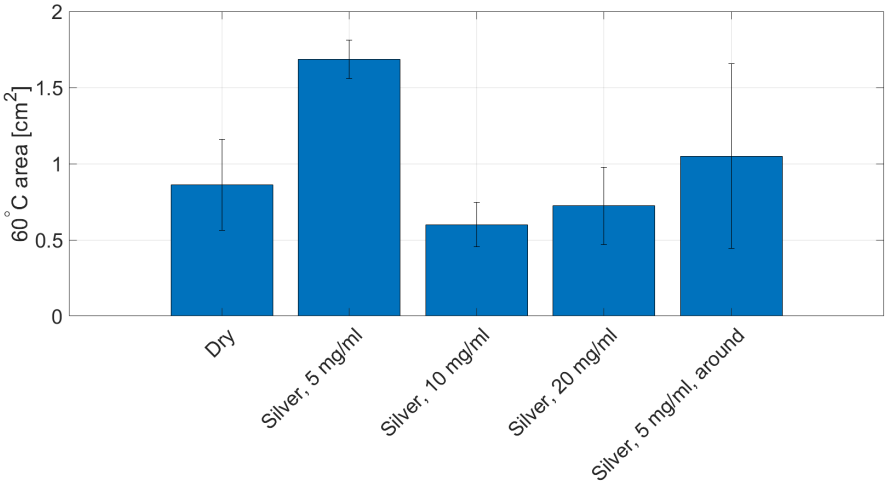

Figure 4.12: Bar plots of ablated ares heated to 60°C.

higher than 1 cm^2. However, other concentrations did not maintain their heating efficiency after reaching 42°, as the areas ablated at 60° were even smaller than in the case of dry heating.

Moreover, after the 5 mg/ml silver solution proved to be the most efficient, a different deposition method of it was considered; the nanoparticles were placed around the application point, as opposed to the central deposition implemented before. The depositions are schematically represented in Fig. 4.13. The resulting areas are shown in the

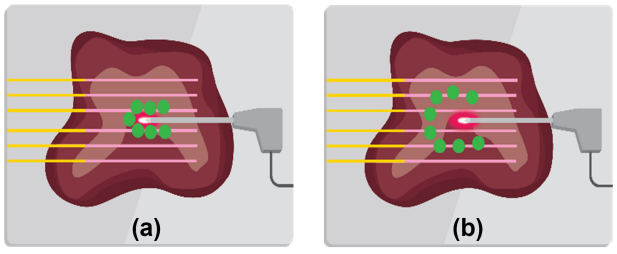

Figure 4.13: Deposition of silver nanoparticles (green) a) in a center, coinciding with the catheter application; b) around the catheter.

same bar plots in Figs. 4.11-4.12. However, this particular way of heating resulted in smaller regions of ablation. In addition, there was less consistency in the results, as indicated by the standard deviation.

4.5 CONCLUSION

In this chapter, optical fibers were used as real-time monitoring tools during the thermal ablation tests. The goal of the experiments was to identify the silver solution that facilitated the heating the most. The solution containing silver nanoparticles at concentration of 5 mg/ml proved to be the most efficient option.

It was demonstrated that optical fibers is an efficient temperature monitoring tool that can be used in real time. Most importantly, multiplexing capacities of the fibers were explored by implementing a 2D-array sensor. The multiplexed configuration was built by concatenating fibers with enhanced backscattering into a sequential link, leveraging the TDM principle. The improved backscattering enables high SNR values, although TDM leads to a decrease in effective sensing range.

5 SHAPE SENSING

This chapter considers the implementation of shape sensing with optical fibers. This application also requires to multiplex several optical links.

The chapter starts from the description of techniques used as a basis for the work. Firstly, SCA is discussed in the context of strain measurements; it is commonly used in commercial devices to estimate strain from the backscattering signals of the stressed fiber. It is followed by discussing a conventional interrogation setup, used as the benchmark in the chapter, that uses switching to sequentially probe the multiplexed channels. A numerical algorithm that needs to be applied in order to reconstruct the shape of the stressed fiber is also reviewed.

Then, the proposed methodology is presented. This part shows how SCA can be extended to facilitate the simultaneous interrogation of the multiplexed channels. The model for characterizing the noise of the multi-channel configuration is introduced.

The experimental part starts from presenting the setups used in the work. Then, the noise measurements are analyzed to validate the model developed for noise characterization. Finally, the proposed methodology is tested on three shapes.

5.1 THEORETICAL FRAMEWORK

The method known as SCA, which has always been considered in the context of single channel sensors, is going to be extended onto multicore fibers for shape sensing. Recalling Eq. 4.2, there is an ambiguity in detecting the spectral shift of the Rayleigh trace, as it can be caused by both strain and temperature. In this chapter, we assume that the thermal impact is negligible, and SCA detects only strain. During the experiments, the laboratory conditions are set in such a way that thermal fluctuations of the environment are minimized.

It should be noted that the previously discussed multiplexing technique would not be as practical as the extended SCA in the current case, which is an application in shape sensing. When interrogating a simple SMF, the sensing region is determined by the characteristics of the utilized OFDR setup. However, when the method of multiplexing the fibers with enhanced Rayleigh backscattering is used, the same sensing region also needs to accommodate the delay lines and the fibers concatenated into a single link, which means that the actual length covered by the sensor is significantly reduced, as indicated by Eq. 4.4. Although this method can be applied in shape sensing, the demonstrated implementations were targeted towards medical applications. In medical area, shorter lengths are usually interrogated,

such as the case with the monitoring of needle deformations during the insertions.

When working with shape sensing, the length covered by a fiber link is a crucial factor. Hence, it is necessary to fully utilize the sensing capabilities of the OFDR, which is why SCA is considered. The goal is to make the sensing range cover L_f instead of NL_f.

The most efficient way to interrogate the multiplexed channels simultaneously is to use a separate detector for each of them, which is a costly solution that requires complex hardware. Moreover, as it is based on measurements of forward propagation, it would be intrinsically incompatible with the considered OFDR paradigm. In OFDR, the output is monitored at the same point where the probe is launched. After the backscattering signals pass through the coupling point, they cannot be split again in accordance with the multiplexed arrangement of channels and preserve the same spatial relationship. Thus, only a single point can be used to collect the backscattering signals. Instead, most of the existing shape sensing techniques are based on the interrogation schemes where light does not pass through the multiplexed channels at the same time, but sequentially, which allows to use a single detector. It was the case in the previously discussed configuration. A common technique to implement sequential interrogation is to alternate between the channels with an optical switch, obtaining the respective backscattering signals in a quick succession. However, due to the delays between receiving the backscattering traces of different channels, it may be difficult to accurately capture dynamic variations of strain. Moreover, the effective acquisition rate is reduced, since the amount of scans is equal to the number of multiplexed channels.

In the proposed method, only one probe needs to be done to collect the backscattering of the stressed fiber.

5.1.1 *Sequential interrogation*

In order to conduct shape sensing, a fiber link consisting of at least 3 channels is needed. It can be either a multi-core fiber or a multiplexed set of independent fibers; from this point on, multi-core fibers are going to be considered. Still, the discussed approaches are valid for other multi-channel configurations as well. For convenience, multi-core fibers may be preferable, since the equal angular spacing of the cores and the constant radius from the center to the cores are ensured by manufacturers; otherwise, it could be cumbersome to achieve the same specifications in a custom setup consisting of independent fibers. Multiplexing of the cores into a single link can be accomplished with simple couplers. When multiplexed cores are connected directly to the OFDR, the backscatterings from different cores are mixed at the point of multiplexing. Hence, the superposed backscattering is monitored at the output of the OFDR setup. On the other hand, an optical switch allows to select one core at a time, which means that only one scattering signal travels back along the propaga-

tion route. The introduction of the switch does not affect the overall configuration, since its insertion loss and the cross-talk are typically very low.

It is supposed that the distances from the center of the fiber to each core are the same. The cores are also offset from each other by the same angle.

First, according to the conventional sequential interrogation approach, the separate signatures are collected for each core by alternating between them with the switch. At this stage, when the fiber experiences no perturbation, the time between switching is not crucial. When the fiber is stressed, the switch is utilized again to cyclically interrogate each core. This time, however, a quick switching is needed; otherwise, the fiber state represented by the backscattering in each core may not be the same, depending on how dynamic the nature of the perturbation is.

And yet, under the stable testing conditions with the fixed strain, the sequential method provides accurate measurements and can serve as a reliable benchmark.

5.1.2 *Parallel transport frame method*

In the work, only flat curves are going to be considered. In 3-dimensional recreation of shape, the internal twist of the fiber significantly complicates the detection. However, the focus of the current work is solely on the comparison of shape sensing performance. Even if the twist can be measured, the development of a mathematical algorithm that could decouple the twist from the shape does not fit within the scope of this chapter.

It is possible to detect the shape variations along a fiber link that consists of at least three propagation channels, or cores. Higher number of cores can enable higher spatial resolution. The spatial orientation of each point on the fiber can be represented with the curvature and the bending angle, which are the parameters obtained by considering the strain values across all the cores. With these parameters, the reconstruction algorithms are able to estimate the geometrical shape of the fiber in space. For example, Frenet-Serret formulas can be used for reconstruction in 3D-space [87]. However, the correct 3D-recreation can only be done by compensating for the internal twist of the fiber. It is a complex issue which is beyond the scope of the work, since the current goal is to compare the proposed shape sensing method with the sequential approach.

To avoid problems due to the twist, it is better to consider flat curves. For this reason, parallel transport frame is a shape reconstruction method used in this work, as it is more suitable for shape sensing in 2D-space [88]. Moreover, this method requires less differentiation steps, which means that the accumulation of the computational errors is at the lower rate.

The fiber shape is governed by the following vector in X-Y coordinates:

$$\mathbf{p}(z) = x(z)\mathbf{i} + y(z)\mathbf{j}. \tag{5.1}$$

Generally, the distance between two consecutive points on a curve is known as the arc length. In our case, it is determined by the gauge length of SCA.

At each position z, the unit vector tangent to the curve in Eq. 5.1 is defined as

$$\mathbf{T}(z) = \frac{x'(z)\mathbf{i} + y'(z)\mathbf{j}}{\sqrt{(x'(z))^2 + (y'(z))^2}}. \tag{5.2}$$

The local curvature vector is equal to $\kappa(z) = \mathbf{T}'(z)$. The length of this vector, $\kappa(z)$, defines the rate at which the tangent vector varies with respect to the arc length. It is commonly referred to as the curvature, and it is also defined as the inverse of the curvature radius.

In the reconstruction process, the vector values of $\mathbf{T}$ is determined by numerically solving the following matrix:

$$\begin{bmatrix} \mathbf{T}' \\ \mathbf{N}_1' \\ \mathbf{N}_2' \end{bmatrix} = \begin{bmatrix} 0 & \kappa_1 & \kappa_2 \\ -\kappa_1 & 0 & 0 \\ -\kappa_2 & 0 & 0 \end{bmatrix} \begin{bmatrix} \mathbf{T} \\ \mathbf{N}_1 \\ \mathbf{N}_2 \end{bmatrix} \tag{5.3}$$

where $\mathbf{N}_1$ and $\mathbf{N}_2$ are normal unit vectors perpendicular to the tangent vector in the normal plane at the current position z, and κ_1 and κ_2 are the magnitudes of the curvature vector projections on $\mathbf{N}_1$ and $\mathbf{N}_2$.

Then, the curve from Eq. 5.1 is estimated:

$$\mathbf{p}(z) = \int \mathbf{T}(z)\, dz + \mathbf{p}_0(z), \tag{5.4}$$

with $\mathbf{p}_0(z)$ defining the position on the fiber where the reconstruction starts.

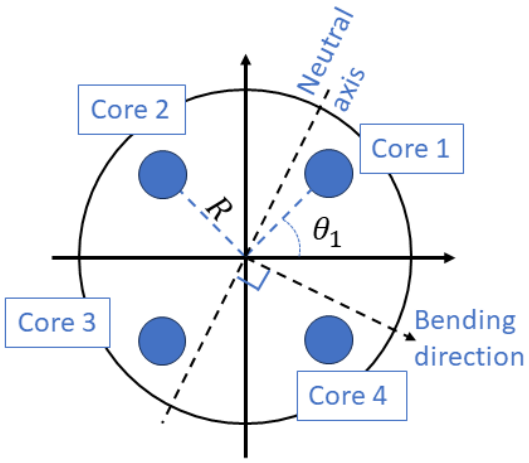

Figure 5.1: Cross-sectional view of the cores subjected to bending.

Fig. 5.1 is the cross-sectional view of the fiber, showing the arrangement of the cores. θ_i, referred to as the core angle, and radius R are

known from the fiber specifications. Neutral axis represents the state of zero strain, and the direction of bending is perpendicular to it. After applying the expanded SCA, we have strain ε_i for each core i. Then, the local curvature vector directed from the center of the fiber to the core i is obtained: $\boldsymbol{\kappa_i} = -\frac{\varepsilon_i}{R}(\cos\theta_i \mathbf{j} + \sin\theta_i \mathbf{k})$. By summing the curvature vectors of all the cores, we calculate the overall local curvature vector:

$$\boldsymbol{\kappa} = -\sum_{i=1}^{M} \frac{\varepsilon_i}{R} \cos\theta_i \mathbf{j} - \sum_{i=1}^{M} \frac{\varepsilon_i}{R} \sin\theta_i \mathbf{k} \tag{5.5}$$

The angle of the vector from Eq. 5.5 is the bending direction.

The lengths of the X and Y components of the curvature vector, κ_1 and κ_2, are then substituted into Eq. 5.3.

For initial conditions, the eye matrix can be selected as the matrix in Eq. 5.3. The choice of the initial matrix is a trivial matter, because it is only needed to define the starting orientation of the fiber shape. The shape variations along the fiber stay the same regardless of the initial point. To numerically compute the derivatives, backward differentiation is used.

With longer reconstruction lengths, the integration steps involved in the process lead to the error accumulation.

5.2 METHODOLOGY

5.2.1 *Extension of spectral correlation analysis to multi-core fibers*

In literature, SCA has always been considered in the context of fiber sensors containing just a single propagation channel. However, the technique can be also expanded to perform operations on multi-core fibers.

In the expanded implementation, the starting point is the same. For each channel, the Rayleigh signature is obtained. It can be achieved, for example, by using the sequential approach. It should be emphasized that these signatures need to be collected only once; after that, the switch can be removed from the setup. From this point on, the mixed backscattering due to the superposition of the signals from all the cores is considered.

Let us suppose there is a fiber link consisting of M cores. The individual backscattering signals, $s_i(z)$, arrive at the receiver all at once, and the single superposed backscattering can be expressed as $s_{mix}(z) = \sum_i s_i(z)$, with i indicating the index of a core. In theory, the strain of along each core can be extracted by using the stored signature traces in the SCA procedure: $SCA[s_{i,ref}(z), s_{mix}(z)] = \varepsilon_i(z)$. A shift of one of the traces may be needed to align the ends of the fiber links. The cross-correlation of the separate signature and the mixed trace results in a sum of M terms. One of them provides meaningful information exclusive to the core i due to the spatial alignment, and the remaining terms represent the noise uncorrelated with the signature of the core i.

The main advantage over the sequential method, as well as the method discussed in the previous chapter, is that now the cores can be probed simultaneously, instead of cycling through each core either with the switch or by sending the probe across the channels cascaded into one propagation route. In the latter case, one probe is actually split between the number of channels. Thus, the expanded SCA enables the most efficient acquisition rate, and also allows to multiplex longer channels.

An important consideration is that the higher the number of cores being considered at once, the higher the amount of noise present in the mixed backscattering. In order to successfully extract the individual strains, the overall noise has to be lower than a certain threshold. We propose to characterize this threshold with Cramer-Rao lower bound (CRLB), which is usually considered in the context of sonar communications.

5.2.2 *Cramer-Rao lower bound*

Firstly, let us briefly review CRLB in its original context, which is the reception of signals in sonar systems. Let us assume that we receive a signal with two detectors. One of them experiences a delay in the reception and an attenuation in amplitude due to the propagation medium. The noise patterns of the signals are uncorrelated. The variance of the delay between the signals can be expressed as follows:

$$\sigma_D^2 = \frac{3}{8B^3T\pi^2}\frac{1+2SNR}{SNR^2}, \tag{5.6}$$

where $C(t)$ is the normalized cross-spectral density function of the two received signals, T is the length of time window used to segment the signals, and B is the bandwidth of the signals.

As evident, a certain SNR needs to be maintained to avoid high estimation errors. The detailed derivation of Eq. 5.6 can be found in Ref. [89]. Instead, this work will present the proof for the case of CRLB in OFDR with interrogation of multiple cores. Cores in fiber sensing can be thought of as analogous to receivers in sonar communications.

The concept of CRLB in OFDR is in itself a novel consideration. The variance of the delay has to be obtained for frequency domain instead of time domain. Firstly, let us consider the case when a single core is interrogated ($N = 1$). $b_0(\omega)$ is the reference backscattering, and $b_1(\omega)$ is the backscattering of the fiber which undergoes a frequency shift Ω due to the applied stress. They can be expressed as follows:

$$b_0(\omega) = s(\omega) + \eta_0(\omega), \tag{5.7}$$

$$b_1(\omega) = s(\omega - \Omega) + \eta_1(\omega), \tag{5.8}$$

where $s(\omega)$ is the source backscattering, η_0 and η_1 are uncorrelated noise signals. The goal is to obtain an estimate of Ω.

Since we consider the case when no perturbations act on the straight fiber, signals $b_i(\omega)$ and $\eta_i(\omega)$ are assumed to be Gaussian. The Gaussian coefficients of b_i are

$$B_i(k) = \frac{1}{B}\int_0^B b_i(\omega)e^{jk\omega t}\,d\omega. \tag{5.9}$$

Then, the Fourier transform of $b_i(\omega)$ into time domain is equal to

$$\tilde{B}_i(t) = \lim_{B\to\infty} B\,B_i(k) = \int_0^\infty x_i(\omega)e^{jt\omega t}\,d\omega. \tag{5.10}$$

Generally, the signature and the FUT traces can be represented in vector form:

$$\mathbf{B}(\mathbf{k}) = [B_0(k)\,B_1(k)]'. \tag{5.11}$$

The power spectral density matrix of the signals can be written as

$$Q = E[\mathbf{B}(\mathbf{k})\mathbf{B}^{*\prime}(\mathbf{k})] = E\begin{bmatrix} B_0(k)B_0^*(k) & B_0(k)B_1^*(k) \\ B_1(k)B_0^*(k) & B_1(k)B_1^*(k)\end{bmatrix}. \tag{5.12}$$

The matrix in Eq. 5.12 can be further expressed in terms of $G_{b_ib_j}$, which is the Fourier transform of cross-correlations between signals $b_0(\omega)$ and $b_1(\omega)$:

$$Q = \frac{1}{B}\begin{bmatrix} G_{b_0b_0}(t) & G_{b_0b_1}(t) \\ G_{b_1b_0}(t) & G_{b_1b_1}(t)\end{bmatrix} = \frac{1}{B}Q_x. \tag{5.13}$$

The probability density function of B_i given the matrix Q is

$$p(X|Q) = c\,exp(-\frac{1}{2}J_1), \tag{5.14}$$

where J_1 is equal to

$$J_1 = \sum_{k=-N}^{N} \mathbf{B}^{*\prime}Q_x^{-1}\mathbf{B}(k)B. \tag{5.15}$$

Using the relationship from Eq. 5.10, Eq. 5.15 becomes

$$J_1 = \frac{1}{B}\sum_{k=-N}^{N} \tilde{\mathbf{B}}^{*\prime}(t)Q_x^{-1}\tilde{\mathbf{B}}(t), \tag{5.16}$$

and for large values of B, Eq. 5.16 becomes

$$J_1 = \int_0^\infty \tilde{\mathbf{B}}^{*\prime}(t)Q_x^{-1}\tilde{\mathbf{B}}(t)dt. \tag{5.17}$$

Let us denote the normalized cross-spectral density function of the measured signals by $C(t)$:

$$C(t) = \frac{G_{b_0b_1}(t)^2}{G_{b_0b_0(t)}G_{b_0b_1}(t)}. \tag{5.18}$$

Then, after factorization, we write Q_x^{-1} as

$$Q_x^{-1} = \frac{1}{1-C(t)} \begin{bmatrix} \frac{1}{G_{b_0b_0}(t)} & \frac{-G_{b_0b_1}(t)}{G_{b_0b_0}(t)G_{b_1b_1}(t)} \\ \frac{-G^*_{b_0b_0}(t)}{G_{b_0b_0}(t)G_{b_1b_1}(t)} & \frac{1}{G_{b_1b_1}(t)} \end{bmatrix}. \tag{5.19}$$

After substituting Eq. 5.19 in Eq. 5.17, we obtain

$$J_1 = \int_0^\infty \frac{1}{1-C(t)} \left[\frac{|\tilde{B}_0(t)|^2}{G_{b_0b_0}(t)} + \frac{|\tilde{B}_1(t)|^2}{G_{b_1b_1}(t)} \right] dt - J_3, \tag{5.20}$$

where J_3 is

$$J_3 = \int_0^\infty \frac{1}{1-C(t)} \left[\frac{\tilde{B}^*_0(t)G_{b_0b_1}(t)\tilde{B}_1(t)}{G_{b_0b_0}(t)G_{b_1b_1}(t)} + \frac{\tilde{B}^*_1(t)G^*_{b_0b_1}(t)\tilde{B}_0(t)}{G_{b_0b_0}(t)G_{b_1b_1}(t)} \right] dt. \tag{5.21}$$

Two terms inside the integral in Eq. 5.21 are conjugates:

$$J_3 = \int_0^\infty \frac{1}{1-C(t)} \left[A^*(t) + A(t) \right] dt, \tag{5.22}$$

with

$$A = \frac{\tilde{B}^*_1(t)G^*_{b_0b_1}(t)\tilde{B}_0(t)}{G_{b_0b_0}(t)G_{b_1b_1}(t)}. \tag{5.23}$$

Each transformed cross-correlation can be further expressed in terms of cross-correlations between source and noise signals using Eq. 5.7:

$$G_{b_ib_j} = G_{ss}e^{j2\pi\Omega t} + G_{\eta_i\eta_j}. \tag{5.24}$$

There is no term for correlation between the source signal and the noise, because it always results in zero. Correlating different Gaussian noises also gives zero. From 5.24, it follows that

$$|G_{b_1b_2}| = G_{ss}, \tag{5.25}$$

which leads to Eq. 5.23 transforming into

$$A = \frac{\tilde{B}^*_1(t)|G_{b_0b_1}|e^{-j2\pi\Omega t}\tilde{B}_0(t)}{G_{b_0b_0}(t)G_{b_1b_1}(t)} = \frac{\tilde{B}^*_1(t)\tilde{B}_0(t)C(t)}{|G_{b_0b_1}|}e^{-j2\pi\Omega t}. \tag{5.26}$$

If the analyzed signals are real, then $A^*(t) = A(-t)$, and $\tilde{B}^*_1(t)\tilde{B}_0(t)$ can be used to obtain the estimation of the transformed cross-correlation: $\tilde{B}^*_1(t)\tilde{B}_0(t) = B\hat{G}_{b_0b_1(t)}$. As a result,

$$J_3 = 2B \int_0^\infty \frac{\hat{G}_{b_0b_1(t)}}{|G_{b_0b_1}|} \frac{C(t)}{1-C(t} e^{-j2\pi\Omega t} dt, \tag{5.27}$$

and only J_3 in Eq. 5.20 is dependent on the frequency shift Ω. Using 5.14, the uncertainty on the frequency shift is evaluated as follows:

$$var(\Omega) \geqslant \frac{-1}{\frac{\delta^2}{\delta\Omega^2}E(-\frac{1}{2}J_3)}. \tag{5.28}$$

In the expression above, only the parts dependent on the delay can be differentiated. Hence, the variance of the frequency shift can be generally expressed as

$$\sigma_\Omega^2 \geqslant 2\pi \left[B \int_0^{T_w} \frac{C(t)}{1-C(t)}\, t^2\, dt \right]^{-1}, \tag{5.29}$$

where B is the bandwidth swept by the OFDR.

Thus, using Eq. 5.24, Eq. 5.18 becomes

$$C(t) = \frac{(G_{ss} + G_{\eta_0\eta_1})^2}{(G_{ss} + G_{\eta_0\eta_0})(G_{ss} + G_{\eta_1\eta_1})} = \frac{G_{ss}^2}{(G_{ss} + G_{\eta\eta})^2}, \tag{5.30}$$

With $SNR = \frac{G_{ss}^2}{G_{\eta\eta}^2}$,

$$\frac{C(t)}{1-C(t)} = \frac{SNR^2}{2SNR+1}, \tag{5.31}$$

and the lower bound in Eq. 5.29 is

$$2\pi \left[B \int_0^{T_w} \frac{SNR^2}{2SNR+1}\, t^2\, dt \right]^{-1} = 2\pi \left[\frac{1}{3} B T_w^3 \frac{SNR^2}{2SNR+1} \right]^{-1}. \tag{5.32}$$

Thus, Eq. 5.29 for the number of cores $N = 1$ is

$$\sigma_\Omega^2 \geqslant \frac{6\pi}{BT_w^3} \left(\frac{2 \cdot SNR + 1}{SNR^2} \right), \tag{5.33}$$

which is consistent with the expression for time delay estimation from Eq. 5.6, except for the duality between frequency and time domain.

Then, it is required to obtain the CRLB expression when the amount of interrogated cores is higher than 1. In this case, the analyzed backscatterings from Eq. 5.7 become:

$$b_0(\omega) = s(\omega) + \eta_0(\omega), \tag{5.34}$$

$$b_1(\omega) = \frac{1}{N} s(\omega - \Omega) + \eta_1(\omega) + \frac{1}{N} \sum_{k=1}^{N-1} s_k(\omega), \tag{5.35}$$

The reference is the same as for $N = 1$. The perturbed signal is different; the respective source signal is attenuated by the factor of N, since the overall backscattering is distributed between N cores. The noise signal also contains attenuated ideal signals of the rest of the cores, since they are not correlated with $s_1(\omega)$. Thus, after combining Eqs. 5.18, 5.24 and 5.34 for N number of cores, the resulting expression of the normalized cross-spectral density function is

$$C(t) = \frac{\frac{1}{N^2} G_{ss}}{(G_{ss} + G_{\eta_0\eta_0})(\frac{1}{N^2} G_{ss} + G_{\eta_1\eta_1} + \frac{(N-1)^2}{N^2} G_{ss})}. \tag{5.36}$$

In this case, the expression in Eq. 5.31 simplifies to

$$\frac{C(t)}{1-C(t)} = \left[N - 1 + \frac{N^2}{SNR^2} + \frac{N(N+1)}{SNR} \right]^{-1}, \tag{5.37}$$

and the CRLB in Eq. 5.29 can be expressed as

$$\sigma_\Omega^2 \geqslant \frac{6\pi}{BT_w^3}\left[(N-1)+\frac{N(N+1)}{SNR}+\frac{N^2}{SNR^2}\right]. \tag{5.38}$$

We can see that the variance increases with the number of simultaneously interrogated cores. Multiplexing is achieved at the expense of an increase in noise. Clearly, Eq. 5.38 is the extension of the single core interrogation case, as $N = 1$ reduces it to the expression in Eq. 5.33.

The SNR used in the model equations is the one obtained from the OBR measurements done with the sequential interrogation ($N = 1$). It is obtained by averaging the SNRs obtained from the raw backscattering trace of all the cores. Fig. 5.2 shows theoretical bounds depending on the SNR of the measurements.

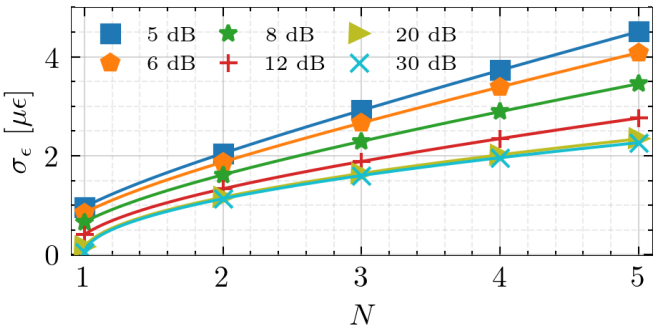

Figure 5.2: CRLB of strain standard deviation, calculated using Eq. 5.38, as a function of the number of cores interrogated simultaneously.

However, the model is described under the assumption that each core has the same SNR value. In practice, there are bound to be some deviations from the assumed conditions due to the inherent non-idealities of the used devices and components. Hence, we need to introduce a parameter that can compensate for these divergences. Unequal SNR values across cores means that the signal power is not distributed equally. We can assume that this power differs from the default core, numbered as core 1, by some factor α_i, and Eq. 5.35 becomes:

$$b_1(\omega) = \frac{1}{N}s(\omega-\Omega)+\eta_1(\omega)+\frac{1}{N}\sum_{k=1}^{N-1}\alpha_k s_k(\omega), \tag{5.39}$$

and the SNR across each core is $SNR_i = \alpha_i SNR_1$.

Ideally, when the expression in Eq. 5.39 is equal to Eq. 5.35, it yields:

$$\sum_{k=1}^{N-1}\alpha_k = A\,(N-1), \tag{5.40}$$

with $A = 1$. However, in case of unequal SNRs, A is different for each core, as it is defined by the averaged sum of coefficients α_k in the rest of the cores. Hence, the corrected CRLB becomes

$$\sigma_\Omega^2 \geqslant \frac{6\pi}{BT_w^3}\left[(N-A^2)+\frac{N(N+1)+1-A^2}{SNR}+\frac{N^2}{SNR^2}\right]. \tag{5.41}$$

Before starting the measurements of shape, the SNR is going to be obtained from the backscattering trace of each core. Then, the differences in the SNR are used to determine α_i, which allows to obtain A for all of the cores. These values are averaged and substituted into Eq. 5.41 to obtained the compensated bound, which is supposed to follow one of the curves in Fig. 5.2, depending on the SNR of the real backscattering.

5.3 EXPERIMENTAL SETUPS

5.3.1 *Conventional setup with an optical switch*

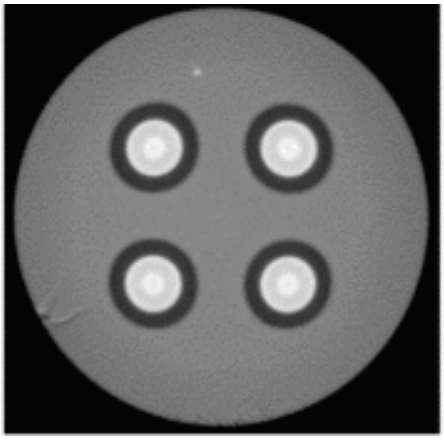

Figure 5.3: Cross-sectional view of the U4CF.

Throughout the described experiments, an uncoupled-4-core-fiber (U4CF) is used as the FUT [90] (the fiber provided by Optical Communications Laboratory, Sumitomo Electric Industries); each core is denoted with an index i. The radius, i.e., the distance between the center and each core, is 40 µm. The schematic arrangement of cores is shown in Fig. 5.3.

The benchmark setup, based on the sequential interrogation, is shown in Fig. 5.4. The FUT is connected to a multiplexer. The SMF links of the multiplexer corresponding to different cores are coupled to the ports of an optical switch. The switch itself is connected to the OFDR device (OBR 4600, Luna Innovations).

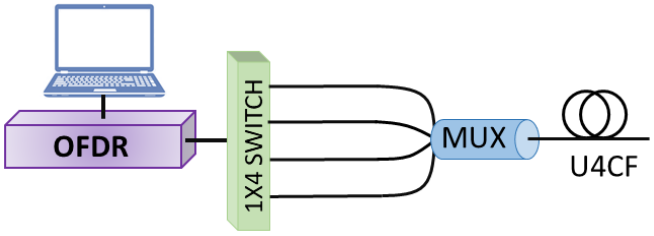

Figure 5.4: Experimental setup for sequential interrogation of the cores using an optical switch.

5.3.2 *Setup for simultaneous interrogation of fiber cores*

In the setup built for testing the expanded SCA, as shown in Fig. 5.5, the FUT is also connected to the same multiplexer. The outputs of the multiplexer are grouped into two pairs; each of them is recombined with a 50/50 couplers; they are also recombined by the same type of coupler. Finally, this cascaded configuration is connected to the OFDR device.

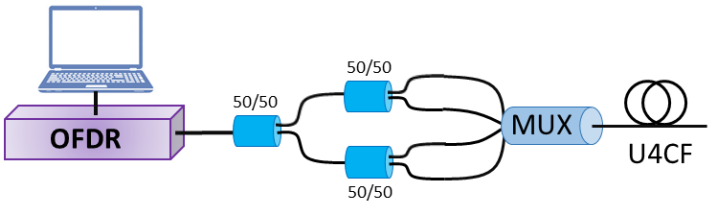

Figure 5.5: Proposed setup for simultaneous interrogation of the cores.

In addition, another setup, shown in Fig. 5.6, was built by altering the scheme in Fig. 5.5. It interrogates only two cores of the fiber, and it was built solely for the purpose of the noise characterization.

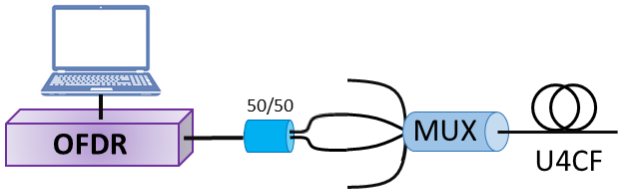

Figure 5.6: Setup for simultaneous interrogation of 2 cores.

As for SCA, the gauge length of 1.5 cm is used.

5.4 RESULTS

5.4.1 *Noise characterization*

Firstly, the measurements were done on a straight, unperturbed fiber. In this state, the strain variation is supposed to be zero, so any deviation is actually due to noise. An example of the measured noise is shown in Fig. 5.7. As expected, it is evident that lower number of cores leads to lesser noise. The goal of this part is to quantify and parameterize this difference.

The overall purpose of this stage is to verify the CRLB model by showing how the noise varies depending on the number of cores being interrogated simultaneously. Specifically, the tested number of interrogated cores N was set to 1, 2, and 4.

The reference signatures of all the cores were collected with the sequential interrogation scheme from Fig. 5.4. For $N = 1$, the same scheme was used. In this case, the strain values along each core were obtained using the standard SCA. For $N = 2$, the scheme from Fig. 5.6 was used. Unlike the previous case, the mixed backscattering was

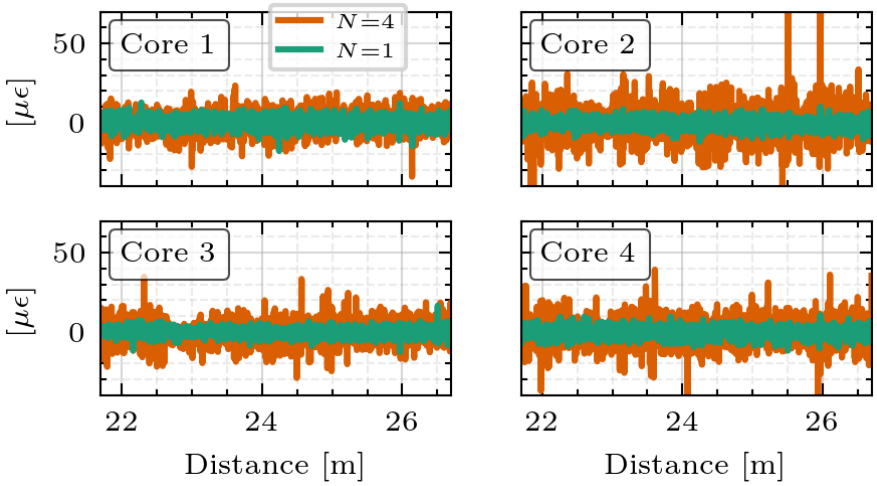

Figure 5.7: Strains measured with the unperturbed straight fiber.

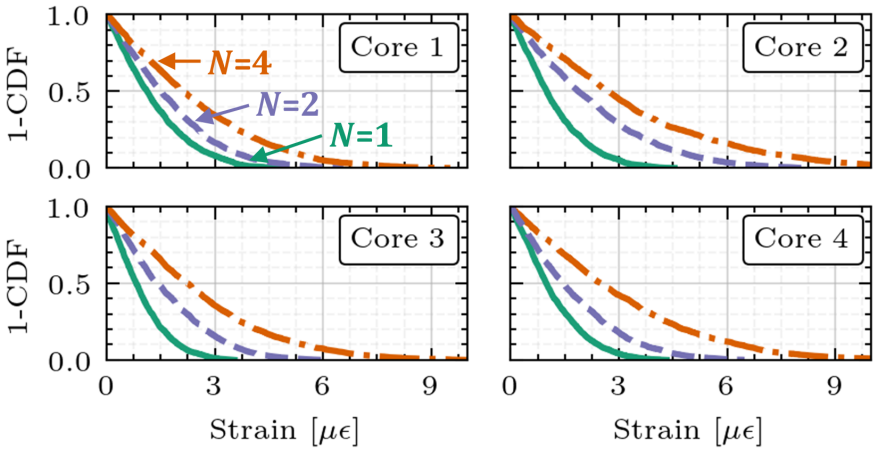

Figure 5.8: Noise floor of the strain measured on the straight fiber. The curves show the probability of the strain being higher than a certain threshold when interrogating N cores simultaneously.

collected. The interrogation was conducted for two setup variations, with the first one coupling Cores 1 and 2, and the second one coupling Cores 3 and 4. It was done in order to have the strain values for each core, so that they could be compared with the cases $N = 1$ and $N = 4$. For $N = 4$, the proposed setup from Fig. 5.5 was used to collect the superposed scattering. For each N, the cumulative distribution function (CDF) was calculated. Fig. 5.8 shows the survival function, equal to $1 - \text{CDF}$, which indicates the probability of the measured strain being higher than a certain value. As seen in the plots, the noise increases with the number of cores.

Then, for each setup, the standard deviations of the strains in all of the cores were estimated and averaged. The resulting values are plotted in Fig. 5.9 with respect to the number of cores interrogated by the setups. In addition, the SNR of each core was obtained from the OBR traces collected with the benchmark setup ($N = 1$), since, according to the CRLB model, this configuration provides the default SNR values for Eq. 5.38. The determined SNR values were equal to 14.3, 8.7, 11.6,

and 10.4 dB for Cores 1, 2, 3, and 4, respectively. By considering Core 1 to be the default core, the values of α_i were obtained with Eq. 5.39 ($\alpha_1^2 = 1$, $\alpha_2^2 = 0.28$, $\alpha_3^2 = 0.54$, $\alpha_4^2 = 0.41$). From there, the correction factor A can be determined with Eq. 5.40 for each configuration of cores. The average of these values was used in Eq. 5.38 to calculate the corrected CRLB bound, which is also plotted in Fig. 5.9. As it can be seen, the results follow a trend which is similar to the theoretical bound. The values of the measured standard deviations are higher than those of the CRLB, which is in accordance with the conditions of Eq. 5.38. Moreover, the implemented correction allowed to narrow the gap between the theory and the measurements.

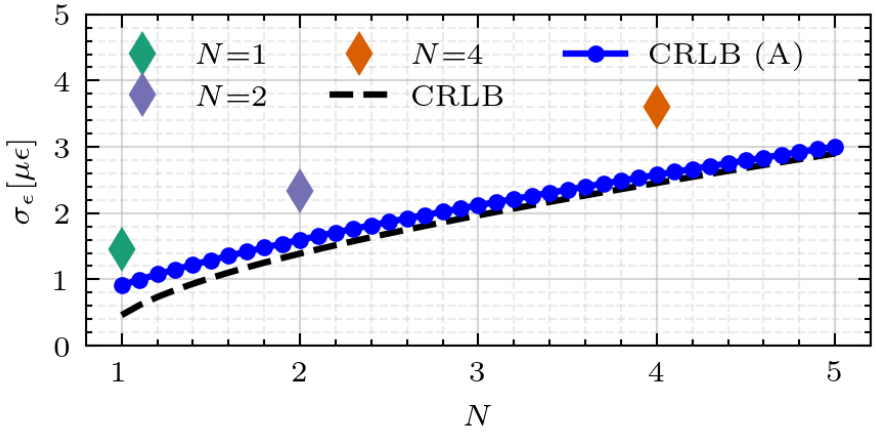

Figure 5.9: Experimental validation of the CRLB.

5.4.2 *Detected shapes*

Throughout the experiments, the fiber was wound along three different shapes. The first one is a single circle of radius equal to 16 cm, the second one is a cascade of two circles of radii equal to 12.25 cm and 8.8 cm, respectively, and the third shape is an Archimedean spiral of outer radius equal to 13.4 cm with a distance between turns equal to

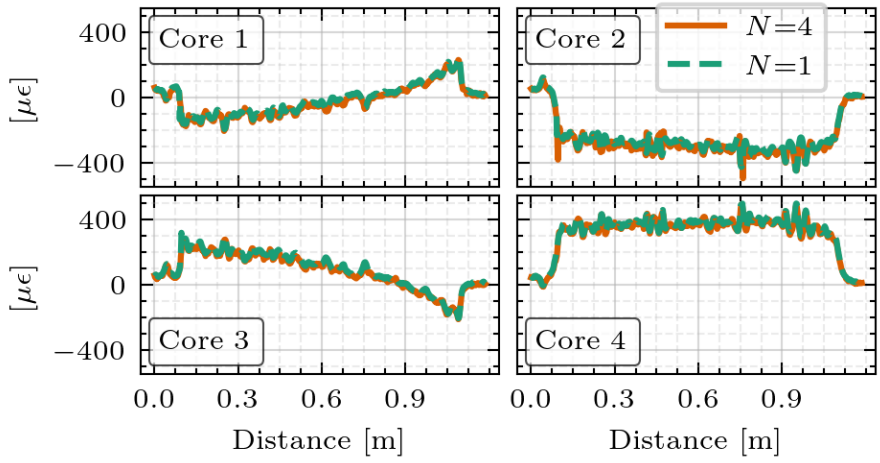

Figure 5.10: Strains measured with the fiber wrapped along single circle.

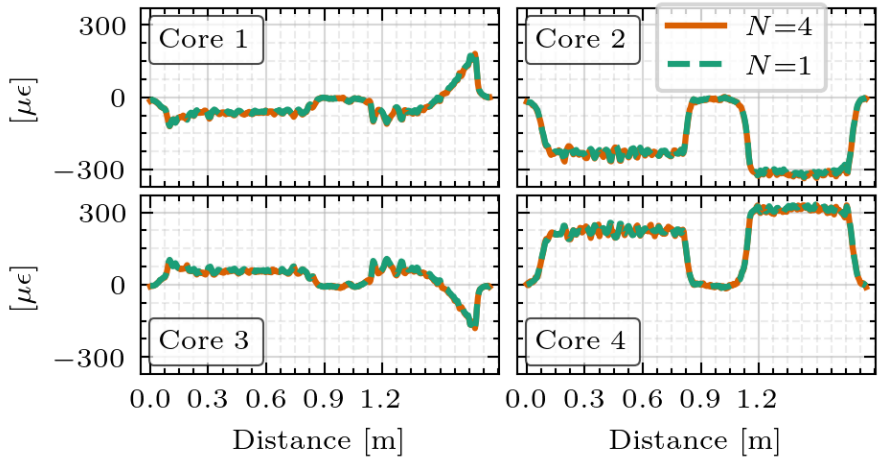

Figure 5.11: Strains measured with the fiber wrapped along two circles.

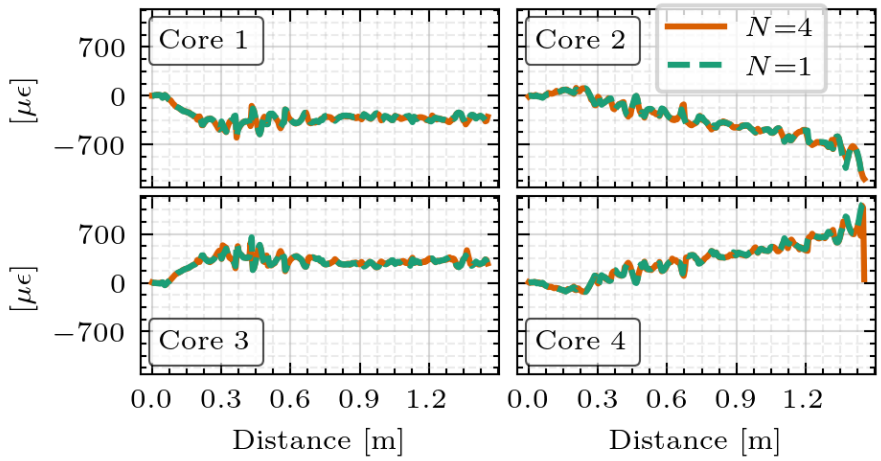

Figure 5.12: Strains measured with the fiber wrapped along spiral.

5 cm. The corresponding strain values obtained along each core with both shape sensing methods are shown in Figs. 5.10-5.12. As it can be seen, Cores 1 and 3 and Cores 2 and 4 detect strains that have opposite trends, which indicates that these the cores in these pairs are 180° apart. Upon visual inspection, the sequential and the simultaneous interrogation techniques achieve a very high degree of similarity. To quantify it, the RMSE values between the strains obtained with the methods are calculated for each shape, and then averaged across the cores.

Then, the strains in Figs. 5.10-5.12 were processed with parallel transport frame. The resulting shape outputs are shown in Figs. 5.13(a-c). The experimentally measured radii are equal to the nominal values. For each of the measured shapes, the geometric fits were generated. During the process of curve fitting, the known values of the radii and the distance between the turns of the spiral were used as fixed parameters. The Frechet distance was used as a metric of the difference between the measured shapes and their fits. For each method, the mean Frechet distance across the three shapes was calculated. The re-

sulting values are equal to 2.8 and 2.6 mm for the benchmark and the proposed method, respectively.

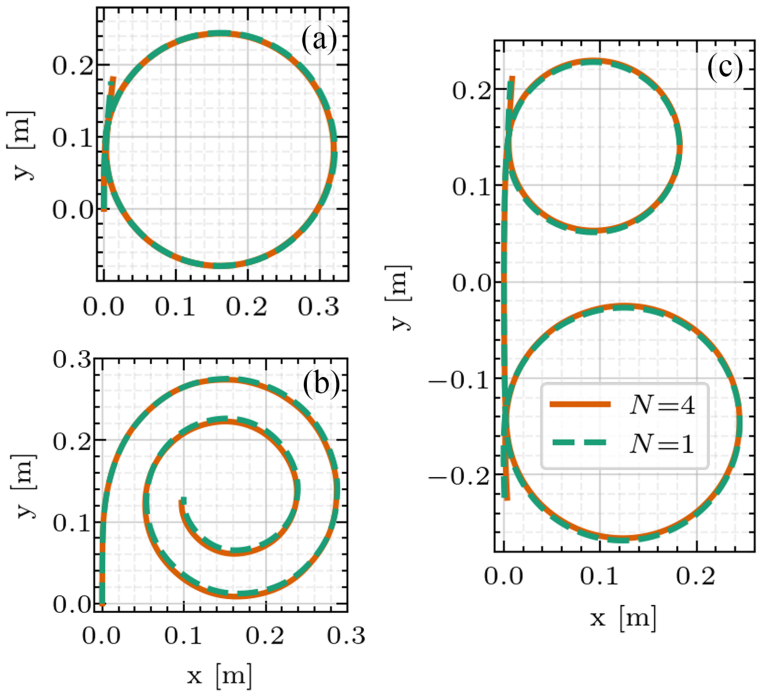

Figure 5.13: Reconstruction of: (a) one circle; (b) spiral; (c) two circles.

The benchmark method does not interrogate the cores simultaneously, which is why its average error was slightly higher, as the temporal relationship between each core is not as strong as when one probe interrogates the cores.

Both methods are accurate with respect to the absolute shapes. Still, there are some deviations between the detected shapes themselves, as becomes evident if they are plotted together. These differences can be attributed to the errors accumulated during the integration steps of parallel transport frame. Both reconstruction processes are independent from each other, so small variations in the strains can lead to variations between the directions of the shape curves.

One of the most important consideration is that while the sequential interrogation used as the benchmark required to do four scans of the multi-core fiber, the proposed approach scanned the fiber only once.

5.5 CONCLUSION

In this chapter, a novel shape sensing technique was introduced. The conventional SCA method was extended to multi-core fibers, which allowed to improve the acquisition rate by a factor equal to the number of simultaneously interrogated cores, compared to methods that interrogate the cores sequentially using a switch. This improvement is particularly important, as it enables potential reconstruction of dynamically varying shapes. The new method also allows to use the

full sensing range for an interrogation of the whole length of each multiplexed core. Moreover, a model for characterizing the noise of the sensing configuration with the respect to the number of cores was presented. It was shown that as long as the proposed method adhered to a specific noise threshold, it was able to provide the shape reconstruction quality on a level comparable with traditional approaches, but at an improved acquisition rate.

Part III

POLARIZATION-RESOLVED SENSING

This part elaborates on the benefits of unspun multi-core fibers in the context of polarization-sensitive configurations.

6 TWIST MEASUREMENTS

In this chapter, polarization-resolved distributed sensing is considered. It is a very useful concept, as it enables the estimation of the internal twist of the fiber. The chapter opens with some mathematical background behind the polarization-assisted twist estimation. The first half describes how the twist affects the light propagation, and the second half explains how the twist can be determined with the polarization-sensitive interrogation. Then, it is discussed how this technique can benefit from using unspun MCFs. The section is followed by the experimental setups used for twist monitoring. In the presentation of the results, it is verified that these measurements can be conducted even at the distances far from the launching end of the fiber. Moreover, it is going to be discovered whether the tested MCF has the same elasto-optic characteristics as the conventional SMF.

6.1 THEORETICAL FRAMEWORK

As the light wave travels in space, its electric field oscillates perpendicularly to the direction of the wave propagation. The oscillations have two signal components that lie in the orthogonal planes. If there is no phase difference between the components, the light is said to be in the state of linear polarization. If this phase difference is equal to $\pi/2$, the light is circularly polarized. In this case, the oscillations rotate circularly around the direction of propagation. Depending on the direction of the rotation, circular polarization can be right-hand or left-hand. For any other value of the phase shift between the components, the light is elliptically polarized. On the other hand, if the oscillations occur in a plane that is randomly oriented with respect to the direction of propagation, the light is unpolarized.

If the light travels through a homogeneous medium, the refractive index along the propagation path remains the same. However, if the medium is inhomogeneous, the refractive indices may change depending on the polarization of the light. These differences between the refractive indices are characterized by a property known as birefringence.

Basically, the light wave propagates through different polarization axes within the same fiber link. The axes can be categorized as slow or fast, depending on the respective speed of propagation. Hence, there is a phase difference between the polarized waveforms. This poses a challenge when developing the fibers for telecommunication purposes, but presents an opportunity for expanding their sensing capabilities.

6.1.1 *Twist phenomenon in fiber*

For completeness, I will briefly review how the twist of the fiber impact the propagation of light.

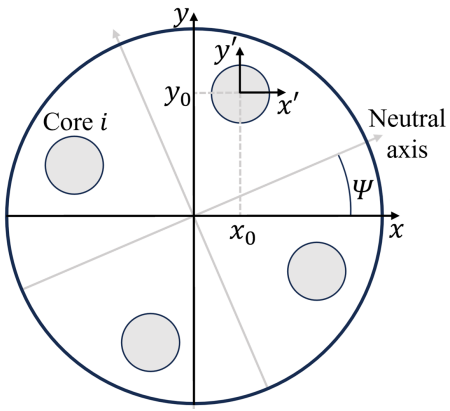

Figure 6.1: Cross-sectional view of the twisted MCF.

Let us suppose that a mode μ propagating through the fiber, shown in cross-section in Fig. 6.1, has a complex amplitude a_μ. The progression of the mode with respect to the spatial point along the fiber can be expressed as

$$\frac{da_\mu}{dz} = -jC_\mu a_\mu(z) - j\sum_\nu K_{\mu,\nu}(z)a_\nu(z), \tag{6.1}$$

with C_μ representing the propagation constant of the mode, and $K_{\mu,\nu}$ being the coupling coefficient related to the perturbation applied to the fiber. $K_{\mu,\nu}$ is equal to

$$K_{\mu,\nu} = \frac{\omega}{4}\iint_S \mathbf{E}^*_\mu(\mathbf{x'}_t)\delta\boldsymbol{\varepsilon}(\mathbf{x'}_t, z)\mathbf{E}_\nu(\mathbf{x'}_t)d\mathbf{x'}_t\,, \tag{6.2}$$

with $\delta\boldsymbol{\varepsilon}(\mathbf{x'}_t, z)$ as the 3×3 matrix that represents the perturbation term that must be added to the dielectric tensor of the ideal fiber core to obtain the perturbed one; the vector $\mathbf{x'}_t = (x' = x - x_0, y' = y - y_0)$ spans the transverse plane of a generic core relative to the position of the fiber axis, and the vectors $\mathbf{E}_\mu$ and $\mathbf{E}_\nu$ are the electric fields of mode μ and ν, respectively. When the fiber experiences twisting by some angle $\psi(z)$, the change in the perturbation matrix becomes

$$\delta\boldsymbol{\varepsilon}(\mathbf{x'}_t, z) = \epsilon_0 n_{av}^2 g\tau(z)\begin{bmatrix} 0 & 0 & -y' \\ 0 & 0 & x' \\ -y' & x' & 0 \end{bmatrix}, \tag{6.3}$$

where n_{av} is the average refractive index, $g \simeq 0.144$ is the elastic-optic rotation coefficient, and $\tau(z) = d\psi/dz$ is the twist rate, which is a parameter of interest in this work.

It is true that external strain can have an effect on the measured twist. However, the bending radii need to be in order of a few cm in order to impact the measurements in a significant way. These measurements can be very useful, for example, robotics [91], as well as

in the monitoring of umbilical cable. By observing when the twist of the cable reaches a critical value, it is possible to avoid the cable breakages.

6.1.2 *Polarization-resolved sensing*

Twist applied to the fiber induces variations in the local birefringence of the fiber. Thus, we first need to estimate the birefringence from the polarization-resolved measurements of the backscattering.

As stated in Chapter 2.2.3, it is possible to obtain polarization-sensitive information from the OFDR measurements. The properties of the received backscattering signal depend on the state of polarization (SOP) of the input light. SOP is a parameter describing how the oscillations of the propagating light wave are oriented. In general, the backscattered SOP along the fiber is described with the Stokes vector $S = [S_0\ S_1\ S_2\ S_3]^T$. The first element, S_0, is the total intensity of the received backscattering, which is the output of the OFDR before it is split into S and P components. The second element, S_1, is obtained by calculating the difference between horizontal and vertical polarization components of the received backscattering. The third element, S_2, is the difference between the light intensities polarized at $+45°$ and $-45°$, respectively. Finally, the fourth element, S_3, is the difference between the intensities that are right-hand and left-hand circularly polarized. If normalized by S_0, S takes the form $[1\ s_1\ s_2\ s_3]^T$. The last three elements serve as a representation of SOP. Thus, SOP can be plotted as a point on the Poincaré sphere.

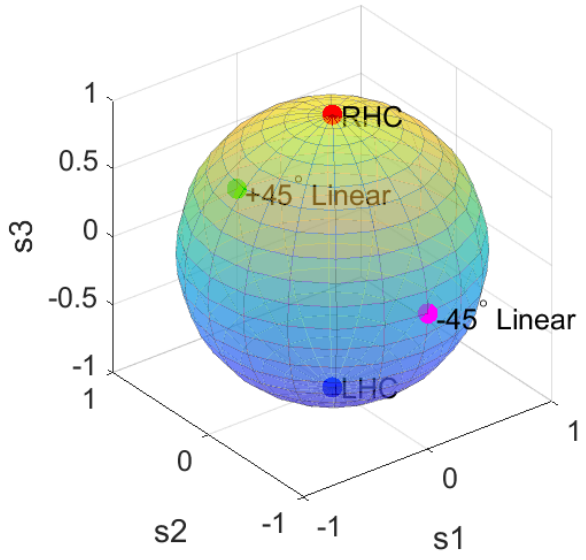

Figure 6.2: Poincaré sphere.

Hence, SOP can be described as a unit vector with 3 components that correspond to the coordinates on the sphere. The points on the equator correspond to the SOPs of the linearly polarized light. The poles correspond to the left-hand and right-hand circular polarization. The origin of the sphere is for the unpolarized light. Due to the

propagation through the fiber, this vector changes, which is reflected by its rotation in the spherical coordinates. This rotation can be represented with the Mueller matrix, **F**, in the following expression:

$$\begin{bmatrix} S_{out,0} \\ S_{out,1} \\ S_{out,2} \\ S_{out,3} \end{bmatrix} = \mathbf{F} \begin{bmatrix} S_{in,0} \\ S_{in,1} \\ S_{in,2} \\ S_{in,3} \end{bmatrix}, \tag{6.4}$$

with $S_{in} = [S_{in,0}\ S_{in,1}\ S_{in,2}\ S_{in,3}]^T$ and $S_{out} = [S_{out,0}\ S_{out,1}\ S_{out,2}\ S_{out,3}]^T$ representing the input SOP and the backscattered SOP, respectively. The backscattered SOP needs to be measured for at least two different input SOPs. Then, we can obtain the solution for the matrix **F** with numerical methods. By comparing the differences between the backscattered SOPs, the birefringence parameters of the analyzed fiber link can be determined. Thus, for the method to be functional, we have to be able to vary the SOP at the input of the employed OFDR setup [92].

Let us suppose that the SOP changes along the fiber at a rate defined as

$$\frac{d\hat{s}}{dz} = \bar{\beta} \times \hat{s}, \tag{6.5}$$

where $\bar{\beta}(z)$ is the birefringence that needs to be measured. With the polarization-resolved measurements of OFDR, the backscattered SOP, $\hat{s}_B(z)$, is obtained. Similarly to Eq. 6.5, its evolution is described as

$$\frac{d\hat{s}_B}{dz} = \bar{\beta}_B \times \hat{s}_B, \tag{6.6}$$

with $\bar{\beta}_B$ standing for the round-trip birefringence:

$$\bar{\beta}_B(z) = 2\mathbf{M}\mathbf{F}^T(z)\bar{\beta}_A(z). \tag{6.7}$$

In Eq. 6.7, $\mathbf{M} = \mathrm{diag}(1, 1, -1)$ is a diagonal matrix, and $\mathbf{F}(z)$ is the Muller matrix which represents propagation from the fiber input up until the position z, and [93]

$$\bar{\beta}_A(z) = \mathbf{U}_3\,[-g\tau(z)]\,\bar{\beta}_L(z), \tag{6.8}$$

where $\mathbf{U}_3$ is a rotation around $\hat{s}_3$ in the Stokes space, and $\bar{\beta}_L(z)$ is the linear part of $\bar{\beta}$. It follows that the linear birefringence can be measured directly from the obtained backscattering, and its rotation leads to circular birefrigence, which is a result of the applied twist.

The evolution of the Muller matrix along the fiber is described as

$$\frac{d\mathbf{F}}{dz} = \frac{1}{2}(\mathbf{M}\bar{\beta}_B) \times \mathbf{F}, \tag{6.9}$$

with $\mathbf{F}(0) = \mathbf{I}$ as the initial conditions.

From Eq. 6.7, the apparent birefringence is obtained as

$$\bar{\beta}_A(z) = \frac{1}{2}\mathbf{F}(\mathbf{z})\mathbf{M}\bar{\beta}_B(z). \tag{6.10}$$

Taking the mathematical procedures from above into consideration, a procedure for calculating the twist can be formulated. First, the backscattering, $\hat{s}_B(z)$, is collected for each SOP. From Eq. 6.6, the round-trip birefringence $\bar{\beta}_B$ is found. Then, the Muller matrix is obtained by numerically solving Eq. 6.9, which enables the computation of the apparent birefringence with Eq. 6.10. Finally, we calculate the twist rate $\tau(z)$ with Eq. 6.8. It is sufficient to launch two SOPs to obtain $\bar{\beta}_B$, but the redundancy actually makes the estimates more reliable.

6.2 UNSPUN MULTI-CORE FIBERS

Due to the primary use of optical fibers in telecommunications, the cores in default versions of SMF are spun to mitigate polarization mode dispersion (PMD). Basically, the fiber is rotated at the drawing stage of manufacturing. The respective spinning rates range from very slow to very fast. At the positions along the fiber where the spinning rates are too high, the backscattered SOP is marked by very quick and faint oscillations. Due to the reduced strength and rapid evolution of birefringence, it becomes very hard to monitor, impeding the development of a reliable polarization-resolved sensor.

On the other hand, there have been significant advances in the development of MCFs over the last years. In particular, uncoupled MCFs strive for the reduction of cross-talk between the cores. As a result, the spinning is avoided during the drawing process, which leads to the corresponding birefringence vector being regular and uninform in their amplitude and orientation. Thus, MCF can have a very high applicability in the field of polarization-resolved fiber sensors.

The current work proposes to verify that MCFs can indeed offer reliable polarization-resolved measurements by measuring the twist applied to the fiber.

6.3 EXPERIMENTAL SETUPS

The same U4CF as in the previous chapter was used to conduct backscattering measurements. The interrogation setups are provided in Fig. 6.3.

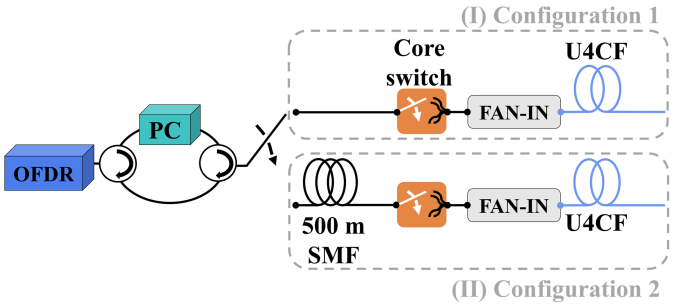

Figure 6.3: Interrogation schemes for polarization-resolved sensing.

The common part of both configurations in Fig. 6.3 includes the OFDR device (OBR 4600, Luna Innovations) connected to a polarization controller (PC). The PC is needed to alter the SOP of the sweeping probe signal. In each sensing session, 4 different SOPs were sequentially launched into the fiber. Both the OFDR and the PC are followed by a circulator.

The difference between the configurations in Fig. 6.3 is that the second one is connected to the ODFR and the PC through 500 m of a SMF. Apart from this, both configurations consist of an optical switch and the U4CF. Essentially, the same sequential interrogation scheme built in the previous chapter was used. Hence, for each SOP, the measurements across all cores of the U4CF could be collected.

For each configuration, the controlled twist was applied to the fiber in a step equal to half of a turn, up to 2 full turns. The twists were applied in both directions. On the tested fiber, a section equal to 3.6 m was selected by fixing its ends. The twisting was performed manually at the 1.74 m position on the selected fiber section.

Unlike the previous chapters, SCA is not used now, the raw backscattering signals obtained as the direct output of OFDR are processed. For the first configuration, the scans were performed with the central wavelength at 1550 nm, and the swept range of 43 nm, resulting in the spatial resolution equal to 4 mm. In the second configuration, due to the considerably higher length being under observation, the swept bandwidth was reduced to 0.8 mm, which permitted the spatial resolution of 6 cm.

6.4 RESULTS

The backscattering signals obtained with the first and the second configurations from Fig. 6.3 were processed in accordance with the procedure from 6.1.1 to obtain the twist rates in Figs. 6.4 and 6.5, respectively.

For each case, the obtained number of turns was in agreement with the applied twist. Moreover, these results were determined by setting the elasto-optic coefficient g in Eq. 6.8 to 0.144, which is also a typical value for SMFs [37]. Hence, the elastic properties of the U4CF were indeed verified.

The measurements in Fig. 6.5 are marked by oscillations stronger than those in Fig. 6.4. It is expected, since the constrains in the spatial resolution result in lower accuracy. Beyond the fixed points of the fiber, any variations are basically contributions by noise. The evaluation of these regions indicated the standard deviation values of 3.6° and 9° for the first and the second configurations, respectively. These values are quite low when compared to the angles of the turns, since each full turn is equal to 360°.

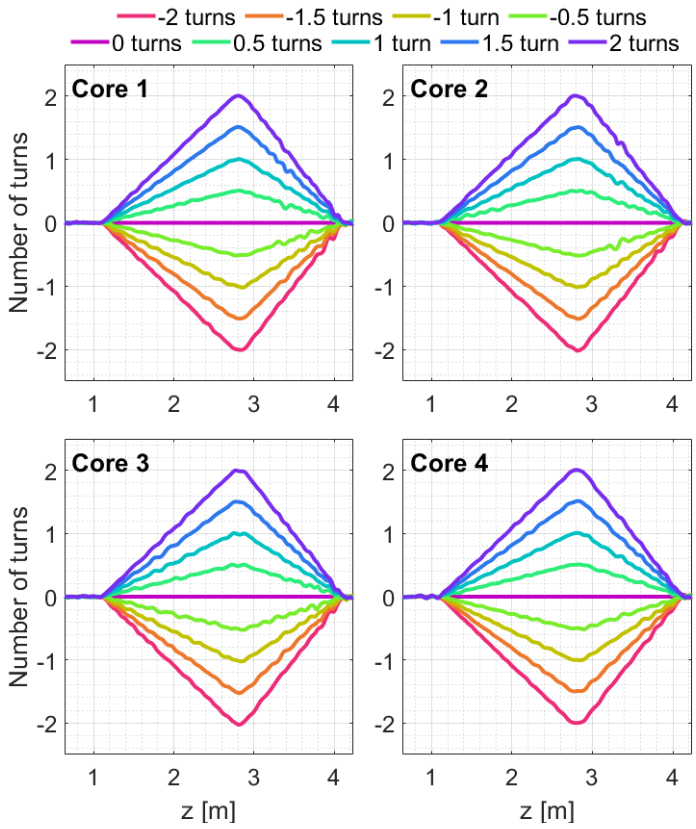

Figure 6.4: Number of turns measured with respect to the reference state when the U4CF is connected to the OFDR without a delay.

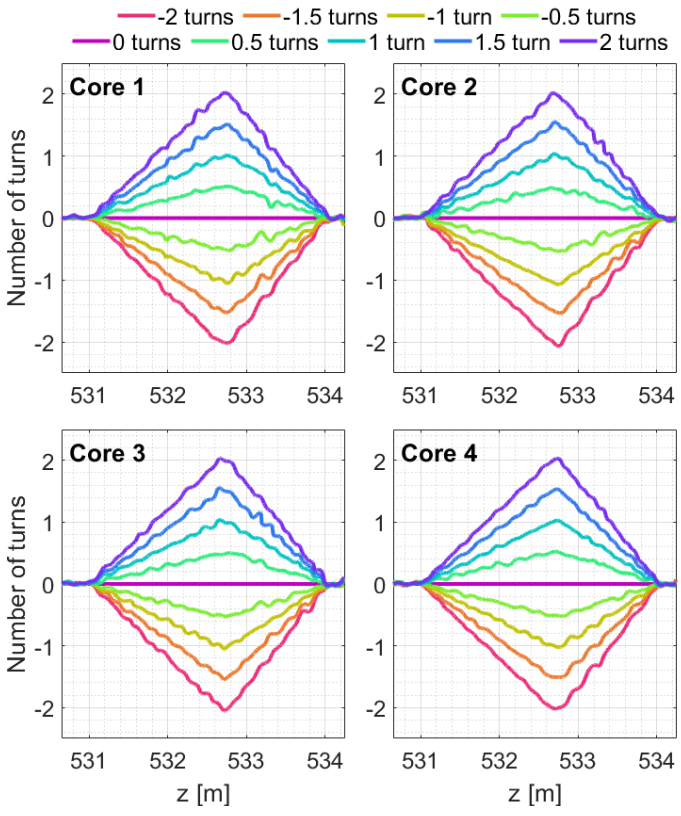

Figure 6.5: Number of turns measured with respect to the reference state when the U4CF is connected to the OFDR through 500 m of SMF.

6.5 CONCLUSION

The chapter explored the polarization sensing capacity of unspun MCFs using the twist measurements as examples. For this purpose, a modification allowing to alter the polarization state of the input light was introduced into the OFDR scheme. The measurements obtained with the MCF were in a total agreement with the controlled twists that were applied during the experiments. The reliable measurements were obtained even at a distance that was 0.5 km away from the input point of the OFDR device. Moreover, it was verified that the tested fibers had the same elasto-optic properties as the conventional SMFs.

7

DISCUSSION AND FUTURE OUTLOOKS

In this work, optical fibers have been considered as a platform for several sensing applications. The first of the developed configurations was a distributed acoustic sensor (DAS); in this case, machine learning was applied for the first time as a tool for mitigating the effects of fading on the Rayleigh traces. The second configuration was built by multiplexing independent fiber structures for the purpose of thermal monitoring during the treatment of tumors. In the third configuration, used to conduct shape sensing, spectral correlation analysis (SCA) was applied in a novel way, which allowed to implement the simultaneous interrogation of the cores of a multi-core fiber (MCF). In the fourth configuration, polarization-resolved interrogation setup was built to conduct twist measurements. The development of the sensor became possible by utilizing unspun MCF instead of conventional single-mode fiber (SMF). There are several potential directions for extending these methods.

In the case of DAS, the tests were conducted in laboratory conditions, and possible continuations of the work may involve tests done with real seismic activity, which is the primary application of DAS.

Similarly, the next logical step of the thermal ablation work is to test the multiplexed fiber configuration in the clinical trials.

It is also worth exploring the multi-core SCA method in the context of temperature measurements, but not necessarily in the medical area. Potentially, the spatial resolution achieved by SCA in shape reconstruction can be increased by using fibers with higher number of cores. However, additional cores also lead to the increase in noise, which means that the trade-off needs to be maintained.

On overall, two multiplexing methodologies were considered in the work, and the advantages of each of them depend on their application. The TDM approach can offer high SNR values due to enhanced backscattering, but the monitored lengths need to be sufficiently short, meaning that the primary applicability of the method is in medicine, which is the case of thermal ablation. Moreover, the applications in thermal ablation cannot work with MCFs. MCFs are not applicable in the case when measurements need to be done in a 2D pattern, since all of the cores are within the same fiber structure. On the other hand, the extended SCA is applicable to fibers with standard gain values. Moreover, the sensing range of OFDR can be fully utilized to cover the length of each multiplexed channel, instead of accommodating the combined lengths of all of the channels. Hence, this configuration is a preferable choice when longer distances need to be measured, which is required, for example, in industrial applications, or robotics. Nevertheless, the TDM method only needs to store one signature that contains the traces of all cores. In the case of the extended SCA, the signatures need to be collected separately for each

core, and in terms of processing power, the computations are more demanding. All of these factors need to be taken into consideration when selecting the multiplexing methodology.

The extended SCA and polarization-resolved twist measurements can be combined, which could expand the shape sensing component of the work onto 3-dimensional spaces. By using polarization-resolved OFDR, the internal twist can be determined from the local birefringence vector and compensated during the shape recreation, making it feasible to conduct shape sensing in 3D. However, when considering the issue of twist, the modified method would be applicable only for multi-core fibers, and not for general multi-channel fiber structures, which still consist of conventional spun SMFs.

Machine learning angle is also worth exploring in the context of multiple channels. For instance, the correlation step in SCA can be implemented with a neural network to make the method more efficient in detecing spectral shifts associated with dynamically changing stimuli.

Future directions involve exploring the issue of the cross-sensitivity to strain and temperature in the multiplexed configurations. Possible directions include machine learning decoupling or using modified fibers with zero strain sensitivity, as well as FBGs [94]. As a result, it could be possible to measure both strain and temperature along one channel, and only temperature along the second channel. Thus, the thermal impact in the first channel could be compensated using computational techniques. After achieving this, the discussed sensing approaches can be combined into a multi-parameter sensor, since there is a significant research interest in sensors that can simultaneously observe temperature and vibrations.

BIBLIOGRAPHY

[1] Brian Culshaw and Alan Kersey. "Fiber-Optic Sensing: A Historical Perspective." In: *Journal of Lightwave Technology* 26.9 (May 2008), pp. 1064–1078. URL: https://opg.optica.org/jlt/abstract.cfm?URI=jlt-26-9-1064.

[2] María R. Fernández-Ruiz, Hugo F. Martins, Ethan F. Williams, Carlos Becerril, Regina Magalhães, Luis Costa, Sonia Martin-Lopez, Zhensheng Jia, Zhongwen Zhan, and Miguel González-Herráez. "Seismic monitoring With distributed acoustic sensing from the near-surface to the deep oceans." In: *Journal of Lightwave Technology* 40.5 (Nov. 2021), pp. 1453–1463. DOI: 10.1109/JLT.2021.3128138. URL: https://ieeexplore.ieee.org/document/9616386.

[3] Zhaoqiang Peng, Jianan Jian, Hongqiao Wen, Andrei Gribok, Mohan Wang, Hu Liu, Sheng Huang, Zhi-Hong Mao, and Kevin P. Chen. "Distributed fiber sensor and machine learning data analytics for pipeline protection against extrinsic intrusions and intrinsic corrosions." In: *Optics Express* 28.19 (Sept. 2020), pp. 27277–27292. DOI: 10.1364/OE.397509. URL: https://opg.optica.org/oe/fulltext.cfm?uri=oe-28-19-27277&id=437782.

[4] Zhongqi Li, Jianwei Zhang, Maoning Wang, Yuzhong Zhong, and Fei Peng. "Fiber distributed acoustic sensing using convolutional long short-term memory network: a field test on high-speed railway intrusion detection." In: *Optics Express* 28.3 (Feb. 2020), pp. 2925–2938. DOI: 10.1364/OE.28.002925. URL: https://opg.optica.org/oe/fulltext.cfm?uri=oe-28-3-2925&id=426132.

[5] Wei-Qi Qin, Guo-Ming Ma, Meng Zhang, Yuan Wang, Jun Jiang, Hongyang Zhou, and Xilin Wang; Chao Yan. "Quasi-Distributed Vibration Sensing System for Transformers Using a Phase-Sensitive OFDR." In: *IEEE Transactions on Industrial Electronics* 69.10 (Jan. 2022), pp. 10625–10633. DOI: 10.1109/TIE.2021.3139188. URL: https://ieeexplore.ieee.org/document/9673109.

[6] Ester Catalano, Agnese Coscetta, Enis Cerri, Nunzio Cennamo, Luigi Zeni, and A. Minardo. "Automatic traffic monitoring by φ-OTDR data and Hough transform in a real-field environment." In: *Applied Optics* 60.13 (May 2021), pp. 3579–3584. DOI: 10.1364/AO.422385. URL: https://opg.optica.org/ao/abstract.cfm?URI=ao-60-13-3579.

[7] Mudabbir Badar, Ping Lu, Qirui Wang, Thomas Boyer, Kevin P. Chen, and Paul R. Ohodnicki. "Real-Time Optical Fiber-Based Distributed Temperature Monitoring of Insulation Oil-Immersed Commercial Distribution Power Transformer." In: *IEEE Sensors Journal* 21.3 (Sept. 2020), pp. 3013–3019. DOI: 10.1109/JSEN.

2020.3024943. URL: https://ieeexplore.ieee.org/document/9201121.

[8] Gabriele Bolognini and Arthur Hartog. "Raman-based fibre sensors: Trends and applications." In: *Optical Fiber Technology* 19.6, Part B (2013). Optical Fiber Sensors, pp. 678–688. ISSN: 1068–5200. DOI: 10.1016/j.yofte.2013.08.003. URL: https://www.sciencedirect.com/science/article/pii/S1068520013001090.

[9] Abhisek Ukil, Hubert Braendle, and Peter Krippner. "Distributed Temperature Sensing: Review of Technology and Applications." In: *IEEE Sensors Journal* 12.5 (July 2012), pp. 885–892. DOI: 10.1109/JSEN.2011.2162060. URL: https://ieeexplore.ieee.org/document/5955066.

[10] Seong-O Yang, Seungmin Lee, Seok Ho Song, and Jihyung Yoo. "Development of a distributed optical thermometry technique for battery cells." In: *International Journal of Heat and Mass Transfer* 194 (2022), p. 123020. ISSN: 0017–9310. DOI: 10.1016/j.ijheatmasstransfer.2022.123020. URL: https://www.sciencedirect.com/science/article/pii/S0017931022004938.

[11] Antonella Chiuchiolo, Luca Palmieri, Marco Consales, Michele Giordano, Anna Borriello, Hugues Bajas, Andrea Galtarossa, Marta Bajko, and Andrea Cusano. "Cryogenic-temperature profiling of high-power superconducting lines using local and distributed optical-fiber sensors." In: *Optics Letters* 40.19 (Oct. 2015), pp. 4424–4427. DOI: 10.1364/OL.40.004424. URL: https://opg.optica.org/ol/abstract.cfm?URI=ol-40-19-4424.

[12] Abhisek Ukil, Wang Libo, and Gang Ai. "Leak detection in natural gas distribution pipeline using distributed temperature sensing." In: *IECON 2016 - 42nd Annual Conference of the IEEE Industrial Electronics Society*. 2016, pp. 417–422. DOI: 10.1109/IECON.2016.7793562.

[13] Alex K. Sang, Mark E. Froggatt, Dawn K. Gifford, Stephen T. Kreger, and Bryan D. Dickerson. "One Centimeter Spatial Resolution Temperature Measurements in a Nuclear Reactor Using Rayleigh Scatter in Optical Fiber." In: *IEEE Sensors Journal* 8.7 (2008), pp. 1375–1380. DOI: 10.1109/JSEN.2008.927247.

[14] Han Li, Jun Zhang, Chaojun Jiang, Qi Liu, Maozeng Zhang, and Jingsong Zhou. "Muscle Temperature Sensing and Control with a Wearable Device for Hand Rehabilitation of People After Stroke." In: *2020 International Conference on Sensing, Measurement & Data Analytics in the era of Artificial Intelligence (ICSMD)*. 2020, pp. 94–99. DOI: 10.1109/ICSMD50554.2020.9261634.

[15] Sanzhar Korganbayev, Martina De Landro, Federica Morra, Alfredo Cigada, and Paola Saccomandi. "Fiber Optic Sensors for Distributed and Quasi-distributed Temperature Measurement." In: *2020 IEEE SENSORS*. 2020, pp. 1–4. DOI: 10.1109/SENSORS47125.2020.9278937.

[16] Zhannat Ashikbayeva, Arman Aitkulov, Alexey Wolf, Alexander Dostovalov, Aida Amantayeva, Aliya Kurbanova, Vassilis J. Inglezakis, and Daniele Tosi. "Investigation of Thermal Effects of Radiofrequency Ablation Mediated with Iron Oxide Nanoparticles Dispersed in Agarose and Chitosan Solvents." In: *Applied Sciences* 11.5 (2021). ISSN: 2076-3417. DOI: 10.3390/app11052437. URL: https://www.mdpi.com/2076-3417/11/5/2437.

[17] Dimitri A. Lezcano, Iulian I. Iordachita, and Jin Seob Kim. "Lie-Group Theoretic Approach to Shape-Sensing Using FBG-Sensorized Needles Including Double-Layer Tissue and S-Shape Insertions." In: *IEEE Sensors Journal* 22.22 (Oct. 2022), pp. 22232–22243. DOI: 10.1109/JSEN.2022.3212209.

[18] Xuan Thao Ha, Di Wu, Mouloud Ourak, Gianni Borghesan, Arianna Menciassi, and Emmanuel Vander Poorten. "Sensor Fusion for Shape Reconstruction Using Electromagnetic Tracking Sensors and Multi-Core Optical Fiber." In: *IEEE Robotics and Automation Letters* 8.7 (May 2023), pp. 4076–4083. DOI: 10.1109/LRA.2023.3280456.

[19] Peng Wei, Jie Liu, Zejing Dai, and Ming Li. "Monitoring the Shape of Satellite Wing Frame Using FBG Sensors in High Electronic Noise, Vacuum, and -196 °C Environment." In: *IEEE Transactions on Industrial Electronics* 64.1 (Jan. 2017), pp. 691–700. DOI: 10.1109/TIE.2016.2606901.

[20] Tianliang Li, Liang Qiu, and Hongliang Ren. "Distributed Curvature Sensing and Shape Reconstruction for Soft Manipulators With Irregular Cross Sections Based on Parallel Dual-FBG Arrays." In: *IEEE/ASME Transactions on Mechatronics* 25.1 (Feb. 2020), pp. 406–417. DOI: 10.1109/TMECH.2019.2949151.

[21] Hedan Bai, Shuo Li, Jose Barreiros, Yaqi Tu, Clifford R. Pollock, and Robert F. Shepherd. "Stretchable distributed fiber-optic sensors." In: *Science* 370.6518 (Nov. 2020), pp. 848–852. DOI: 10.1126/science.aba5504. URL: https://www.science.org/doi/10.1126/science.aba5504.

[22] Ignazio Floris, Jose M. Adam, Pedro A. Calderón, and Salvador Sales. "Fiber Optic Shape Sensors: A comprehensive review." In: *Optics and Lasers in Engineering* 139 (Apr. 2021), p. 106508. DOI: 10.1016/j.optlaseng.2020.106508. URL: https://www.sciencedirect.com/science/article/pii/S0143816620319461.

[23] John William Arkwright, Ian David Underhill, Simon A. Maunder, Alireza Jafari, Nick Cartwright, and Charles Lemckert. "Fiber Optic Pressure Sensing Arrays for Monitoring Horizontal and Vertical Pressures Generated by Traveling Water Waves." In: *IEEE Sensors Journal* 14.8 (Mar. 2014), pp. 2739–2742. DOI: 10.1109/JSEN.2014.2311806.

[24] A. Aitkulov, M. Sypabekova, C. Molardi, W. Blanc, and D. Tosi. "Fabrication and performance evaluation of reflectorless refractive index fiber optic sensors using etched enhanced backscattering fibers." In: *Measurement* 172 (Feb. 2021), p. 108874. ISSN: 0263-2241. DOI: https://doi.org/10.1016/j.measurement.2020.108874. URL: https://www.sciencedirect.com/science/article/pii/S0263224120313622.

[25] Junyi Guo, Mengya Sun, Jinhui Fang, Guangqing Wei, Bin Shi, and Hongtao Jiang. "High-Sensitivity Seawater Salinity Sensing With Cladding Etched Fiber Bragg Grating Technology." In: *IEEE Sensors Journal* 23.13 (May 2023), pp. 14182–14192. DOI: 10.1109/JSEN.2023.3279324.

[26] Christian Totland, Peter J. Thomas, Ingvild Fladvad Størdal, and Espen Eek. "A Fully Distributed Fibre Optic Sensor for the Detection of Liquid Hydrocarbons." In: *IEEE Sensors Journal* 21.6 (Mar. 2021), pp. 7631–7637. DOI: 10.1109/JSEN.2020.3047549.

[27] Alimzhan Sultangazin, Janysbek Kusmangaliyev, Arman Aitkulov, Dana Akilbekova, Massimo Olivero, and Daniele Tosi. "Design of a Smartphone Plastic Optical Fiber Chemical Sensor for Hydrogen Sulfide Detection." In: *IEEE Sensors Journal* 17.21 (2017), pp. 6935–6940. DOI: 10.1109/JSEN.2017.2752717.

[28] Gaopeng Wang, Jixiang Dai, and Minghong Yang. "Fiber-Optic Hydrogen Sensors: A Review." In: *IEEE Sensors Journal* 21.11 (Oct. 2021), pp. 12706–12718. DOI: 10.1109/JSEN.2020.3029519.

[29] Iacopo Toccafondo, Tiziano Nannipieri, Alessandro Signorini, Elisa Guillermain, Jochen Kuhnhenn, Markus Brugger, and Fabrizio Di Pasquale. "Raman Distributed Temperature Sensing at CERN." In: *IEEE Photonics Technology Letters* 27.20 (July 2015), pp. 2182–2185. DOI: 10.1109/LPT.2015.2456029.

[30] T. Horiguchi, K. Shimizu, T. Kurashima, M. Tateda, and Y. Koyamada. "Development of a distributed sensing technique using Brillouin scattering." In: *Journal of Lightwave Technology* 13.7 (July 1995), pp. 1296–1302. DOI: 10.1109/50.400684.

[31] Ezra Ip, Jian Fang, Yaowen Li, Qiang Wang, Ming-Fang Huang, Milad Salemi, and Yue-Kai Huang. "Distributed fiber sensor network using telecom cables as sensing media: technology advancements and applications [Invited]." In: *Journal of Optical Communications and Networking* 14.1 (Nov. 2022), A61–A68. DOI: 10.1364/JOCN.439175.

[32] Khurram Naeem, Changwon Lee, Kadathala Linganna, Chul Kang, Myoung-Kyu Oh, Nan Ei Yu, Hoonsoo Kang, and Bok Hyeon Kim. "Multiparameter Distributed Fiber Sensor Based on Optical Frequency-Domain Reflectometry and Bandwidth-Division Multiplexing." In: *IEEE Sensors Journal* 21.22 (Aug. 2021), pp. 25703–25709. DOI: 10.1109/JSEN.2021.3106385.

[33] Fumihiko Ito, Xinyu Fan, and Yusuke Koshikiya. "Long-Range Coherent OFDR With Light Source Phase Noise Compensation." In: *Journal of Lightwave Technology* 30.8 (Sept. 2012), pp. 1015–1024. DOI: 10.1109/JLT.2011.2167598.

[34] B. J. Soller, M. Wolfe, and M. E. Froggatt. "Polarization Resolved Measurement of Rayleigh Backscatter in Fiber-optic Components." In: *Optical Fiber Communication Conference and Exposition and The National Fiber Optic Engineers Conference*. Optica Publishing Group, 2005, NWD3. URL: https://opg.optica.org/abstract.cfm?URI=NFOEC-2005-NWD3.

[35] Andrea Galtarossa and Luca Palmieri. "Mapping of intense magnetic fields based on polarization sensitive reflectometry in single mode optical fibers." In: *2013 Africon*. 2013, pp. 1–5. DOI: 10.1109/AFRCON.2013.6757675.

[36] M. Aerssens, A. Gusarov, P. Moreau, P. Malard, V. Massaut, P. Mégret, and M. Wuilpart. "Development of a Jones vector based model for the measurement of a plasma current in a thermonuclear fusion reactor with a POTDR setup." In: *Optical Sensing and Detection II*. Ed. by Francis Berghmans, Anna Grazia Mignani, and Piet De Moor. Vol. 8439. International Society for Optics and Photonics. SPIE, 2012, p. 84390D. DOI: 10.1117/12.922714. URL: https://doi.org/10.1117/12.922714.

[37] A. Galtarossa, D. Grosso, and L. Palmieri. "Accurate Characterization of Twist-Induced Optical Activity in Single-Mode Fibers by Means of Polarization-Sensitive Reflectometry." en. In: *IEEE Photon. Technol. Lett.* 21.22 (Nov. 2009), pp. 1713–1715. ISSN: 1041-1135, 1941-0174. DOI: 10.1109/LPT.2009.2032152. URL: http://ieeexplore.ieee.org/document/5272342/.

[38] Luna Innovations. *Optical Backscatter Reflectometer 4600 User Guide*. English. Version 2.2.1. Luna Innovations. June 2, 2006. 240 pp.

[39] Lianlian Xie, Zinan Wang, Ji Xiong, and Yunjiang Rao. "Distributed acoustic sensing based on correlation analysis of fast and linear sweep OFDR." In: *2017 16th International Conference on Optical Communications and Networks (ICOCN)*. 2017, pp. 1–3. DOI: 10.1109/ICOCN.2017.8121189.

[40] Lihi Shiloh and Avishay Eyal. "Sinusoidal frequency scan OFDR with fast processing algorithm for distributed acoustic sensing." In: *Optics Express* 25.16 (Aug. 2017), pp. 19205–19215. DOI: 10.1364/OE.25.019205. URL: https://opg.optica.org/oe/abstract.cfm?URI=oe-25-16-19205.

[41] Da-Peng Zhou, Zengguang Qin, Wenhai Li, Liang Chen, and Xiaoyi Bao. "Distributed vibration sensing with time-resolved optical frequency-domain reflectometry." In: *Optics Express* 20.12 (June 2012), pp. 13138–13145. DOI: 10.1364/OE.20.013138. URL: https://opg.optica.org/oe/abstract.cfm?URI=oe-20-12-13138.

[42] Mohammadmasoud Zabihi, Yusheng Chen, Tong Zhou, Jingxiao Liu, Yuanyuan Shan, Zhen Meng, Feng Wang, Yixin Zhang, Xuping Zhang, and Mengmeng Chen. "Continuous Fading Suppression Method for ϕ-OTDR Systems Using Optimum Tracking Over Multiple Probe Frequencies." In: *Journal of Lightwave Technology* 37.14 (May 2019), pp. 3602–3610. DOI: 10.1109/JLT.2019.2918353. URL: https://ieeexplore.ieee.org/document/8720050.

[43] Shengtao Lin, Zinan Wang, Ji Xiong, Yun Fu, Jialin Jiang, Yue Wu, Yongxiang Chen, Chongyu Lu, and Yunjiang Rao. "Rayleigh Fading Suppression in One-Dimensional Optical Scatters." In: *IEEE Access* 7 (Jan. 2019), pp. 17125–17132. DOI: 10.1109/ACCESS.2019.2895126.

[44] Yoshifumi Wakisaka, Daisuke Iida, Hiroyuki Oshida, and Nazuki Honda. "Fading Suppression of φ-OTDR With the New Signal Processing Methodology of Complex Vectors Across Time and Frequency Domains." In: *Journal of Lightwave Technology* 39.13 (Apr. 2021), pp. 4279–4293. DOI: 10.1109/JLT.2021.3071159.

[45] Hao Li, Tao Liu, Cunzheng Fan, Baoqiang Yan, Junfeng Chen, Tianye Huang, Zhijun Yan, and Qizhen Sun. "Fading Suppression for Distributed Acoustic Sensing Assisted With Dual-Laser System and Differential-Vector-Sum Algorithm." In: *IEEE Sensors Journal* 22.10 (Apr. 2022), pp. 9417–9425. DOI: 10.1109/JSEN.2022.3164695.

[46] Fufei Pang, Mengting He, Huanhuan Liu, Xuanwei Mei, Jiaming Tao, Tongzhi Zhang, Xiaobei Zhang, Na Chen, and Tingyun Wang. "A Fading-Discrimination Method for Distributed Vibration Sensor Using Coherent Detection of φ -OTDR." In: *IEEE Photonics Technology Letters* 28.23 (Oct. 2016), pp. 2752–2755. DOI: 10.1109/LPT.2016.2616023.

[47] Kexin Cui, Fei Liu, Kuiru Wang, Xiaojun Liu, Jinhui Yuan, Binbin Yan, and Xian Zhou. "Interference-Fading-Suppressed Pulse-Coding φ-OTDR Using Spectrum Extraction and Rotated-Vector-Sum Method." In: *IEEE Photonics Journal* 13.6 (Oct. 2021), pp. 1–6. DOI: 10.1109/JPHOT.2021.3121064.

[48] L. Rossi, L. K. Cheng, W. de Jong, R. Jansen, and G. Bolognini. "Low-noise ϕ-OTDR employing nonlinear optical preamplification for distributed acoustic sensing." In: *Appl. Opt.* 62.16 (June 2023), E70–E77. DOI: 10.1364/AO.483814. URL: https://opg.optica.org/ao/abstract.cfm?URI=ao-62-16-E70.

[49] Xiangge He, Zhi Cao, Peng Ji, Lijuan Gu, Shipeng Wei, Bo Fan, Min Zhang, and Hailong Lu. "Eliminating the Fading Noise in Distributed Acoustic Sensing Data." In: *IEEE Transactions on Geoscience and Remote Sensing* 61, 3263159 (Jan. 2023), p. 3263159. DOI: 10.1109/TGRS.2023.3263159.

[50] Yuxiang Feng, Weilin Xie, Yinxia Meng, Jiang Yang, Qiang Yang, Yan Ren, Tianwai Bo, Zhongwei Tan, Wei Wei, and Yi Dong. "Multicore Fiber Enabled Fading Suppression in ϕ-OFDR Based High Resolution Quantitative DVS." In: *IEEE Photonics Technology Letters* 34.19 (Oct. 2022), pp. 1026–1029. DOI: 10.1109/LPT.2022.3199604. URL: https://ieeexplore.ieee.org/document/9858916.

[51] Wei Feng, Mengfan Wang, Hailun Jia, Kang Xie, and Guojie Tu. "High Precision Phase-OFDR Scheme Based on Fading Noise Suppression." In: *Journal of Lightwave Technology* 40.3 (Feb. 2022), pp. 900–908. DOI: 10.1109/JLT.2022.3142164. URL: https://ieeexplore.ieee.org/document/9678030.

[52] Tabi Fouda Bernard Marie, Dezhi Han, and Bowen An. "Pattern recognition algorithm and software design of an optical fiber vibration signal based on Φ-optical time-domain reflectometry." In: *Applied Optics* 58.31 (Oct. 2019), pp. 8423–8432. DOI: 10.1364/AO.58.008423. URL: https://opg.optica.org/ao/fulltext.cfm?uri=ao-58-31-8423&id=422545.

[53] Yu Wang, Pengfei Wang, Kai Ding, Hao Li, Jianguo Zhang, Xin Liu, Qing Bai, Dong Wang, and Baoquan Jin. "Pattern Recognition Using Relevant Vector Machine in Optical Fiber Vibration Sensing System." In: *IEEE Access* 7 (Jan. 2019), pp. 5886–5895. DOI: 10.1109/ACCESS.2018.2889699. URL: https://ieeexplore.ieee.org/document/8598862.

[54] Huijuan Wu, Jiping Chen, Xiangrong Liu, Yao Xiao, Mengjiao Wang, Yi Zheng, and Yunjiang Rao. "One-Dimensional CNN-Based Intelligent Recognition of Vibrations in Pipeline Monitoring With DAS." In: *Journal of Lightwave Technology* 37.17 (Sept. 2019), pp. 4359–4366. DOI: 10.1109/JLT.2019.2923839. URL: https://ieeexplore.ieee.org/document/8740957.

[55] Pablo D. Hernández, Jaime A. Ramírez, and Marcelo A. Soto. "Deep-Learning-Based Earthquake Detection for Fiber-Optic Distributed Acoustic Sensing." In: *Journal of Lightwave Technology* 40.8 (Dec. 2021), pp. 2639–2650. DOI: 10.1109/JLT.2021.3138724. URL: https://ieeexplore.ieee.org/document/9664395.

[56] Christos Karapanagiotis, Konstantin Hicke, Aleksander Wosniok, and Katerina Krebber. "Distributed humidity fiber-optic sensor based on BOFDA using a simple machine learning approach." In: *Optics Express* 30.8 (Mar. 2022), pp. 12484–12494. DOI: 10.1364/OE.453906. URL: https://opg.optica.org/oe/fulltext.cfm?uri=oe-30-8-12484&id=470902.

[57] Yi Luo and Nima Mesgarani. "Conv-TasNet: Surpassing Ideal Time–Frequency Magnitude Masking for Speech Separation." In: *IEEE/ACM Transactions on Audio, Speech, and Language Processing* 27.8 (May 2019), pp. 1256–1266. DOI: 10.1109/TASLP.2019.2915167. URL: https://ieeexplore.ieee.org/document/8707065.

[58] Z.-H. Zhu, Y.-Y. Xiao, and R.-M. Yao. "CNN-based few-mode fiber modal decomposition method using digital holography." In: *Applied Optics* 60.24 (Aug. 2021), pp. 7400–7405. DOI: 10.1364/AO.427847. URL: https://opg.optica.org/ao/fulltext.cfm?uri=ao-60-24-7400&id=457328.

[59] Chenda Lu, Qinghua Tian, Lei Zhu, Ran Gao, Haipeng Yao, Feng Tian, Qi Zhang, and Xiangjun Xin. "Mitigating the ambiguity problem in the CNN-based wavefront correction." In: *Optics Letters* 47.13 (June 2022), pp. 3251–3254. DOI: 10.1364/OL.459799. URL: https://opg.optica.org/ol/fulltext.cfm?uri=ol-47-13-3251&id=477285.

[60] Yifan Liu, Ziwen Zhang, Jiang Qian, Yong Wang, and Xiaobo Yang. "A Phase Filtering Method based on Deep Learning Network." In: *International Geoscience and Remote Sensing Symposium*. IEEE, 2021. DOI: 10.1109/IGARSS47720.2021.9554552.

[61] Colin Lea, René Vidal, Austin Reiter, and Gregory D. Hager. "Temporal Convolutional Networks: A Unified Approach to Action Segmentation." In: *European Conference on Computer Vision*. 2016. DOI: 10.1007/978-3-319-49409-8_7.

[62] Mikael Sabuhi, Ming Zhou, Cor-Paul Bezemer, and Petr Musilek. "Applications of Generative Adversarial Networks in Anomaly Detection: A Systematic Literature Review." In: *IEEE Access* 9 (Nov. 2021), pp. 161003–161029. DOI: 10.1109/ACCESS.2021.3131949. URL: https://ieeexplore.ieee.org/document/9631286.

[63] Xiangjie He, Zhengwei Chang, Linghao Zhang, Houdong Xu, Hongbo Chen, and Zhongqiang Luok. "A Survey of Defect Detection Applications Based on Generative Adversarial Networks." In: *IEEE Access* 10 (Oct. 2022), pp. 113493–113512. DOI: 10.1109/ACCESS.2022.3217227. URL: https://ieeexplore.ieee.org/document/9930483.

[64] Yushu Zhang, Hongbo Lin, Yue Li, and Haitao Ma. "A Patch Based Denoising Method Using Deep Convolutional Neural Network for Seismic Image." In: *IEEE Access* 7 (Oct. 2019), pp. 156883–156894. DOI: 10.1109/ACCESS.2019.2949774. URL: https://ieeexplore.ieee.org/document/8884145.

[65] Sreyas Mohan, Ramon Manzorro, Joshua L. Vincent, Binh Tang, Dev Y. Sheth, Eero P. Simoncelli, David S. Matteson, Peter A. Crozier, and Carlos Fernandez-Granda. "Deep Denoising for Scientific Discovery: A Case Study in Electron Microscopy." In: *IEEE Transactions on Computational Imaging* 8 (May 2022), pp. 585–597. DOI: 10.1109/TCI.2022.3176536. URL: https://ieeexplore.ieee.org/document/9779676.

[66] David J. Ma, Hortense A-M. Le, Yuming Ye, Andrew F. Laine, Jeffery A. Lieberman, Douglas L. Rothman, Scott A. Small, and Jia Guo. "Magnetic Resonance Spectroscopy Frequency and Phase Correction Using Convolutional Neural Networks." In: *Magnetic Resonance in Medicine* 87.4 (Dec. 2021), pp. 1700–1710. DOI:

10.1002/mrm.29103. URL: https://pubmed.ncbi.nlm.nih.gov/34931715/.

[67] Sébastien Loranger, Mathieu Gagn'e, Victor Lambin-Iezzi, and Raman Kashyap. "Rayleigh scatter based order of magnitude increase in distributed temperature and strain sensing by simple UV exposure of optical fibre." In: *Scientific Reports* 5.1 (June 2015). URL: https://api.semanticscholar.org/CorpusID:6725722.

[68] Qirui Wang, Kehao Zhao, Mudabbir Badar, Xinruo Yi, Ping Lu, Michael Buric, Zhi-Hong Mao, and Kevin Chen. "Improving OFDR Distributed Fiber Sensing by Fibers With Enhanced Rayleigh Backscattering and Image Processing." In: *IEEE Sensors Journal* 22.19 (Oct. 2022), pp. 18471–18478. DOI: 10.1109/JSEN.2022.3197730.

[69] Aidong Yan, Sheng Huang, Shuo Li, Rongzhang Chen, P.R. Ohodnicki, Michael Buric, Shiwoo Lee, Ming-Jun Li, and Kevin Chen. "Distributed Optical Fiber Sensors with Ultrafast Laser Enhanced Rayleigh Backscattering Profiles for Real-Time Monitoring of Solid Oxide Fuel Cell Operations." In: *Scientific Reports* 7 (Dec. 2017). DOI: 10.1038/s41598-017-09934-3.

[70] Timothy Lee, Martynas Beresna, Ali Masoudi, and Gilberto Brambilla. "Enhanced-Backscattering and Enhanced-Backreflection Fibers for Distributed Optical Fiber Sensors." In: *Journal of Lightwave Technology* 41.13 (June 2023), pp. 4051–4064. DOI: 10.1109/JLT.2023.3281136.

[71] Wilfried Blanc, Valérie Mauroy, Luan Nguyen, B.N. Shivakiran Bhaktha, Patrick Sebbah, Bishnu P. Pal, and Bernard Dussardier. "Fabrication of Rare Earth-Doped Transparent Glass Ceramic Optical Fibers by Modified Chemical Vapor Deposition." In: *Journal of the American Ceramic Society* 94.8 (June 2011), pp. 2315–2318. DOI: https://doi.org/10.1111/j.1551-2916.2011.04672.x. eprint: https://ceramics.onlinelibrary.wiley.com/doi/pdf/10.1111/j.1551-2916.2011.04672.x. URL: https://ceramics.onlinelibrary.wiley.com/doi/abs/10.1111/j.1551-2916.2011.04672.x.

[72] Zhiyong Zhao, Yunli Dang, Ming Tang, Liang Wang, Lin Gan, Songnian Fu, Chen Yang, Weijun Tong, and Chao Lu. "Enabling Simultaneous DAS and DTS Through Space-Division Multiplexing Based on Multicore Fiber." In: *Journal of Lightwave Technology* 36.24 (Oct. 2018), pp. 5707–5713. DOI: 10.1109/JLT.2018.2878559.

[73] Jing Jin, Yibo Zhang, Yunhong Zhu, Dongwei Zhang, and Haoshi Zhang. "Analysis and Correction Method of Axial Strain Error in Multi-Core Fiber Shape Sensing." In: *IEEE Sensors Journal* 20.21 (June 2020), pp. 12716–12722. DOI: 10.1109/JSEN.2020.3001937.

[74] Sheng Li, Peidong Hua, Zhenyang Ding, Kun Liu, Yong Yang, Junpeng Zhao, Ming Panand Haohan Guo, Teng Zhang, Li Liu, Junfeng Jiang, and Tiegen Liu. "Reconstruction error model of distributed shape sensing based on the reentered frame in OFDR." In: *Optics Express* 30.24 (Nov. 2022), pp. 43255–43270. DOI: 10.1364/OE.471684. URL: https://opg.optica.org/oe/fulltext.cfm?uri=oe-30-24-43255&id=518959.

[75] Yuanpeng Deng, Qingwen Liu, Shuting Liu, and Zuyuan He. "Multipath Quasi-Distributed Acoustic Sensing Based on Space Division Multiplexing and Time-Gated OFDR." In: *IEEE Sensors Journal* 23.11 (Apr. 2023), pp. 11615–11620. DOI: 10.1109/JSEN.2023.3261329.

[76] Wing Ko, Kenneth S. Feder, Xiaoguang Sun, Jie Li, and Paul S. Westbrook. "Simultaneous interrogation of multiple cores in a shape sensor fiber with a graded index fiber micro-turnaround." In: *Optics Express* 30.14 (July 2022), pp. 24452–24460. DOI: 10.1364/OE.460540. URL: https://opg.optica.org/oe/fulltext.cfm?uri=oe-30-14-24452&id=477148.

[77] Leonardo Marcon, Andrea Galtarossa, and Luca Palmieri. "High-frequency high-resolution distributed acoustic sensing by optical frequency domain reflectometry." In: *Optics Express* 27.10 (May 2019), pp. 13923–13933. DOI: 10.1364/OE.27.013923. URL: https://www.osapublishing.org/oe/fulltext.cfm?uri=oe-27-10-13923&id=411875.

[78] Y. LeCun, B. Boser, J. S. Denker, D. Henderson, R. E. Howard, W. Hubbard, and L. D. Jackel. "Backpropagation Applied to Handwritten Zip Code Recognition." In: *Neural Computation* 1.4 (Dec. 1989), pp. 541–551. DOI: 10.1162/neco.1989.1.4.541. URL: https://ieeexplore.ieee.org/document/6795724.

[79] Olaf Ronneberger, Philipp Fischer, and Thomas Brox. "U-Net: Convolutional Networks for Biomedical Image Segmentation." In: *International Conference on Medical Image Computing and Computer-Assisted Intervention*. 2015. DOI: 10.1007/978-3-319-24574-4_28. URL: https://link.springer.com/chapter/10.1007/978-3-319-24574-4_28.

[80] Zhannat Ashikbayeva, Arman Aitkulov, Madina Jelbuldina, Aizhan Issatayeva, Aidana Beisenova, Carlo Molardi, Paola Saccomandi, Wilfried Blanc, Vassilis J. Inglezakis, and Daniele Tosi. "Distributed 2D temperature sensing during nanoparticles assisted laser ablation by means of high-scattering fiber sensors." In: *Scientific Reports* 10 (2020). URL: https://api.semanticscholar.org/CorpusID:220811830.

[81] Riccardo Veronese, Andrea Galtarossa, and Luca Palmieri. "Distributed Characterization of Few-Mode Fibers Based on Optical Frequency Domain Reflectometry." en. In: *J. Lightwave Technol.* 38.17 (Sept. 2020), pp. 4843–4849. ISSN: 0733-8724, 1558-2213. DOI: 10.1109/JLT.2020.2993228. URL: https://ieeexplore.ieee.org/document/9090321/.

[82] J. Pastor-Graells, H. F. Martins, A. Garcia-Ruiz, S. Martin-Lopez, and M. Gonzalez-Herraez. "Single-shot distributed temperature and strain tracking using direct detection phase-sensitive OTDR with chirped pulses." In: *Opt. Express* 24.12 (June 2016), pp. 13121–13133. DOI: 10.1364/OE.24.013121. URL: https://opg.optica.org/oe/abstract.cfm?URI=oe-24-12-13121.

[83] Daniele Tosi, Carlo Molardi, Wilfried Blanc, Tiago Paixão, Paulo Antunes, and Carlos Marques. "Performance Analysis of Scattering-Level Multiplexing (SLMux) in Distributed Fiber-Optic Backscatter Reflectometry Physical Sensors." In: *Sensors* 20.9 (2020). ISSN: 1424-8220. DOI: 10.3390/s20092595. URL: https://www.mdpi.com/1424-8220/20/9/2595.

[84] Daniele Tosi, Carlo Molardi, Marzhan Sypabekova, and Wilfried Blanc. "Enhanced Backscattering Optical Fiber Distributed Sensors: Tutorial and Review." In: *IEEE Sensors Journal* 21.11 (2021), pp. 12667–12678. DOI: 10.1109/JSEN.2020.3010572.

[85] Daniele Tosi, Carlo Molardi, and Wilfried Blanc. "Rayleigh scattering characterization of a low-loss MgO-based nanoparticle-doped optical fiber for distributed sensing." In: *Optics and Laser Technology* 133 (2021), p. 106523. ISSN: 0030-3992. DOI: https://doi.org/10.1016/j.optlastec.2020.106523. URL: https://www.sciencedirect.com/science/article/pii/S0030399220311567.

[86] Zhannat Ashikbayeva, Arman Aitkulov, Timur Sh. Atabaev, Wilfried Blanc, Vassilis J. Inglezakis, and Daniele Tosi. "Green-Synthesized Silver Nanoparticle-Assisted Radiofrequency Ablation for Improved Thermal Treatment Distribution." In: *Nanomaterials* 12.3 (2022). ISSN: 2079-4991. DOI: 10.3390/nano12030426. URL: https://www.mdpi.com/2079-4991/12/3/426.

[87] Jason P. Moore and Matthew D. Rogge. "Shape sensing using multi-core fiber optic cable and parametric curve solutions." In: *Opt. Express* 20.3 (Jan. 2012), pp. 2967–2973. DOI: 10.1364/OE.20.002967. URL: https://opg.optica.org/oe/abstract.cfm?URI=oe-20-3-2967.

[88] Jiwen Cui, Shiyuan Zhao, Chaoqiang Yang, and Jiubin Tan. "Parallel Transport Frame for Fiber Shape Sensing." In: *IEEE Photonics Journal* 10.1 (Dec. 2018), pp. 1–12. DOI: 10.1109/JPHOT.2017.2782736.

[89] C. Knapp and G. Carter. "The generalized correlation method for estimation of time delay." In: *IEEE Transactions on Acoustics, Speech, and Signal Processing* 24.4 (Aug. 1976), pp. 320–327. DOI: 10.1109/TASSP.1976.1162830.

[90] Tetsuya Hayashi, Takuji Nagashima, Tetsuya Nakanishi, Tetsu Morishima, Reiji Kawawada, Antonio Mecozzi, and Cristian Antonelli. "Field-Deployed Multi-Core Fiber Testbed." In: *2019 24th OptoElectronics and Communications Conference (OECC) and 2019 International Conference on Photonics in Switching and Computing (PSC)*. 2019, pp. 1–3. DOI: 10.23919/PS.2019.8818058.

[91] Guolu Yin, Lei Lu, Lei Zhou, Cong Shao, Qingjiang Fu, Jingdong Zhang, and Tao Zhu. "Distributed directional torsion sensing based on an optical frequency domain reflectometer and a helical multicore fiber." In: *Optics Express* 28.11 (2020), pp. 16140–16150. DOI: 10.1364/OE.390549. URL: https://opg.optica.org/oe/fulltext.cfm?uri=oe-28-11-16140&id=431770.

[92] Andrea Galtarossa, Daniele Grosso, Luca Palmieri, and Matteo Rizzo. "Spin-profile characterization in randomly birefringent spun fibers by means of frequency-domain reflectometry." In: *Opt. Lett.* 34.7 (Apr. 2009), pp. 1078–1080. DOI: 10.1364/OL.34.001078. URL: https://opg.optica.org/ol/abstract.cfm?URI=ol-34-7-1078.

[93] Luca Palmieri. "Distributed polarimetric measurements for optical fiber sensing." en. In: *Optical Fiber Technology* 19.6 (Dec. 2013), pp. 720–728. ISSN: 10685200. DOI: 10.1016/j.yofte.2013.07.015. URL: https://linkinghub.elsevier.com/retrieve/pii/S1068520013000953.

[94] Shitai Yang, Hongye Wang, Tingting Yuan, Xiaotong Zhang, and Libo Yuan. "Highly Sensitive Bending Sensor Based on Multicore Optical Fiber With Diagonal Cores Reflector at the Fiber Tip." In: *Journal of Lightwave Technology* 40.17 (June 2022), pp. 6030–6036. DOI: 10.1109/JLT.2022.3184042.